Electrochemical Oxidation of Glycerol in a Proton-Exchange-Membrane Reactor

by

Kanako Okada

A dissertation submitted in partial fulfillment
of the requirements for the degree of
Doctor of Philosophy
(Chemical Engineering)
in the University of Michigan
2013

Doctoral Committee:

Professor Levi T. Thompson, Jr., Chair
Assistant Professor Nina Lin
Assistant Professor Charles W. Monroe
Professor Phillip E. Savage
Associate Professor Angela Violi

ACKNOWLEDGEMENTS

TABLE OF CONTENTS

LIST OF FIGURES

LIST OF TABLES

LIST OF ABBREVIATIONS

AEM anion exchange membrane

BET Brunauer, Emmet, and Teller

CE current efficiency

CL core level

CSTR continuous stirred-tank reactor

CV cyclic voltammetry

DGFC direct glycerol fuel cell

DHE dynamic hydrogen electrode

DMFC direct methanol fuel cell

ECSA electrochemical surface area

EDX energy-dispersive x-ray spectroscopy

EIA Energy Information Administration

FID flame ionization detector

FTIR Fourier transform infrared spectroscopy

GC gas chromatograph

GDL gas diffusion layer

HER hydrogen evolution reaction

HPLC high-performance liquid chromatography

IC internal combustion

ICDD International Center for Diffraction Data

ICP-OES inductively coupled plasma optical emission spectrometry

MEA membrane electrode assembly

MS mass spectrometer

NHE normal hydrogen electrode

OCV open circuit voltage

PEM proton exchange membrane

PLA poly lactic acid

PDF Powder Diffraction File

PTFE polytetrafluoroethylene

RHE reversible hydrogen electrode

SEM scanning electron microscopy

SHE standard hydrogen electrode

SPE solid polymer electrolyte

TCD thermal conductivity detector

TGA thermogravimetric analysis

TPR temperature programmed reaction

XPS X-ray photoelectron spectroscopy

XRD X-ray diffraction

CHAPTER I

Introduction

1.1 Background

Producing fuels and chemicals from renewable biomass resources has become a high priority due to issues associated with fossil fuels, such as heavy dependence on foreign resources, and negative environmental impacts. The Energy Information Administration (EIA) projects that the total consumption of marketed renewable energy will grow by 2.8 percent per year, from 7.7 quadrillion Btu in 2008 to 16 quadrillion Btu in 2035 [1]. As a result, shifting our energy resources from fossil fuels to renewables has also been a primary task among energy-related researchers over the past decades. A good example can be found in the automotive industry in developing hybrid, electric, or fuel cell vehicles to shift from internal combustion (IC) engines powered by fossil fuels to advanced power trains that can potentially utilize renewable resources. Since infrastructures for these new technologies are not readily available yet, biofuels play an important role during this transition to vehicles powered by renewable sources. Biofuels can be distributed like gasoline, so the current infrastructure can be used.

Biofuels have several advantages. They produce much lower levels of harmful emissions (e.g. carbon monoxide, NO_x) than that of petroleum-derived diesel because they are made from biomass feedstocks. They also produce less greenhouse gas during

production and use. As for biodiesel, the most commonly used biofuel, it can be used in conventional diesel engines without modification for the low biodiesel blends, or with low-cost modifications to accept the high biodiesel blends [2].

The EIA reported that biodiesel consumption in the U.S. transportation sector has been increasing rapidly since 2004 as shown in Figure 1.1. Biodiesel consumption has recorded an average annual growth rate of 70%, expanding from 91 million gallons in 2005 to 412 million gallons in 2008 [3]. Its consumption declined from 2007 to 2008 due to the large volume of exports, but U.S. domestic biodiesel production actually increased during that period.
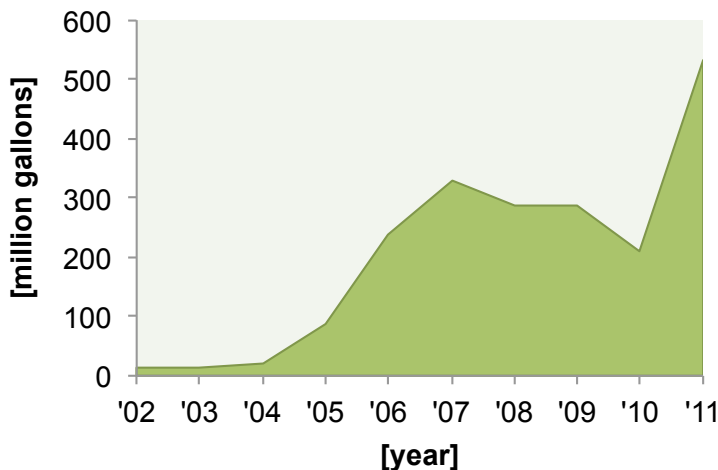
Figure 1.1: Biodiesel consumption in the U.S. transportation sector [4].

Biodiesel is typically produced by transesterification of animal fat or vegetable oil (Figure 1.2). Transesterification of triglycerides typically requires an acid or base as a catalyst depending on the grade of raw materials. This process produces 10% glycerol (typically containing 20% water and residual esterification catalyst) as a by-product [5]. As a result of the expansion of biodiesel utilization, the production of glycerol is expected to increase significantly.

Glycerol ($C_3H_8O_3$, also known as glycerine, glycyl alcohol, and propane-1,2,3-triol) is a colorless, odorless, viscous liquid that is widely used in food additives and

2

$$
\begin{array}{ccccc}
\mathrm{CH_2\text{-}OOC\text{-}R_1} & & & \mathrm{R_1\text{-}COO\text{-}R'} & \mathrm{CH_2\text{-}OH} \\
| & & \text{Catalyst} & & | \\
\mathrm{CH\text{-}OOC\text{-}R_2} & + \ 3\mathrm{R'OH} & \rightleftharpoons & \mathrm{R_2\text{-}COO\text{-}R'} \quad + & \mathrm{CH\text{-}OH} \\
| & & & & | \\
\mathrm{CH_2\text{-}OOC\text{-}R_3} & & & \mathrm{R_3\text{-}COO\text{-}R'} & \mathrm{CH_2\text{-}OH} \\
\\
\text{Glyceride} & \text{Alcohol} & & \text{Esters} & \text{Glycerol}
\end{array}
$$
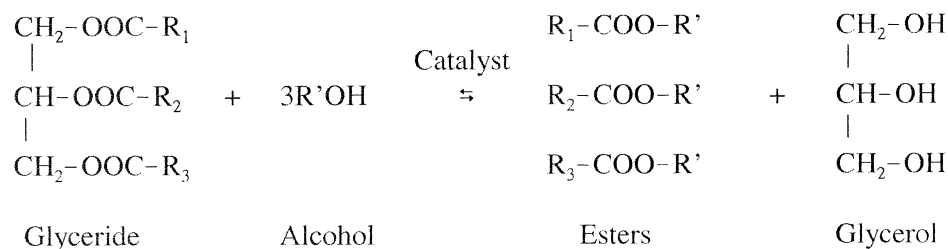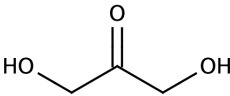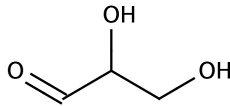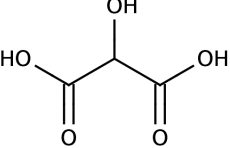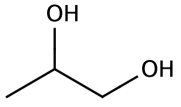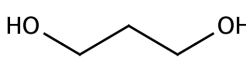
Figure 1.2: Transesterification of triglycerides with alcohol [6].

pharmaceutical formulations. Most glycerol is commercially synthesized from petro-chemicals [6]. Although glycerol is used in food and personal care products, supply currently outstrips demand so that up to 350,000 tons of glycerol are incinerated in the U.S. annually [5]. Utilizing the surplus of glycerol would render the biodiesel life cycle more environmentally friendly, and enhance the economic viability of the biodiesel supply chain.

1.2   Sustainable use of glycerol surplus

As glycerol production has increased, glycerol has become a reasonably-priced raw material (currently priced at $0.05/lb) [7], and is an attractive precursor for producing value-added chemicals. Some potential products from glycerol include synthetic gas or syngas (H_2/CO gas mixtures), liquid fuels (e.g. methanol, ethanol), and commodity chemicals (e.g. propanediols). Syngas can be directly used in IC systems, or converted to liquid hydrocarbons through the Fischer-Tropsch process [8]. Ethanol can be blended with gasoline. In fact, 95% of U.S. gasoline contains up to 10% ethanol to boost octane and meet air quality requirements [9]. Brazil also blends ethanol with gasoline [10]. Glycerol can be converted into chemicals like aldehydes, acids, or alcohols. As listed in Table 1.1, it can be oxidized to dihydroxyacetone, which is used in an artificial tanning agent, or glyceraldehyde, which is a precursor of cosmetics. Besides, glycerol also can be reduced to compounds like diols, which are used in antifreeze, detergent, or in the manufacture of textile fibers [5].

Table 1.1: List of oxidation and reduction products derived from glycerol [5].

	Name	Molecular structure	Applications
Oxidation products	Dihydroxyacetone (DHA)		• Artificial tanning agent in cosmetics • Feedstock for the synthesis of fine chemicals
	Glyceraldehyde		• Precursor of cosmetics
	Tartronic acid		• Raw materials in pharmacy • Additive in candy, drink, wine • Antiseptic
Reduction	1,2-propanediol (Propylene glycol)		• Functional fluids (antifreeze, deicing, cosmetics, liquid detergent etc.)
	1,3-propanediol		• Copolymer to produce polyester (textile fibers exhibiting chemical resistance)

Various catalytic solutions exist to convert glycerol into valuable products. In fact, there have been numerous reports about the feasibility of converting glycerol into chemicals and gases, from both a thermochemical and an electrochemical standpoint [5]. Some reaction pathways through hydrogenolysis via $C-C$ bond cleavage are illustrated in Figure 1.3. Methanol, ethylene glycol, or 1,3-propanediol were obtained as final products [11]. 1,3-propanediols are currently produced from petroleum derivatives such as ethylene oxide, which provides an opportunity to replace petroleum-based raw materials with biomass-derived feedstocks.

One of the most promising paths for glycerol conversion is liquid phase oxidation. Garcia et al. examined the liquid phase oxidation of glycerol in a thermochemical environment with noble metal catalysts to derive products such as glyceric acid and dihydroxyacetone. The effects of pH and specific catalysts on selectivity were exam-
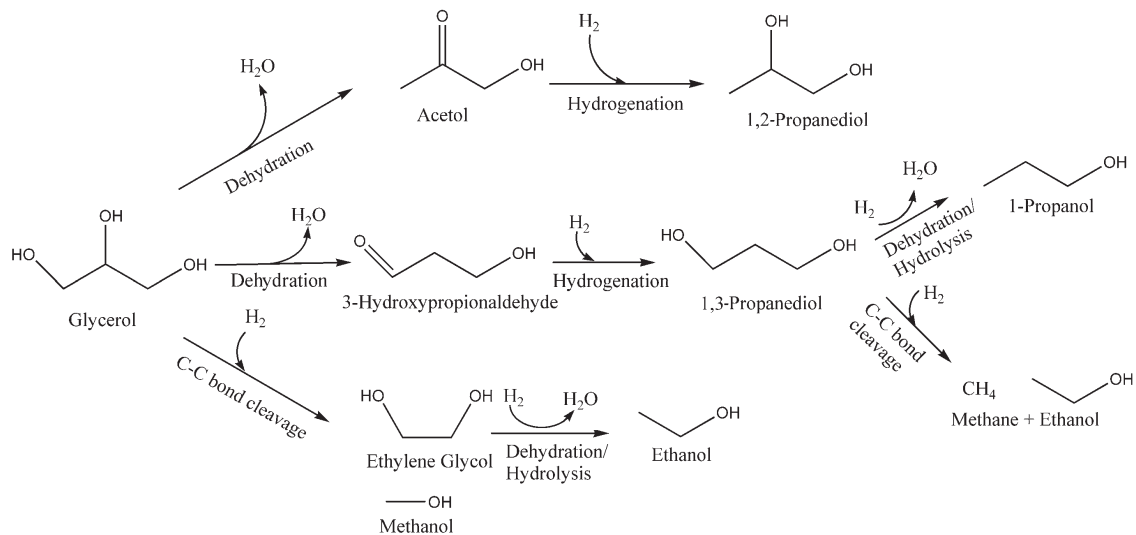
Figure 1.3: Reaction pathways for glycerol hydrogenolysis [11].

ined at atmospheric pressure and at 60 °C, and they demonstrated 70% glyceric acid selectivity with 100% glycerol conversion at pH 11 using 5%Pd/C as a catalyst [12]. Glyceric acid is a building block for chemical synthesis and an intermediate for amino acids. Glycerol oxidation can follow several reaction pathways (Figure 1.4), but each step is generally controllable by managing the catalyst and reaction conditions [13].
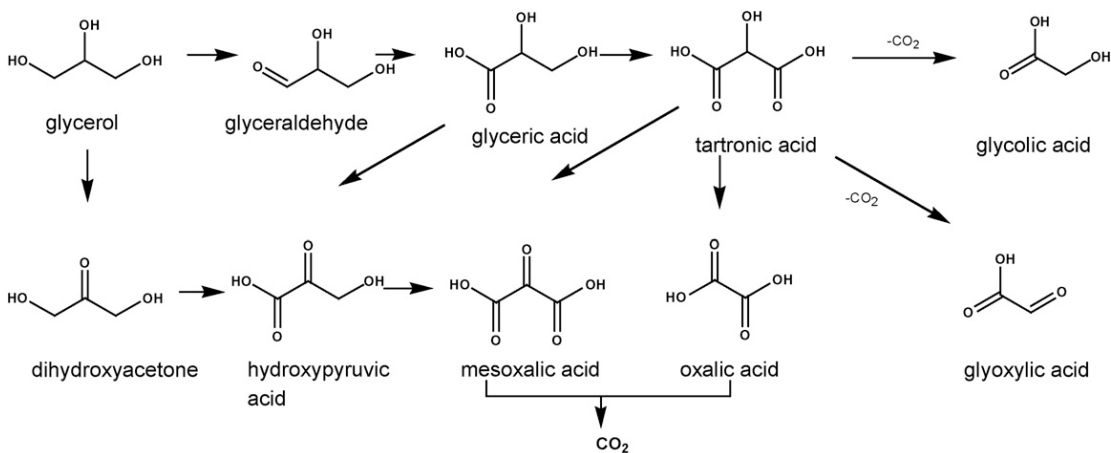
Figure 1.4: Reaction network of glycerol oxidation [13].

5

1.3 Electrooxidation of glycerol

For thermochemical processes, manipulating selectivity and increasing efficiency require changing temperatures and pressures, which can add significantly to the operating costs. Alternatively, electrochemical processes have been intensively studied due to their potential to use electricity from renewable resources. Furthermore, compared to thermochemical conversions, electrochemical processes can be driven at relatively low temperatures and pressures, which could eliminate the need for a heating or pressuring device from the reactor system. In addition, it is possible to alter selectivities by controlling the applied potentials, pH of electrolytes, and choice of electrocatalysts to selectively activate targeted bonds (e.g. C=C, C−H).

There are reports regarding electrooxidation of glycerol [14–21]. Simoes et al. investigated oxidation of glycerol in 1 M NaOH, and obtained glycerate, dihydroxyacetone, and tartronate as the main reaction products with Pt-Bi/C and Pd-Bi/C [18]. Kyriacou et al., Kwon et al., and Mougenot et al. also evaluated the reaction in an alkaline environment (NaOH) with noble-metal catalysts [15, 17, 19], as glycerol oxidation typically shows higher activity in alkaline media [22]. Roquet et al. carried out glycerol oxidation in both 0.1 M NaOH and 0.1 M $HClO_4$ using Pt/C electrocatalysts that resulted in the production of aldehydes and acids at specific applied potentials and pH [16]. The applied potential was one of the key parameters that affected the product selectivities. Roquet et al. complete a quantitative analysis using a high-performance liquid chromatography (HPLC). The results indicated that the oxidation products varied with potential. As shown in Figure 1.5, at 0.75 V versus reversible hydrogen electrode (vs. RHE) in an acid medium, the oxidation process involves platinum sites, which are not yet oxidized. The adsorbed OH species would interact with Pt to oxidize and then desorb as glyceraldehyde, which is desirable for partial oxidation. Conversely, at 1.30 V vs. RHE, the platinum surface forms more stable oxides such as Pt-O. An active oxygen molecule now can interact with a

glycerol molecule and cause C−C bond scission, which leads to formic and glycolic acids.
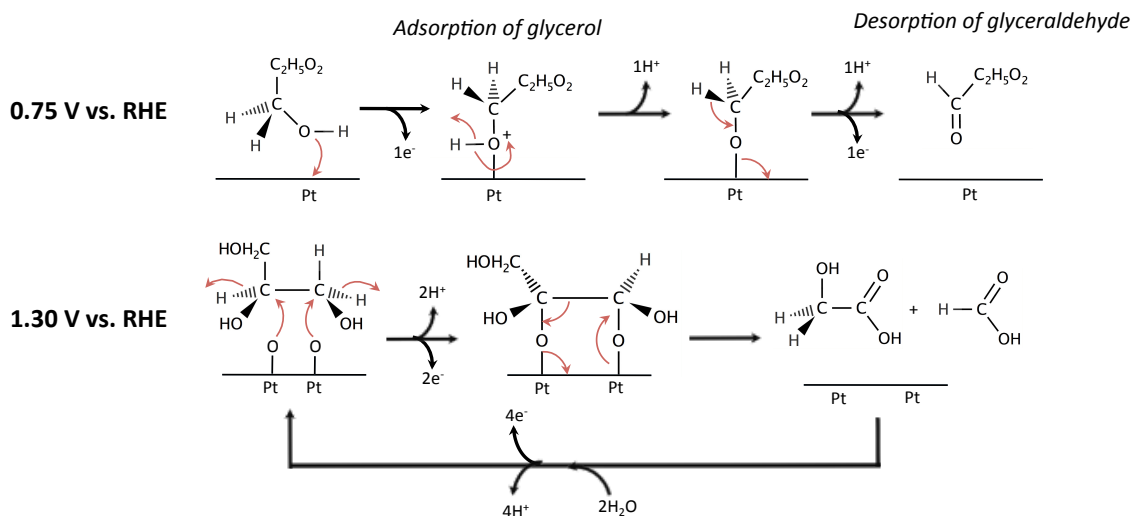
Figure 1.5: Glycerol electrooxidation pathways in acidic medium [16].

More recent studies have been directed towards direct glycerol fuel cells (DGFCs) as a means to utilize surplus glycerol to produce electricity [23–48]. Generally, the focus has been on the complete oxidation of glycerol into CO_2 via C−C bond cleavage, which is not desirable for producing chemicals. Noble metals (e.g. Pd, Pt, Pt-Ru) supported on carbon or various metal oxides were typically used as electrocatalysts in DGFCs [29, 30, 38, 39, 43, 44].

1.4 Solid polymer electrolyte reactor for glycerol oxidation

Electrocatalytic processes provide an alternative strategy for the conversion of glycerol to thermochemical processes. In addition to traditional batch reactors, flow reactors such as the solid polymer electrolyte (SPE) reactor have been studied for various chemical conversions due to their advantage of reducing the number of down-stream separation processes.

One such successful example is the hydrogenation of triglycerides using an SPE

reactor [49, 50]. Triglycerides are the main compounds found in unprocessed vegetable oils and animal fats used for cooking oil, margarine, and soaps. Food-grade vegetable oil is typically hydrogenated to improve stability and spreadability by reducing unsaturated fatty acids. Due to health concerns, it is beneficial to minimize *trans* isomers resulting from the hydrogenation process to avoid the risk of coronary heart disease [51].

The hydrogenation of triglycerides is commercially carried out in a thermochemical stirred batch reactor with a Raney nickel catalyst, at temperatures between 150 and 225 °C and pressures between 10 and 60 psi [52]. This reaction involves three phases: gas (H_2), liquid (triglycerides), and solid (catalyst). This system, however, results in the production of *trans* isomer concentrations as high as 30%. This increase of trans isomers was due to H_2 scarcity near the catalyst surface caused by mass transport limitations of H_2 in the reactor. Partially hydrogenated intermediates would return to trans configurations, as this pathway is more thermodynamically favored than that for cis configuration [52, 53].

In an attempt to overcome this problem, An et al. used an SPE reactor, which resembles a proton exchange membrane (PEM) fuel cell (Figure 1.6) [49]. This reactor design delivers hydrogen to the surface catalyst by dissociatively adsorbing H_2 on the Pt anode and drawing hydrogen through the Nafion® membrane to the cathode catalyst using an applied cell potential. Using this configuration, the authors reported a reduction of *trans* fatty acid content by over 80%, while maintaining the same degree of hydrogenation as compared to the conventional chemical catalytic process. However, the production of undesirable saturated fats (e.g. stearic acid) increased relative to the conventional process [50, 52], and the catalyst used in these demonstrations was palladium, which is quite expensive ($20,550/kg as of November 2012 [54]).

Glycerol oxidation has been evaluated in an SPE reactor [55–59]. Marshall et al. used a PEM type SPE, but their goal was to produce H_2 at the cathode from
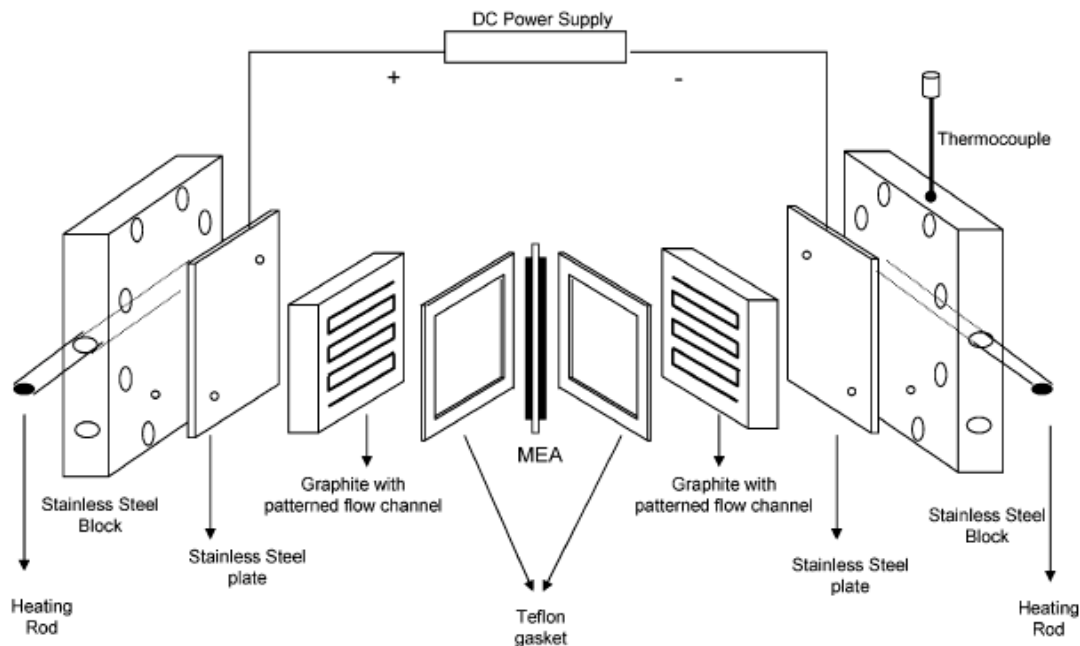
Figure 1.6: Schematic of the electrochemical reactor [50].

glycerol, and the activity and product selectivity at the anode were not well defined [55]. Bambagioni et al. synthesized Pd supported on multi-walled carbon nanotubes (Pd/MWCNT) and Pt-Ru/MWCNT as anode electrocatalysts and tested then for glycerol oxidation in an anion-exchange membrane (AEM) reactor [56]. The use of an AEM as an SPE indicates that the reaction pathways involved hydroxyls (Figure 1.7) as opposed to protons in a PEM. Their NMR analysis on anode exhausts from the AEM reactor indicated the formation of glycolate, glycerate, tartronate, oxalate, formate, and carbonate, with glycerate showing the highest yield. Lux et al. combined an electrochemical reactor with a thermocatalytic convertor to achieve a highly selective process for lactic acid production from glycerol [57]. Ilie et al. also evaluated glycerol oxidation using an AEM reactor for energy production and cogeneration of chemicals [58]. They used various anode electrocatalysts (e.g. Pt/C, Pd/C, Pt_9Bi_1/C, Pd_9Bi_1/C), and found that Pt_9Bi_1/C showed the best performance. They also tested the reaction by varying other parameters such as glycerol concentration, flow rate, or cell temperature, most of which had a great influence on the performance.

9

Most recently, Zhang et al. used HPLC analysis and showed the presence of various acids, including glyceric acid, tartronic acid, mesoxalic acid, glycolic acid and oxalic acid as a result of glycerol oxidation in an AEM reactor using Pt/C [59].
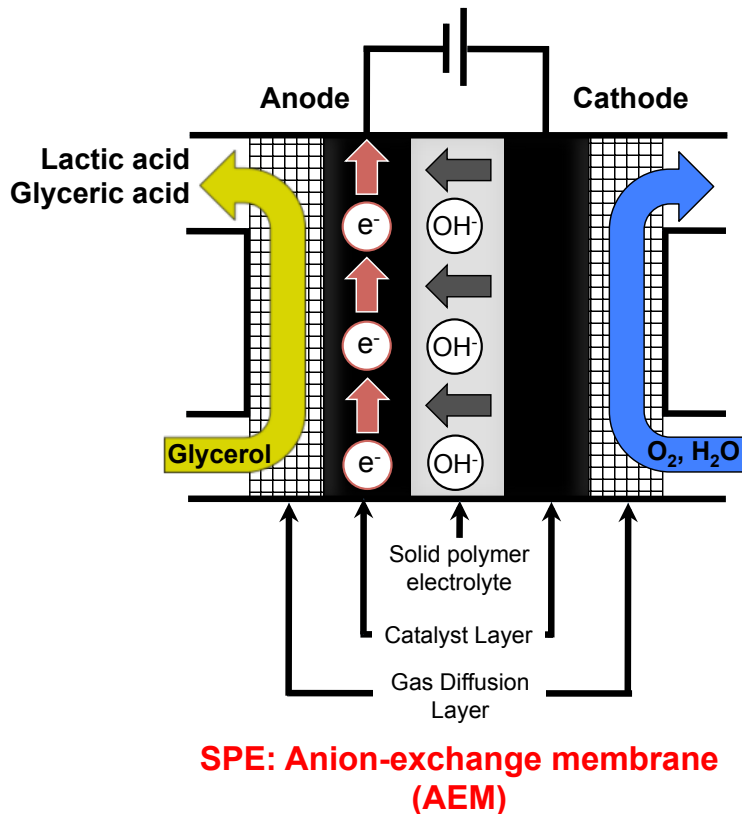
Figure 1.7: Schematic of the AEM reactor.

As mentioned in section 1.3, glycerol oxidation could lead to the use of glycerol as fuel for SPE fuel cells [23–48]. However, most of these electrocatalyst evaluations have been done only in liquid electrolytes despite the eventual intention to use glycerol in SPE fuel cells. This poses the question whether liquid electrolytes are an accurate model for the SPE reactor, as quite different chemistries have been reported at the Nafion® interface compared to those in liquid electrolytes (e.g. H_2SO_4) [60].

1.5 Transition metal carbide electrocatalysts

A key challenge for the electrocatalytic process is the need for low-cost catalysts for the electrooxidation of glycerol. Early transition metal carbide catalysts are typically synthesized from oxides via temperature-programmed carburization. They are attractive candidates because their raw materials are inexpensive: for example, current prices as of 2012 are \$41/kg for Nb_2O_5, and \$0.42/kg for WO_3 [61]. The resulting carbides often adopt simple crystal structures with the metal atoms forming lattices of face-centered cubic (fcc) or hexagonal close packed (hcp) structure, and the non-metallic elements (e.g. C) enter into the interstitial sites between metal atoms as schematically shown in Figure 1.8.

(a) Face-centered cubic
NbC, VC

(b) Hexagonal close packed
Mo_2C, W_2C
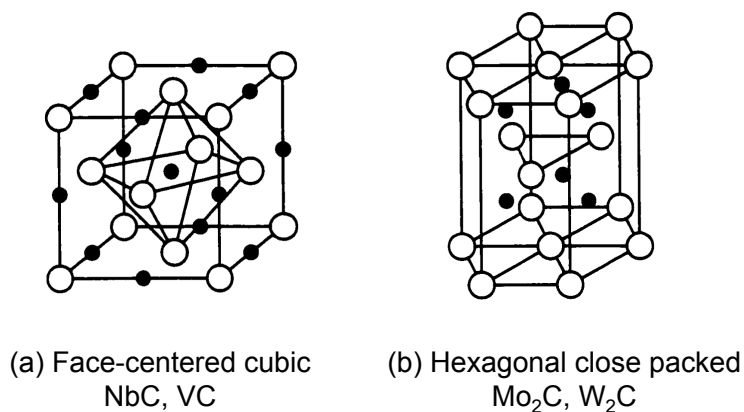
Figure 1.8: Crystal structures for transition metal carbides (a) NbC and VC, (b) Mo_2C and W_2C [62].

Some transition metal carbides have demonstrated catalytic properties that resemble those of Pt group metals [63]. They are also active for many reactions, such as water gas shift [64], methanol steam reforming [65] and benzene hydrogenation [66]. Transition-metal carbides can also be used as supports for the noble-metal catalysts because they can be synthesized with a relatively high surface area [67]. For example, molybdenum carbide (Mo_2C) has shown surface areas of up to 150 m^2/g as a result of temperature-programmed carburization from an oxide precursor [67, 68]. In ad-

dition, transition metal carbides have low electrical resistivities, and are classified as conductors (Table 1.2) [69]. They are typically less conductive than their pure metals, but this characteristic makes some carbides desirable for use in electrochemical applications.

Table 1.2: Electrical resistivity of elements and compounds at room temperature [69].

Element	Electrical resistivity ($\mu\Omega$ cm)
Mo	5.47
Mo_2C	71
W	5.39
WC	22
SiC	10^3
Al_2O_3	10^{18}
C (diamond)	10^{18}

1.6 Research goals and organization of text

The electrooxidation of glycerol has several potential advantages compared to the thermochemical process in terms of the ability to tune selectivities toward the desirable products. We propose the electrooxidation of glycerol in an SPE reactor to produce commodity chemicals. Glycerol electrooxidation has mainly been studied in alkaline medium or AEM reactors. Selective glycerol oxidation using a PEM reactor (e.g. Nafion$^{\circledR}$) has not been reported to the best of our knowledge.

We selected a PEM as the electrolyte over a liquid acidic electrolyte because SPEs seem to provide better selectivity for the mobile ionic species that could be transported across the electrolyte. If the reaction involves an liquid electrolyte instead of a PEM, both cation and anion species are mobile so that they compete for active sites, resulting in undesired side reactions. Furthermore, according to previous findings, the pH of the electrolyte or type of SPE (e.g AEM vs. PEM) can play an important role in terms of activities and selectivities, yielding a different set of products [16, 57].

Finally, as shown in Figure 1.7, it is possible to cogenerate H_2 at the cathode in addition to valuable chemicals at the anode with a PEM reactor, which could add more value to this process.
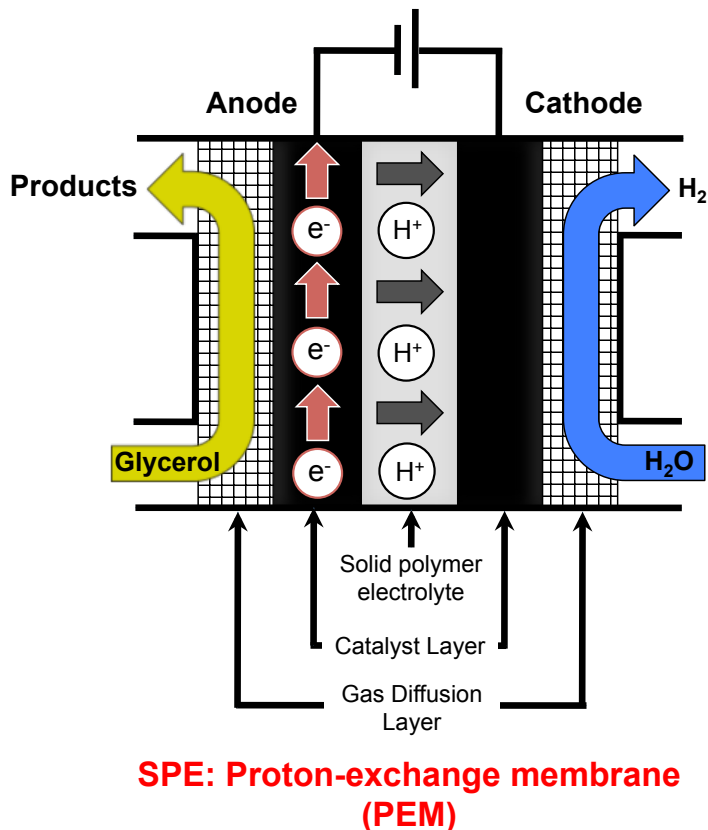
Figure 1.9: Schematic of PEM reactor.

To understand this reaction, the effects of applied potentials and the choice of anode electrocatalysts on the activity and selectivity were investigated. One of the major challenges for the electrochemical process in general is to reduce the use of high-cost noble metals, which are typically susceptible to CO poisoning, as electrocatalysts (e.g Pt). This presents an opportunity for finding low-cost and poison-resistant materials for the electrooxidation of glycerol.

Chapter 2 describes the synthesis procedures for transition-metal-carbide-supported catalysts and various characterization techniques employed in this work. The electrochemical characterization, glycerol oxidation performance evaluation using a PEM

reactor, and post-reaction characterization are also discussed.

Chapter 3 focuses on the functional properties of various catalysts, including noble metal, or transition-metal-carbide-supported Pt, for the electrooxidation of glycerol in a PEM reactor. In addition, a novel electroanalytical technique that can be used in understanding the characteristics of glycerol oxidation at Nafion® interfaces as opposed to interfaces with acidic liquid electrolytes is described.

In Chapter 4, mechanistic studies for this reaction are described with the aim of defining the reaction pathway, and identifying the rate-determining steps. This involves evaluation of the reaction order, characterization of reaction intermediates as well as their adsorption behavior, and measurement of overpotential as a function of current.

Finally, understanding and preventing deactivation of electrocatalysts is currently one of the major goals in fuel cell or electro-synthesis research, and that is covered in Chapter 5.

References

[1] Annual energy outlook 2010, Energy Information Administration, U.S. Department of Energy DOE/EIA-0383 (2010).

[2] C. A. Miller, Characterizing emissions from the combustion of biofuels, U.S. Environmental Protection Agency EPA/600/R-08/069 (2008).

[3] Renewable energy consumption and electricity preliminary statistics 2008, Energy Information Administration, U.S. Department of Energy (2009).

[4] Monthly energy review january 2012, Energy Information Administration, U.S. Department of Energy DOE/EIA-0035(2012/01) (2012).

[5] Y. Zheng, X. Chen, Y. Shen, Commodity chemicals derived from glycerol, an important biorefinery feedstock, Chem Rev 108 (2008) 5253–5277.

[6] F. Shahidi, Bailey's industrial oil and fat products, John Wiley & Sons 3 (2005) 555–565.

[7] Regulatory impact analysis: Renewable fuel standard program, United States Environmental Protection Agency EPA420-R-07-004 (2007) 1–62.

[8] D. A. Simonetti, J. Rass-Hansen, E. L. Kunkes, R. R. Soares, J. A. Dumesic, Coupling of glycerol processing with fischer-tropsch synthesis for production of liquid fuels, Green Chemistry 9 (2007) 1073–1083.

[9] Fuel economy guide, Office of Energy Efficiency and Renewable Energy U.S. Department of Energy, U.S. Environmental Protection Agency DOE/EE-0778 (2013).

[10] G. Huber, S. Iborra, A. Corma, Synthesis of transportation fuels from biomass: chemistry, catalysts, and engineering, Chem Rev 106 (2006) 4044–4098.

[11] T. Miyazawa, Y. Kusunoki, K. Kunimori, K. Tomishige, Glycerol conversion in the aqueous solution under hydrogen over ru/c plus an ion-exchange resin and its reaction mechanism, Journal of Catalysis 240 (2006) 213–221.

[12] R. Garcia, M. Besson, P. Gallezot, Chemoselective catalytic oxidation of glycerol with air on platinum metals, Applied Catalysis A: General 127 (1995) 165–176.

[13] S. Demirel, K. Lehnert, M. Lucas, P. Claus, Use of renewables for the production of chemicals: Glycerol oxidation over carbon supported gold catalysts, Applied Catalysis B: Environmental 70 (2007) 637–643.

[14] R. Gonçalves, W. Triaca, T. Rabockai, The potentiodynamic electrooxidation of glycerol on platinized platinum electrodes, Analytical Letters 18 (1985) 957–973.

[15] D. Kyriacou, T. Tougas, Preparation of glyceric acid by anodic oxidation of glycerol at a silver oxide electrode, J Org Chem 52 (1987) 2318–2319.

[16] L. Roquet, E. Belgsir, J. Leger, C. Lamy, Kinetics and mechanisms of the electrocatalytic oxidation of glycerol as investigated by chromatographic analysis of the reaction-products - potential and ph effects, Electrochim Acta 39 (1994) 2387–2394.

[17] Y. Kwon, M. T. M. Koper, Combining voltammetry with hplc: Application to electro-oxidation of glycerol, Anal. Chem. 82 (2010) 5420–5424.

[18] M. Simoes, S. Baranton, C. Coutanceau, Enhancement of catalytic properties for glycerol electrooxidation on pt and pd nanoparticles induced by bi surface modification, Appl Catal B-Environ 110 (2011) 40–49.

[19] M. Mougenot, A. Caillard, M. Simoes, S. Baranton, C. Coutanceau, P. Brault, Pdau/c catalysts prepared by plasma sputtering for the electro-oxidation of glycerol, Appl Catal B-Environ 107 (2011) 372–379.

[20] Y. Kwon, Y. Birdja, I. Spanos, P. Rodriguez, M. T. M. Koper, Highly selective electro-oxidation of glycerol to dihydroxyacetone on platinum in the presence of bismuth, Acs Catal 2 (2012) 759–764.

[21] J. Gomes, F. Paula, L. Gasparotto, G. Tremiliosi-Filho, The influence of the pt crystalline surface orientation on the glycerol electro-oxidation in acidic media, Electrochim Acta 76 (2012) 88–93.

[22] B. Beden, I. Cetin, A. Kahyaoglu, D. Takky, C. Lamy, Electrocatalytic oxidation of saturated oxygenated compounds on gold electrodes, Journal of Catalysis 104 (1987) 37–46.

[23] M. Avramov-Ivic, J. M. Leger, C. Lamy, V. Jovic, S. Petrovic, The electro-oxidation of glycerol on the gold (100)-oriented single-crystal surface and poly-crystalline surface in 0.1 m naoh, Journal of electroanalytical chemistry and interfacial electrochemistry 308 (1991) 309–317.

[24] M. Avramov-Ivic, J. Léger, B. Beden, F. Hahn, C. Lamy, Adsorption of glycerol on platinum in alkaline medium: effect of the electrode structure, J. Electroanal. Chem. 351 (1993) 285–297.

[25] G. Yildiz, F. Kadirgan, Synergistic effect in the electrocatalytic oxidation of glycerol on platinum-palladium alloy electrodes, Ann Chim-Rome 84 (1994) 455–465.

[26] E. Venancio, W. Napporn, A. Motheo, Electro-oxidation of glycerol on platinum dispersed in polyaniline matrices, Electrochim Acta 47 (2002) 1495–1501.

[27] K. Matsuoka, M. Inaba, Y. Iriyama, T. Abe, Z. Ogumi, M. Matsuoka, Anodic oxidation of polyhydric alcohols on a pt electrode in alkaline solution, Fuel Cells 2 (2002) 35–39.

[28] G. Hutchings, S. Carrettin, P. McMorn, P. Jenkins, G. Attard, P. Johnston, K. Griffin, C. Kiely, Cyclic voltammetry as a potential predictive method for supported nanocrystalline gold catalysts for oxidation in aqueous media, ACS Symposium Series 921 (2006) 82–98.

[29] A. N. Grace, K. Pandian, Pt, pt-pd and pt-pd/ru nanoparticles entrapped polyaniline electrodes - a potent electrocatalyst towards the oxidation of glycerol, Electrochemistry Communications 8 (2006) 1340–1348.

[30] J. H. Kim, S. M. Choi, S. H. Nam, M. H. Seo, S. H. Choi, W. B. Kim, Influence of sn content on ptsn/c catalysts for electrooxidation of c1-c3 alcohols: Synthesis, characterization, and electrocatalytic activity, Appl Catal B-Environ 82 (2008) 89–102.

[31] J. Xi, J. Wang, L. Yu, X. Qiu, L. Chen, Facile approach to enhance the pt utilization and co-tolerance of pt/c catalysts by physically mixing with transition-metal oxide nanoparticles, Chem Commun (2007) 1656–1658.

[32] A. Y. Tsivadze, M. R. Tarasevich, V. A. Bogdanovskaya, M. R. Ehrenburg, Platinum-free nanosize electrocatalysts for glycerol oxidation, Dokl Chem 419 (2008) 54–56.

[33] C. Xu, Z. Tian, P. Shen, S. P. Jiang, Oxide (ceo2, nio,co3o4and mn3o4)-promoted pd/c electrocatalysts for alcohol electrooxidation in alkaline media, Electrochim Acta 53 (2008) 2610–2618.

[34] C. Bianchini, P. Shen, Palladium-based electrocatalysts for alcohol oxidation in half cells and in direct alcohol fuel cells, Chem Rev 109 (2009) 4183–4206.

[35] N. R. Stradiotto, K. E. Toghill, L. Xiao, A. Moshar, R. G. Compton, The fabrication and characterization of a nickel nanoparticle modified boron doped diamond electrode for electrocatalysis of primary alcohol oxidation, Electroanal 21 (2009) 2627–2633.

[36] L. Su, W. Jia, A. Schempf, Y. Lei, Palladium/titanium dioxide nanofibers for glycerol electrooxidation in alkaline medium, Electrochemistry Communications 11 (2009) 2199–2202.

[37] D. Jeffery, G. Camara, The formation of carbon dioxide during glycerol electrooxidation in alkaline media: First spectroscopic evidences, Electrochemistry Communications 12 (2010) 1129–1132.

[38] M. Simoes, S. Baranton, C. Coutanceau, Electro-oxidation of glycerol at pd based nano-catalysts for an application in alkaline fuel cells for chemicals and energy cogeneration, Appl Catal B-Environ 93 (2010) 354–362.

[39] H. Kim, S. Choi, S. Green, G. Tompsett, S. Lee, G. Huber, W. Kim, Highly active and stable ptrusn/c catalyst for electrooxidations of ethylene glycol and glycerol, Applied Catalysis B: Environmental 101 (2011) 366–375.

[40] H. J. Kim, S. M. Choi, M. H. Seo, S. Green, G. W. Huber, W. B. Kim, Efficient electrooxidation of biomass-derived glycerol over a graphene-supported ptru electrocatalyst, Electrochemistry Communications 13 (2011) 890–893.

[41] S. Xie, S. Chen, Z. Liu, C. wei Xu, Comparison of alcohol electrooxidation on pt and pd electrodes in alkaline medium, Int. J. Electrochem. Sci 6 (2011) 882–888.

[42] J. F. Gomes, G. Tremiliosi-Filho, Spectroscopic studies of the glycerol electrooxidation on polycrystalline au and pt surfaces in acidic and alkaline media, Electrocatalysis 2 (2011) 96–105.

[43] A. Falase, M. Main, K. Garcia, A. Serov, C. Lau, P. Atanassov, Electrooxidation of ethylene glycol and glycerol by platinum-based binary and ternary nano-structured catalysts, Electrochim Acta 66 (2012) 295–301.

[44] J. hua Zhang, Y. jun Liang, N. Li, Z. ying Li, C. wei Xu, S. P. Jiang, A remarkable activity of glycerol electrooxidation on gold in alkaline medium, Electrochim Acta 59 (2012) 156–159.

[45] L. Artem, D. Santos, A. de Andrade, K. Kokoh, J. Ribeiro, Development of ternary and quaternary catalysts for the electrooxidation of glycerol, The Scientific World Journal 2012 (2012) 1–6.

[46] P. S. Fernandez, M. E. Martins, G. A. Camara, New insights about the electrooxidation of glycerol on platinum nanoparticles supported on multi-walled carbon nanotubes, Electrochim Acta 66 (2012) 180–187.

[47] P. S. Fernandez, M. E. Martins, C. A. Martins, G. A. Camara, The electrooxidation of isotopically labeled glycerol on platinum: New information on c-c bond cleavage and co2 production, Electrochemistry Communications 15 (2012) 14–17.

[48] J.-H. Song, J.-Y. Yu, M.-Z. Zhang, Y. jun Liang, C. wei Xu, Glycerol electrooxidation on au/ni core/shell three-dimensional structure catalyst, Int J Electrochem Sc 7 (2012) 4362–4368.

18

[49] W. An, J. Hong, P. Pintauro, K. Warner, W. Neff, The electrochemical hydrogenation of edible oils in a solid polymer electrolyte reactor. i. reactor design and operation, Journal of the American Oil Chemists' Society 75 (1998) 917–925.

[50] P. Pintauro, M. Gil, K. Warner, G. List, W. Neff, Electrochemical hydrogenation of soybean oil with hydrogen gas, Ind Eng Chem Res 44 (2005) 6188–6195.

[51] A. Ascherio, M. Katan, P. Zock, M. Stampfer, W. Willett, Trans fatty acids and coronary heart disease, New Engl J Med 340 (1999) 1994–1998.

[52] R. Hastert, Practical aspects of hydrogenation and soybean salad oil manufacture, Journal of the American Oil Chemists' Society 58 (1981) 169–174.

[53] R. Allen, A. Kiess, Isomerization during hydrogenation. 1. oleic acid, Journal of the American Oil Chemists' Society 32 (1955) 400–405.

[54] U.s. geological survey: Mineral industry surveys, U.S. Department of the Interior (2013).

[55] A. Marshall, R. Haverkamp, Production of hydrogen by the electrochemical reforming of glycerol–water solutions in a pem electrolysis cell, Int J Hydrogen Energ 33 (2008) 4649–4654.

[56] V. Bambagioni, C. Bianchini, A. Marchionni, J. Filippi, F. Vizza, J. Teddy, P. Serp, M. Zhiani, Pd and pt-ru anode electrocatalysts supported on multi-walled carbon nanotubes and their use in passive and active direct alcohol fuel cells with an anion-exchange membrane (alcohol = methanol, ethanol, glycerol), J Power Sources 190 (2009) 241–251.

[57] S. Lux, P. Stehring, M. Siebenhofer, Lactic acid production as a new approach for exploitation of glycerol, Separ Sci Technol 45 (2010) 1921–1927.

[58] A. Ilie, M. Simoes, S. Baranton, C. Coutanceau, S. Martemianov, Influence of operational parameters and of catalytic materials on electrical performance of direct glycerol solid alkaline membrane fuel cells, J Power Sources 196 (2011) 4965–4971.

[59] Z. Zhang, L. Xin, W. Li, Electrocatalytic oxidation of glycerol on pt/c in anion-exchange membrane fuel cell: Cogeneration of electricity and valuable chemicals, Appl Catal B-Environ 119 (2012) 40–48.

[60] J. Jiang, A. Kucernak, Investigations of fuel cell reactions at the composite microelectrode vertical bar solid polymer electrolyte interface. i. hydrogen oxidation at the nanostructured pt vertical bar nafion(r) membrane interface, J Electroanal Chem 567 (2004) 123–137.

[61] U.s. geological survey: Commodity statistics and information, U.S. Department of the Interior (2012).

19

[62] C. A. Bennett, Influence of nanostructure and composition on the catalytic properties of mono and bimetallic nitrides, Dissertation, University of Michigan (2002) 1–415.

[63] R. Levy, M. Boudart, Platinum-like behavior of tungsten carbide in surface catalysis, Science 181 (1973) 547–549.

[64] J. Patt, D. Moon, C. Phillips, L. Thompson, Molybdenum carbide catalysts for water-gas shift, Catal Lett 65 (2000) 193–195.

[65] S. Lin, W. Thomson, T. Hagensen, S. Ha, Steam reforming of methanol using supported mo2c catalysts, Applied Catalysis A: General 318 (2007) 121–127.

[66] A. Rocha, V. Dasilva, A. Farojr, Carbided y zeolite-supported molybdenum: On the genesis of the active species, activity and stability in benzene hydrogenation, Applied Catalysis A: General 314 (2006) 137–147.

[67] W. Setthapun, S. Bej, L. Thompson, Carbide and nitride supported methanol steam reforming catalysts: Parallel synthesis and high throughput screening, Topics in Catalysis 49 (2008) 73–80.

[68] S. T. Oyama, Preparation and catalytic properties of transition-metal carbides and nitrides, Catal Today 15 (1992) 179–200.

[69] S. Oyama, The chemistry of transition metal carbides and nitrides: 1st edition, Springer (1996).

CHAPTER II

Experimental Methods

2.1 Introduction

This chapter describes experimental techniques designed to help address the objectives described in section 1.6. Key aspects of the experimental include catalyst synthesis, catalyst characterization and screening, performance evaluation in a PEM reactor, liquid/gas product analysis using gas chromatography, and post-reaction characterization of spent materials (Figure 2.1).

| Catalyst synthesis | → | Catalyst characterization and screening | → | Evaluation in a PEM reactor | → | Product analysis | → | Post-reaction characterization |
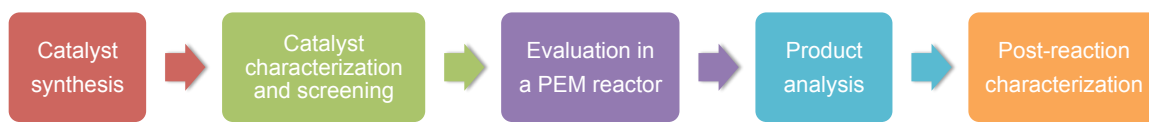
Figure 2.1: Overall experimental procedure.

To evaluate the feasibility of using carbide-supported electrocatalysts, we synthesized various transition-metal carbides. The prepared catalysts were characterized using various techniques, such as N_2 physisorption or x-ray diffraction, to ensure the syntheses were done successfully. Catalyst screening was conducted in a solid-state cell by examining the electrochemical activity and stability at a Nafion® interface. The selected catalysts were then evaluated in an SPE reactor. The liquid and gas products were analyzed using a gas chromatograph equipped with a flame ioniza-

tion detector, a thermal conductivity detector, and a mass spectrometer. Finally, post-reaction characterization was performed on the spent catalysts and membrane electrode assemblies to investigate the deactivation mechanisms.

2.2 Catalyst synthesis

2.2.1 Materials

Carbon-supported noble metals (20 wt%Pt/C (Alfa Aesar), 20 wt%Pt-10 wt%Ru/C (Alfa Aesar), Pt-black (Alfa Aesar), and Ru-black (Sigma-Aldrich)), were used as received. All of the carbides and nitrides were synthesized from oxide precursors: Nb_2O_5 (Alfa Aesar), WO_3 (Alfa Aesar). The metal loading precursor used for carbides and nitrides-supported catalysts was $H_2PtCl_6 \cdot 6\,H_2O$ (Sigma-Aldrich).

2.2.2 Preparation of carbide and carbide supported catalysts

Transition metal carbides were synthesized using the temperature-programmed reaction (TPR) with 15% CH_4 in H_2 (15% CH_4/H_2, Cryogenic Gases, certified mixture) from oxide precursors. The use of TPR has been discussed previously for the synthesis of various carbide materials [1–4]. Details regarding preparation of the carbides and carbide-supported Pt are described below.

NbC: The NbC catalyst was synthesized based on the procedure described previously [1]. Approximately 0.4 g of Nb_2O_5 was reduced and carburized in a quartz tube reactor with 260 ml/min of 15% CH_4/H_2 gas mixture. The heating rate was 7.5 °C/min from room temperature to 1100 °C, followed by soaking at 1100 °C for 1 hour.

W_2C: The W_2C catalyst was synthesized using the procedure described previously [2]. Approximately 1.1 g of WO_3 was reduced and carburized in a quartz tube reactor

with 250ml/min of 15% CH_4/H_2 gas mixture. The heating rate was 10.3 °C/min starting from room temperature to 200 °C. The heating rate was then switched to 1.0 °C/min from 200 °C to 650 °C, followed by soaking at 500 °C for 5 hours.
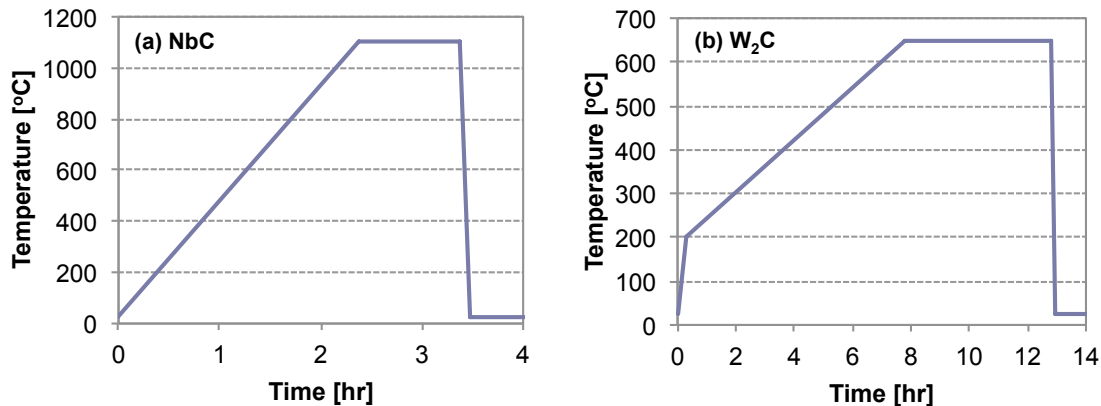
Figure 2.2: Temperature program profiles for (a) NbC and (b) W_2C.

Carbide-supported Pt: The carbide-supported Pt catalysts were prepared by first synthesizing carbides using the procedure described above, followed by wet impregnation [5]. Synthesized carbides were placed into the deaerated and deionized water containing $H_2PtCl_6 \cdot 6\,H_2O$ without exposure to the air. The solution was stirred for 3 hours at room temperature with continuously bubbling with N_2 gas. The resulting materials were dried in a quartz tube reactor with H_2 (Cryogenic Gases, pre-purified) using a heating rate of 1.9 °C/min starting from room temperature to 110 °C, followed by soaking at 110 °C for 2 hours, and then a heating rate of 5.7 °C/min starting from 110 °C to 450 °C, followed by soaking at 450 °C for 4 hours. The resulting material was finally passivated using a 1% O_2/He (Cryogenic Gases, certified mixture) for 5 hours at room temperature.

2.3 Catalyst characterization

2.3.1 N$_2$ physisorption surface area measurement

The physisorption method was used to measure the surface area of electrocatalysts. This method is described by Brunauer, Emmett and Teller, and often called as the BET method [6]. Currently, the BET method is the most popular for determining surface areas from isotherms. Its derivation was based on the assumptions that multimolecular adsorption is related to condensation, and that the isotherm equation for multimolecular adsorption follows Langmuir's treatment of the unimolecular layer. With these simplifying assumptions, they derived an equation (Equation 2.1) that represented isotherms, and could be used to determine the average heat of adsorption in the first layer and volumes of gas required to form a unimolecular layer on the adsorbents:

$$\frac{P/P_0}{n(1 - P/P_0)} = \frac{1}{n_m C} + \frac{(C - 1)P/P_0}{n_m C} \qquad \text{Isotherm} \qquad (2.1)$$

$$C = \exp\left(\frac{q^1 - q^L}{RT}\right) \qquad (2.2)$$

where n is moles of the adsorbate, n_m is moles in the monolayer, P_0 is the saturation pressure, q^1 is the heat of adsorption in the first layer, and q^L is the heat of liquefaction.

Nitrogen (Cryogenic Gases, pre-purified) gas was used with an ASAP 2010 Physisorption Analyzer (Micromeritics Instrument) to obtain the adsorption isotherms. 0.05 to 0.1 g of the catalyst was placed in the sample tube along with an inner rod and sealing cap. First, the tube was installed to the degassing compartment to remove adsorbed moisture or contaminants from the catalyst. The degassing process was initially conducted at room temperature until the pressure indicator read below 5 mmHg, and the tube was then heated to 300 °C and held at that temperature for

2 hours at below 5 mmHg. After cooling, the tube was installed into the analysis compartment located above a liquid nitrogen dewar for N_2 physisorption. Plotting the left-hand side of Equation 2.1 versus P/P_0 yields a linear region between the relative pressures of 0.05 and 0.20. The number of adsorbed N_2 atoms (n_m) in the monolayer was obtained from the slope and the intercept from Equation 2.1. Once n_m was calculated, we obtained the surface area of the substrate by multiplying n_m by the area covered by unit N_2 atom [7].

2.3.2   X-ray diffraction analysis

X-ray diffraction (XRD) analysis was used to determine the crystal structure of the electrocatalysts. The x-rays used in diffraction experiments are monochromatic.

A Miniflex X-ray diffractometer (Rigaku) was used with $K\alpha$ radiation emitted from Cu (λ=1.5418 Å) with a Ni filter. The filter was used to isolate the $K\alpha$ line for diffraction experiments because the $K\alpha$ is the most intense. When crystals diffract x-rays, the atoms or ions act as secondary point sources and scatter the x-rays. Bragg's law is often used as a simplified treatment to describe this diffraction by crystals:

$$n\lambda = 2d \ sin\theta_B \tag{2.3}$$

where n is an integer, λ is the wavelength of the x-ray, d is the d-spacing, and θ_B is Bragg's angle. The diffractometer scans a range of 2θ values at constant angular velocity. The electrocatalyst (powder form) was analyzed for the 2θ range from $10°$ to $90°$, with a constant angular velocity of $4°$/min. A monochromatic x-ray beam hit the powder as the detector recorded the diffraction pattern. The powder sample, as opposed to a single crystal, consisted of randomly arranged crystals with various lattice planes, and diffraction occurs at these crystals and planes. A diffraction pattern includes the relative intensity at each d-spacing, which is unique to each

material. The results are often used to identify unknown samples, or to confirm lab-synthesized materials with the Powder Diffraction File (PDF). JADE Software (Materials Data) which is capable of matching diffraction patterns in the International Center for Diffraction Data, USA (ICDD) PDF database, was employed to analyze diffraction patterns.

2.3.3   Scanning electron microscopy analysis

Scanning Electron Microscopy (SEM) was used to visualize the surface morphology and to estimate the size of the electrocatalyst. SEM can be used to study structure over a range of 10 nm to 100 μm. Electrons from the electron gun scan a small spot (50 to 100 $\mathring{A}$ in a diameter) on a sample surface. Both x-rays and secondary electrons are emitted. X-rays are used for chemical analysis such as energy-dispersive x-ray spectroscopy (EDX) for mapping the distribution of the elements of interest. The secondary electrons are used to construct an image of the sample surface displayed on a screen.

A Philips XL 30 SEM (FEI Company) equipped with an energy-dispersive x-ray spectrometer was used. The SEM and EDX were both controlled via computers for setting electron beam strength or magnification. The catalyst powder was placed onto copper tape for analysis.

This method was also used to characterize spent catalysts to examine any change in morphology that occurred during the reaction.

2.3.4   Inductively coupled plasma elemental analysis

An inductively coupled plasma-optical emission spectrometer (ICP-OES) was used to quantify the weight percentage of the loaded metal on the carbide support. Optical-emission spectroscopy with high-temperature atomization sources (e.g., plasma) can determine the concentration of about 70 elements. When a substance is excited by

plasma or an electrical discharge, its elements emit light at specific wavelengths (Table 2.1). The light is dispersed by a grating or prism monochromator, and its spectral lines are recorded in the computer [8].

Table 2.1: Sensitive lines of the selected elements [8].

Element	Sensitivity[1]	Wavelength [nm]
Pt	U1	265.95
Pt	U1	306.47
Pt	U3	283.03
Pt	U3	292.98
Nb	U1	405.89
Nb	U2	407.97
Nb	U3	410.09
Nb	U4	412.38
W	U1	430.21
W	U2	407.43
W	U4	272.44
W	U5	294.44

[1] In the column headed Sensitivity, the most sensitive line is indicated by U1, and other lines by U2, U3, and so on, in order of decreasing sensitivity.

The inductively coupled plasma (ICP) is formed by ionizing a flowing stream of argon, producing argon ions and electrons. The movement of the electrons and argon ions creates resistive heating, which leads to high temperatures in the plasma, providing better atomization and more highly populated excited states than are possible using flame ionization. The ICP torch consists of three concentric quartz tubes, surrounded at the top by a radio-frequency induction coil. The sample is mixed with a stream of Ar using a spray chamber nebulizer, and is carried to the plasma through the torch's central tube. An alternating radio frequency current in the induction coils creates a fluctuating magnetic field that induces the argon ions and electrons to move in a circular path. The resulting collisions with the abundant non-ionized gas induce high temperatures (6000 to 8000 K) at a height of 15 - 20 mm above the the coils, where emission is usually measured [9].
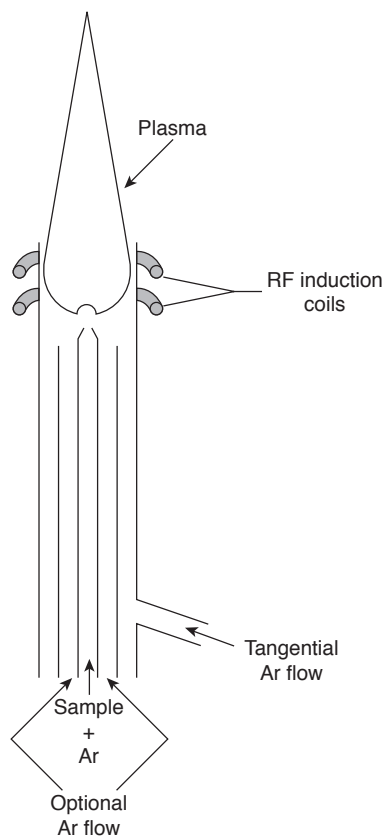
Figure 2.3: Schematic of ICP torch [9].

A 710-ES ICP-OES (Varian) was controlled with ICP Expert II software for auto sampling and data acquisition. For sample preparation, 15 mg of a carbide-supported catalyst was dissolved into 3 mL of aqua regia ($HCl : HNO_3 = 3 : 1$, Fisher Scientific, certified ACS Plus) overnight in a fume hood. Then 1 mL of the dissolved solution was diluted with 13 mL of H_2O in a plastic tube. This sample was replicated to verify the accuracy of the measurement. Typically, four tubes for each catalyst were prepared for one measurement. To determine the concentration, standard solutions (Inorganic Ventures) with six known Pt concentrations were prepared, including one blank (pure water) and five standards of varying concentrations.

2.3.5 Electrochemical characterization using a solid-state cell

One of the novel methods employed in this work is the solid-state cell used for the initial active-metal screening and characterization. This cell allows us to assess the electrocatalyst's activity and stability by evaluating its characteristics during cyclic voltammetry (CV). This method is less time consuming than performing the actual experiment in a PEM reactor, which makes a solid-state cell ideal for initial catalyst screening.

Catalyst screening and characterization for electrochemical reaction has been traditionally conducted in a three-electrode glass compartment cell (Figure 2.4) filled with a liquid electrolyte.
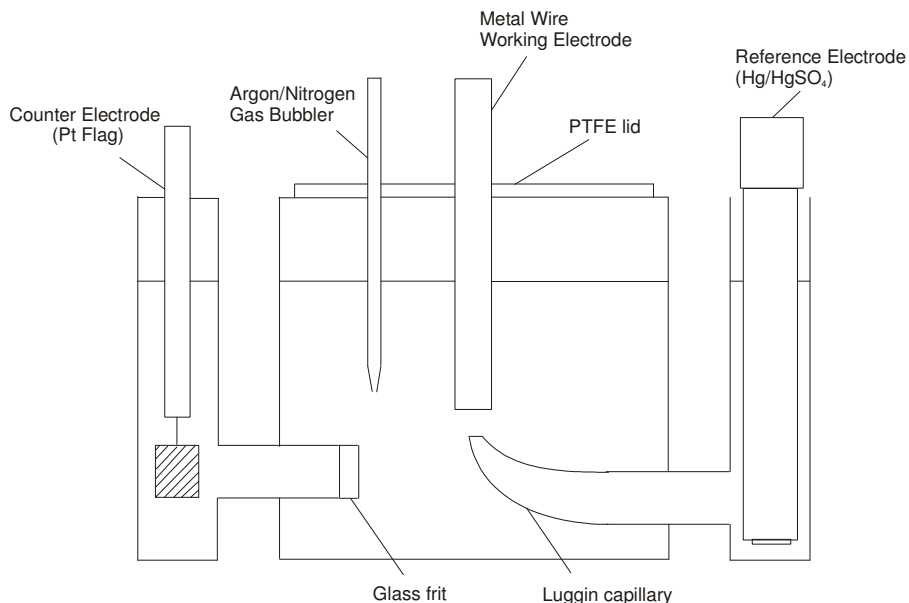
Figure 2.4: Schematic of a three-electrode liquid-electrolyte cell [10].

For a liquid electrolyte such as 0.5M H_2SO_4, both anionic and cationic species are typically present in the solution (e.g. H^+, SO_4^{2-}). On the other hand in a Nafion$^\circledR$ membrane, cations (e.g. H^+) are the majority of the mobile species. There is sulfonate present but it is immobile. Recent research found that the reaction mechanism at the

Nafion® interface can be quite different from the one in the liquid electrolyte because of the absence of mobile anions [11]. Therefore, a solid-state cell was introduced to provide a more viable measurement.

Figure 2.5 shows the cross sectional view of a solid-state cell. This set-up can determine active catalysts at the Nafion® interface rather than in a liquid electrolyte. Once promising catalysts are laid out, they can be further tested in a PEM reactor for long-term performance.
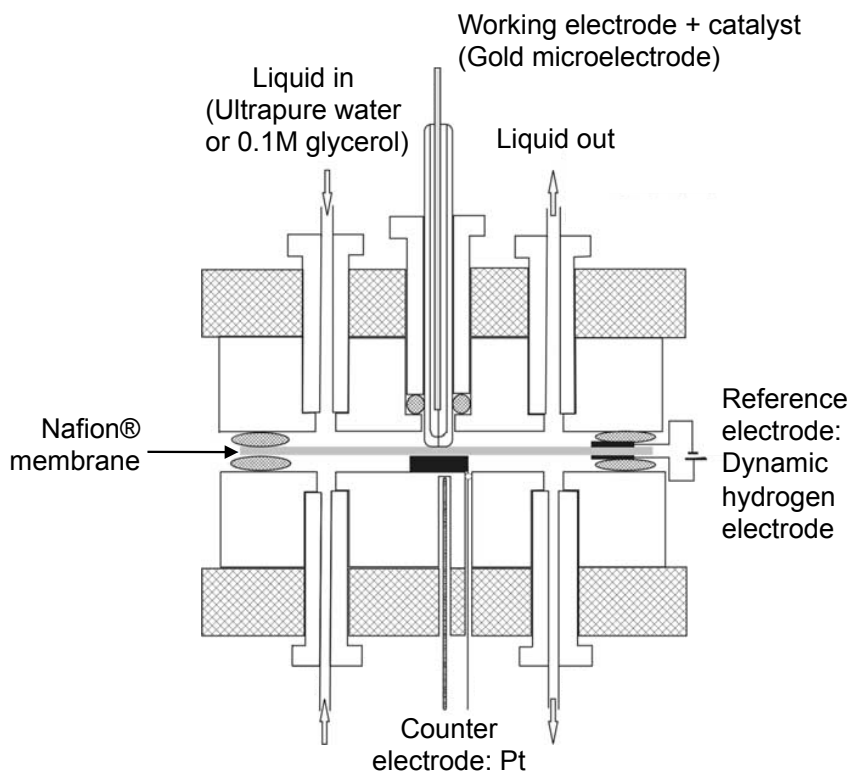
Figure 2.5: Schematic of a solid-state cell [11].

Similar to the measurement in a three-electrode cell, the solid-state cell is connected to a potentiostat (Autolab PGSTAT320N, Metrohm AG) via three electrodes: working electrode, reference, and counter. A gold microelectrode was used for the working electrode. The catalyst was physically rubbed onto the microelectrode surface prior to the experiments. A dynamic hydrogen electrode (DHE) was used for the reference electrode (0.04 V vs. RHE), which was connected to the Nafion® mem-

brane. Nafion® membranes were treated prior to each experiment to remove any adsorbed organics by boiling them in 3% H_2O_2 and 0.5 M H_2SO_4 using a procedure described elsewhere [12]. At the other side of the gold microelectrode via Nafion® membrane, Pt plate with Pt wire was used as the counter electrode. Ultrapure water or 0.1 M glycerol was supplied through the top channels for either hydrating the membrane or testing glycerol oxidation activity. The glasswares (e.g. beakers) used for this measurement were cleaned properly using 0.1 M $KMnO_4$ and 0.2 M H_2SO_4 and then rinsed with 0.2 M H_2O_2 and 0.35 M H_2SO_4 to remove any contaminants that may contribute to additional faradaic current.

CV was used as a measuring method to investigate the electrochemical stability and activity of the electrocatalyst. CV has become a very popular technique for initial electrochemical studies of new systems and has proven very useful for obtaining information about fairly complicated electrode reactions. In a CV measurement, potential is ramped linearly versus time then the ramp is reversed at a specific time, t = λ (or at the switching potential, E = E_λ) as shown in Figure 2.6 [13]. The slope of this potential sweep is called the scan rate (v), which can be varied depending on the speed of the reaction of interest. For example, to examine a slow reaction, a slower scan rate is selected.
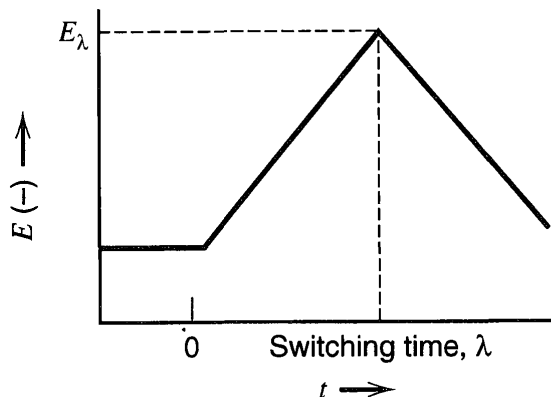
Figure 2.6: Cyclic potential sweep with time [13].

2.4 Evaluation in a proton-exchange-membrane reactor

A PEM reactor comprises different materials layered in a controlled manner. These materials include a membrane electrode assembly (MEA), a core part of the reactor where electrochemical reaction occurs. In addition, several other key pieces of equipment are required to conduct glycerol oxidation in a PEM reactor. Such examples include a humidifier, a liquid pump, and a power supply. This section gives a detailed description of what types of materials were used, how the MEAs were fabricated, and how the equipment was operated.

2.4.1 Fabrication of membrane electrode assemblies

MEAs were prepared by painting the catalyst ink onto the carbon cloth gas diffusion layers (GDLs, carbon cloth-graphitized spun yarn carbon fabrics obtained from Fuel Cell Store) with the desired weight loadings using a paintbrush. Catalyst ink was prepared from each catalyst previously mentioned mixed with ultrapure water, isopropanol, and Nafion® perfluorinated resin solution (5 wt%, Sigma-Aldrich) for both the anode and cathode. The perfluorinated resin solution functions as a binder to bond the Nafion® membrane to the GDLs. The target concentration for the perfluorinated resin solution in the catalyst ink was 20 wt.% with respect to the catalyst weight. Catalyst ink was painted onto a GDL using a paint brush, then dried in an oven at 110 °C for 1 hour to evaporate water and isopropanol. Catalyst loadings were controlled by measuring the weight increase per unit area (e.g. 1 mg/cm^2). Each GDL has an area of 6.45 cm^2. A Nafion® membrane (N117 obtained from Ion Power) was cut into 6 cm by 6 cm squares and then pretreated using the standard method described previously and stored inside the ultrapure water until use. The Nafion® membrane was placed between the anode and cathode GDLs, and this assembly was hot pressed together at 135 °C and 800 psi for 5 minutes. The resulting MEAs were used to measure electrocatalytic activities and selectivities in the electrochemical re-

actor. Some key components of MEAs are described as follows.

Nafion® membrane

Nafion® is the brand name for the DuPont membrane electrolyte, which is most frequently used for PEM fuel cells. The Nafion® membranes are made from a persulfonated polytetrafluoroethylene (PTFE)-based polymer that has very high chemical and thermal stability. It has a similar structure to Teflon®, but includes a sulfonic acid group ($SO_3^-H^+$) that provides sites for proton transport [14].
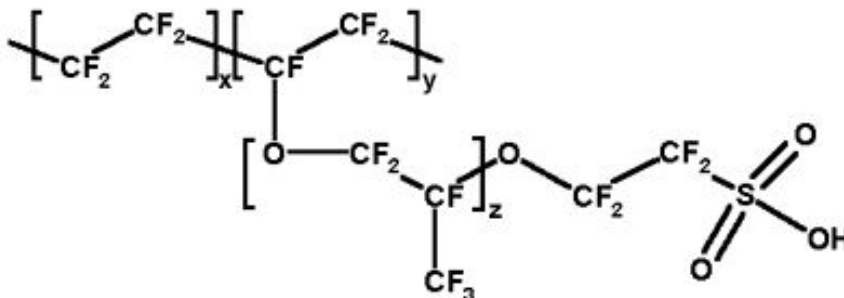
Figure 2.7: Chemical structure of Nafion® [14].

The transport of the protons occurs through hydronium complexes (H_3O^+) in the presence of water. The proton conductivity in the Nafion® membrane is highly dependent on the water content (λ) and the nanostructure of the membrane. Many studies have been done to correlate λ with conductivity and transport properties (e.g electroosmotic drag) [14].

The proton transport mechanism in Nafion® has been found to be divided into two regions based on the water environment of the Nafion®.

1. A surface diffusion mechanism at the pore wall where proton mobility is slow due to the strong electrostatic attraction of SO_3^- groups.

2. A bulk diffusion mechanism in the central region of the pore where proton mobility is fast. In bulk, proton diffusion occurs via the Grotthuss mechanism

(also know as the proton-hopping mechanism), or traditional mass diffusion of hydronium complexes [15].

The Nafion® membrane has to be fully hydrated to have sufficient ionic conductivity equivalent to the liquid electrolyte. In our reactor set-up, a humidification system was placed between the reactor and the cathode gas flow meter, supplying well humidified N_2 to the MEA.

Gas diffusion layer

The GDL is located between the painted catalyst layer and a graphite block. The graphite block was fabricated with flow channels for dispersing materials. The GDLs provide electrical contact between the electrode and the graphite block, and distribute reactants to the electrodes. The GDL also helps to manage water by allowing in an appropriate amount of water vapor to keep the membrane hydrated [14].

GDLs are made from porous and electrically conductive materials such as carbon. Two types of GDLs were considered: carbon cloth and carbon paper. Carbon cloth showed superior activity to a carbon paper, and it is much easier to handle due to its flexibility during fabrication. Therefore, carbon cloth was used for the evaluations in a PEM reactor.

2.4.2 PEM reactor description

The PEM reactor was assembled according to the method described in the literature [16] by placing the MEA between the Teflon® gaskets, the graphite current collectors, and the copper plates. Flow channels in the graphite current collectors are shown in Figure 2.9. Unlike in a typical PEM fuel cell, the channels on the liquid side (anode) are designed to be wider than those on the gas side (cathode) to ensure smooth flow of liquid reactants. Teflon® gaskets were used to provide good sealing between the MEA and the graphite blocks. The assembly was tightened to a torque

of 7.3 N·m to prevent leaking.
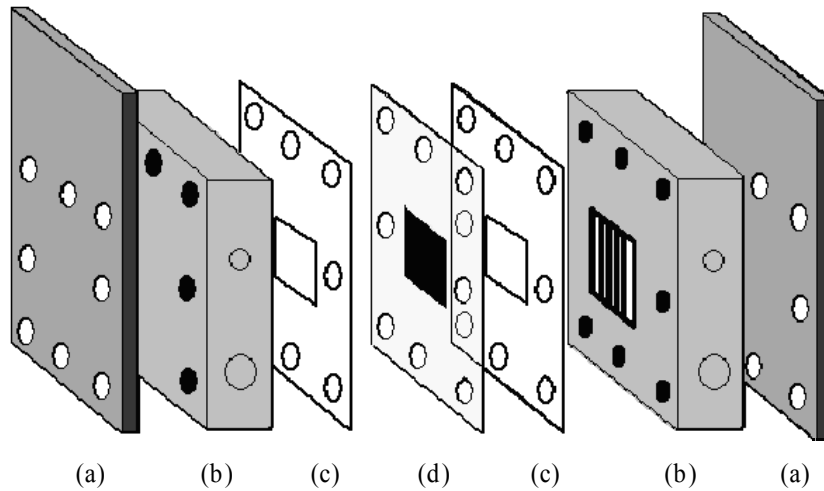
Figure 2.8: Exploded view of a PEM reactor: (a) copper plate, (b) graphite block with flow channel, (c) silicone gasket, (d) MEA [16].
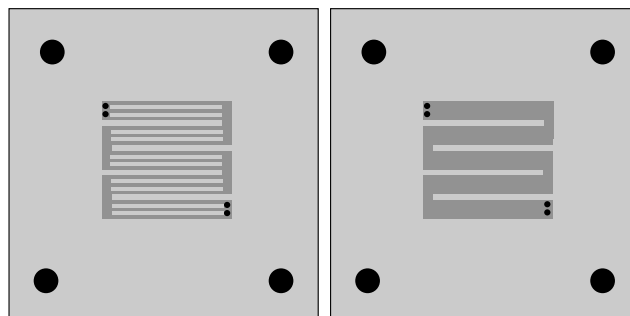
Figure 2.9: Schematic channel design of graphite current collectors (Left: Cathode, Right: Anode).

The SPE reactor system consisted of seven major components (Figure 2.10): a DC power supply (E3640A, Agilent), a heating mantle (100D EMS102 and Stir Control II, Glas-Col), a liquid pump (FMI Q Pump Model QG400 Q1CKC Q485, Fluid Metering), a mass flow controller (Mass-flo® controller, mks), the SPE reactor, a humidifier (Gas humidification system, Fuel Cell Technologies), and a computer-controlled Fuel Cell test system (890C Fuel Cell Test Loads, Scribner Associates).
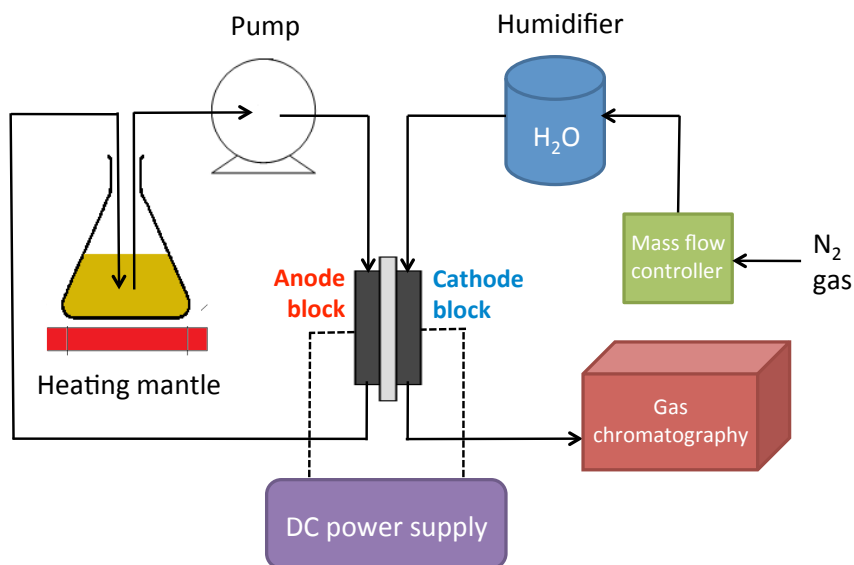
Figure 2.10: PEM reactor set-up.

The main functions of these components are as follows.

• DC power supply: Applies external potential to a PEM reactor to drive the oxidation reaction. Can be used for evaluating either at constant current or constant potential.

• Heating mantle: Holds a flask containing aqueous glycerol and keeps the solution at a set temperature. Connected with stir controller to keep the solution mixed throughout the reaction.

• Liquid pump: Pumps the glycerol solution with a constant flow rate. Flow rate can be adjusted by setting the dial indicator on the side to the pump, which was calibrated prior to the experiments.

• SPE reactor: Assembled from copper plates, graphite blocks, silicone gaskets, and MEA (Figure 2.8).

- Mass flow controller: Controls the flow rate going into a PEM reactor.

- Humidifier: Flow-controlled gas goes through the humidifier and is saturated with vapor before going into a PEM reactor. It keeps a Nafion membrane hydrated prior to and during the reaction.

- Fuel cell test system: PC-controlled Fuel Cell test system that can control temperature and gas flow rate of the system. FuelCell$^\circledR$ software (Scribner Associates, version 4.1) was used to control the temperature for the reactor and gas, and the flow rate of the gas. This software is also capable of monitoring potential deviation.

2.4.3 Operating conditions

Prior to the performance evaluation, the humidified N_2 gas (Cryogenic Gases, pre-purified) at 50 °C was supplied to a PEM reactor with a flow rate of 50mL/min for 24 hours. Then the oxidation process was carried out at 50 °C, at constant potential, and at constant N_2 and aqueous glycerol flow rates of 100 ml/min unless otherwise stated. Partial oxidation of glycerol is exothermic, but the reactor was heated at 50 °C to maintain a reasonable reaction rate in order to make up for the relatively low conversion at lower temperatures.

During the hydration and oxidation process, the PEM reactor was kept at 50 °C with a temperature controller system. Aqueous glycerol was continuously stirred and held at 50 °C using a heating mantle.

Table 2.2: Standard operating conditions of glycerol oxidation in an SPE reactor.

Flow rate	Anode: Aqueous glycerol 100 ml/min Cathode: N_2 100 ml/min
Glycerol concentration	2.7M
Temperature	50 °C (glycerol, N_2 gas, reactor)
N_2 Pressure	10 psi
Catalyst	Anode: 20% Pt/C, 20% Pt-10% Ru/C, Pt black (1 mg-Pt/cm^2) Cathode: 20% Pt/C (1 mg-Pt/cm^2)
Potential	0.4 - 1.5 V vs. RHE

2.5   Product analysis

A gas chromatograph (GC) was used to determine the composition of different species. During each experiment in a PEM reactor, the aqueous solution with a known glycerol concentration was circulated the whole time and product samples were taken at certain time points to evaluate the kinetic performance. The resulting liquid samples were analyzed using a GC equipped with a flame ionization detector (FID) and a mass spectrometer (MS) for liquid products. For detecting gas-phase products, a GC is directly connected to the outlet of the PEM reactor and analyzed with a thermal conductivity detector (TCD).

2.5.1   Analysis of liquid products

A GC-FID (GC-450, Varian) and a MS (MS-220, Varian) was used, equipped with a CP-WAX column (CP-7615, Varian), which is capable of separating small alcohols (e.g. ethylene glycol, glycerol) and their derivatives after adequate preparation. The column was chosen based on the products analyzed since column materials are not able to tolerate all compounds. The column was connected to each detector via a

4-way valve (manually switchable), which allowed us to use one detector at a time without reinstalling the column. Helium (Cryogenic Gases, pre-purified) was used as the carrier gas. The product samples were diluted with ethanol (99.5+%, ACS-grade, Acros Organics) to 1 vol.% of aqueous glycerol prior to the GC injection. Ethanol was chosen due to its high solubility in the products, which helped insure the homogeneous evaporation of the aqueous samples.

Star Chromatography Workstation (Varian) was used to assign each peak to each compound, based on retention times. MS Workstation (Varian) was used for determining unknown products from the mass spectrum database. The product composition can be estimated by integrating the area within the expected retention time. Each integration area was divided by the total integration area after including the response factor for each compound to calculate the product yields for further analysis.

2.5.2   Analysis of gas products

The reaction also produced gas products, which needed to be evaluated in real time. As shown in Figure 2.10, a GC-TCD (8610 GC, SRI Instruments) was directly connected to the gas effluent, which measured the gas concentration every 30 minutes. Argon (Cryogenic Gases, pre-purified) was used as a carrier gas. A SUPELCO 60/80 Carboxen-1000 column (#12390-U, Length: 15 ft, Width: 1/8 in., Inner diameter: 2.1 mm) was used for separating gases. Prior to the evaluations, calibration of possible gases (H_2, N_2, O_2, CO, CO_2) was carried out with certified-grade calibration gases obtained from Cryogenic Gases. Upon injection of gas samples, the oven temperature was held at 70 °C for 5 minutes, then ramped up to 220 °C with a heating rate of 20 °C/min and held for 12.5 min.

PeakSimple Chromatography Software (SRI Instruments) was used to assign each peak to each compound, based on retention times. The concentration of each gas was determined based on the calibration results obtained earlier. The average concentra-

tion is used for the comparison in later chapters.

2.6 Post-reaction characterization

2.6.1 Deactivation mechanism

Current is the direct measure of the reaction rate for the electrochemical system. It typically shows exponential decay over time for various reasons. One of the major reasons is the deactivation of catalysts. The data (rate vs. time) can be fitted to the deactivation model to determine the catalyst deactivation mechanism. This data fitting has been used by Voorhies et al. to determine the catalyst deactivation mechanism for some reactions [17, 18].

$$-\frac{da}{dt} = k_d a(t)^m \tag{2.4}$$

$$a(t) = \frac{I_t}{I_{t=0}} \tag{2.5}$$

$$a = 1 - k_d t \quad \text{Linear} \tag{2.6}$$

$$a = e^{-k_d t} \quad \text{Exponential} \tag{2.7}$$

$$a = \frac{1}{1 + k_d t} \quad \text{Hyperbolic} \tag{2.8}$$

$$a = A_0 t^{-k_d} \quad \text{Reciprocal power} \tag{2.9}$$

The R^2 value is typically used to elucidate the deactivation mechanisms occurring on catalyst surfaces. Typically each model has the corresponding deactivation mechanism as shown in Table 2.3.

Table 2.3: Deactivation models and the corresponding deactivation mechanisms [17].

Type	Mechanism	Details
Linear	Surface oxidation	Formation of metal oxide on catalyst surface
Exponential	Poisoning	Irreversible adsorption of poisoning species such as CO
Hyperbolic	Sintering	Pt particle sintering and carbon support corrosion
Reciprocal power	Carbon deposition	Site blocking by carbonaceous species

This data fitting gives us some insight regarding deactivation mechanisms, and is a useful tool when combined with other experimental techniques that are described in the following sections.

2.6.2 Thermogravimetric analysis

The amount of deposition on the post-reaction catalysts was examined using thermogravimetric analysis (TGA). TGA measures the weight change in a material as a function of temperature or time under a controlled atmosphere inside the furnace to investigate the material's thermal stability or composition. This method was previously used by Chen et al. to study types of carbon deposition on spent catalysts [19].

This analysis was done using a Q50 Thermogravimetric Analyzer (TA Instruments) with a constant gas flow rate (15 mL/min) of O_2 (Cryogenic Gases, extradry). After taring the empty platinum pan, the spent catalyst was scraped from the post reaction MEA and placed on the pan for analysis. The Q50 features a vertical

beam balance design (sample capacity: 1000 mg) that supports precise TGA (balance sensitivity: 0.1 μg) measurements. A purge gas system with a digital mass flow controller provides precise metering of purge gas to the sample and reference pans. There is an inlet tube that delivers reactive or inert gas to the sample in the furnace, and another tube that vents reacted or inert gas to the fume hood. The Q50 also includes Advantage$^{\text{TM}}$ software for automatic experimental control, including customizing temperature programs, and Universal Analysis 2000 software for comprehensive data analysis.

2.6.3 Electrochemical surface area measurement

Electrochemical surface area (ECSA) loss is typically linked to the loss of activity for long-term operation of fuel cell catalysts [20]. ECSA was measured in a PEM reactor directly connected to a potentiostat using the CV method with the following procedure.

The SPE reactor was assembled according to the standard procedure described earlier. As indicated in Figure 2.11, the hydration gas (N_2) was supplied to both the anode and cathode channels for 48 hours to purge the system.
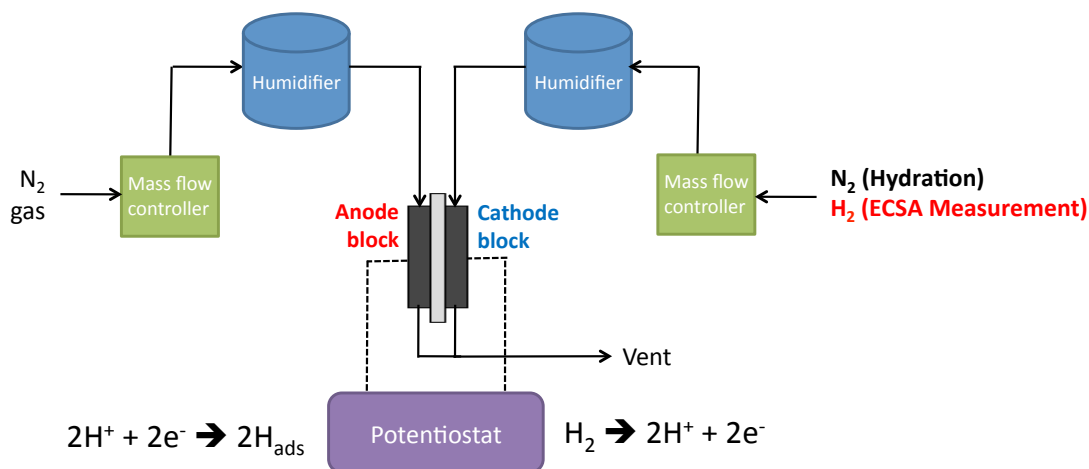
Figure 2.11: PEM reactor set-up for ECSA measurement.

After the hydration, the gas going into the cathode was switched to 200 mL/min of H_2. The N_2 gas flow to the anode was reduced to 20 mL/min, as the flow rate of N_2 at the working electrode can significantly influence the shape of the adsorption/desorption curve. With an increasing N_2 purge rate, H_2 is more readily swept from the electrode surface, decreasing the partial pressure of H_2 at the electrode [21]. CV measurement was then conducted to take the scans before exposing the MEAs to the reaction conditions.

After glycerol oxidation at constant potential, the PEM reactor was disassembled to clean all the components, including copper plates, graphite blocks, and silicone gaskets. The MEA was immersed in the clean ultrapure water and rinsed throughly. Then the reactor was reassembled to take CV scans for the spent MEA using the same gas setting with H_2 to the cathode (200 mL/min) and N_2 to the anode (20 mL/min).

For platinum, an experimental value of $Q_{H,ads}$ was estimated by calculating the total charge under the hydrogen adsorption/desorption curve (Q_{total}) and the charge due to the double layer (Q_{dl}):

$$Q_{H,ads} = \frac{Q_{H,ads} - Q_{dl}}{2} \tag{2.10}$$
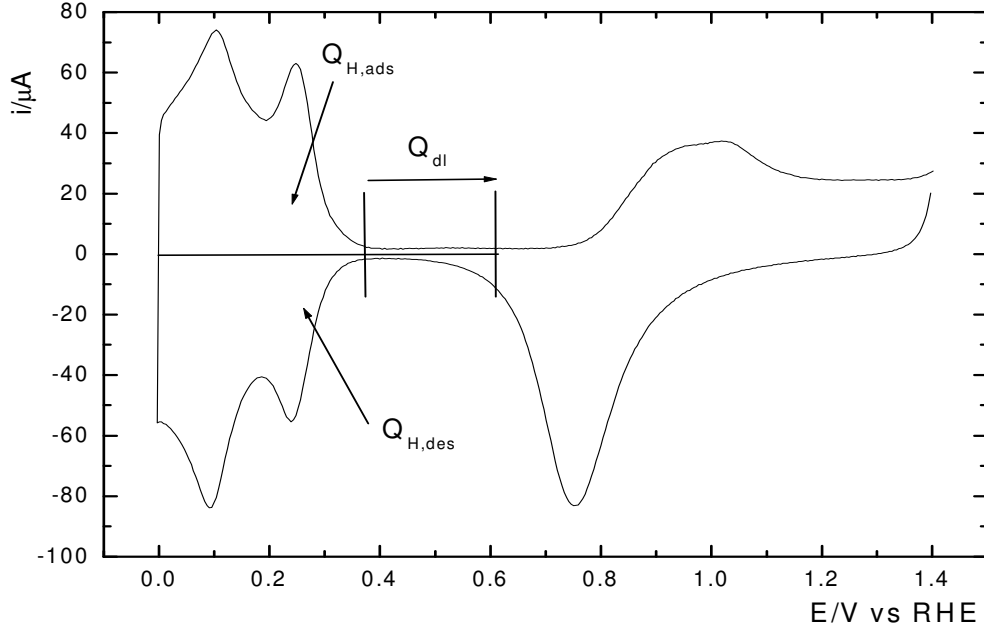
Figure 2.12: Cyclic voltammogram for Pt electrode in 0.5M H_2SO_4 at a scan rate of 10 mV/s and at room temperature [10].

The ECSA of Pt was then calculated using the following equation, assuming one hydrogen atom observed to one platinum atom [22].

$$\text{ECSA}_{\text{Pt}} = \frac{Q_{\text{H,ads}}}{210 \ \mu\text{C} \cdot \text{cm}_{\text{Pt}}^{-2} \cdot L_{\text{ca}} A_{\text{g}}} 10^5 \tag{2.11}$$

where L_{ca} is the cathode loading of the MEA [mg-Pt/cm^2] and A_{g} is the geometric area of the electrode [cm^2].

References

[1] V. daSilva, M. Schmal, S. Oyama, Niobium carbide synthesis from niobium oxide: Study of the synthesis conditions, kinetics, and solid-state transformation mechanism, J Solid State Chem 123 (1996) 168–182.

[2] S. T. Oyama, Preparation and catalytic properties of transition-metal carbides and nitrides, Catal Today 15 (1992) 179–200.

[3] R. Kapoor, S. Oyama, Synthesis of vanadium carbide by temperature programmed reaction, J Solid State Chem 120 (1995) 320–326.

[4] J. A. Schaidle, A. C. Lausche, L. T. Thompson, Effects of sulfur on mo2c and pt/mo2c catalysts: Water gas shift reaction, Journal of Catalysis 272 (2010) 235–245.

[5] W. Setthapun, S. Bej, L. Thompson, Carbide and nitride supported methanol steam reforming catalysts: Parallel synthesis and high throughput screening, Topics in Catalysis 49 (2008) 73–80.

[6] S. Brunauer, P. Emmett, E. Teller, Adsorption of gases in multimolecular layers, Journal of the American Chemical Society 60 (1938) 309–319.

[7] P. Emmett, S. Brunauer, The use of low temperature van der waals adsorption isotherms in determining the surface area of iron synthetic ammonia catalysts, Journal of the American Chemical Society 59 (1937) 1553–1564.

[8] P. Patnaik, Dean's analytical chemistry handbook 2nd ed., McGraw-Hill (2004).

[9] D. Harvey, Modern analytical chemistry, McGraw-Hill (2000).

[10] A. E. S. Sleightholme, Electrochemical studies of fuel cell catalysts, Dissertation, Imperial College London (2008) 1–232.

[11] J. Jiang, A. Kucernak, Investigations of fuel cell reactions at the composite microelectrode vertical bar solid polymer electrolyte interface. i. hydrogen oxidation at the nanostructured pt vertical bar nafion(r) membrane interface, J Electroanal Chem 567 (2004) 123–137.

[12] T. A. Zawodzinski, C. Derouin, S. Radzinski, R. J. Sherman, V. T. Smith, T. E. Springer, S. Gottesfeld, Water-uptake by and transport through nafion(r) 117 membranes, J Electrochem Soc 140 (1993) 1041–1047.

[13] A. J. Bard, L. R. Faulkner, Electrochemical methods - fundamentals and applications 2nd ed., John Wiley & Sons (2001).

[14] C. S. Spiegel, Designing & building fuel cells, McGraw-Hill (2007).

[15] P. Choi, N. Jalani, R. Datta, Thermodynamics and proton transport in nafion - ii. proton diffusion mechanisms and conductivity, J Electrochem Soc 152 (2005) E123–E130.

[16] P. Pintauro, M. Gil, K. Warner, G. List, W. Neff, Electrochemical hydrogenation of soybean oil with hydrogen gas, Ind Eng Chem Res 44 (2005) 6188–6195.

[17] A. Voorhies, Carbon formation in catalytic cracking, Industrial & Engineering Chemistry 37 (1945) 318–322.

[18] A. C. Lausche, J. A. Schaidle, L. T. Thompson, Understanding the effects of sulfur on mo2c and pt/mo2c catalysts: Methanol steam reforming, Applied Catalysis A: General 401 (2011) 29–36.

[19] X. Chen, A. R. Tadd, J. W. Schwank, Carbon deposited on ni/ce-zr-o isooctane autothermal reforming catalysts, Journal of Catalysis 251 (2007) 374–387.

[20] P. J. Ferreira, G. J. laO', Y. Shao-Horn, D. Morgan, R. Makharia, S. Kocha, H. A. Gasteiger, Instability of pt c electrocatalysts in proton exchange membrane fuel cells, J Electrochem Soc 152 (2005) A2256–A2271. Ti.

[21] R. Carter, S. Kocha, F. Wagner, M. Fay, H. Gasteiger, Artifacts in measuring electrode catalyst area of fuel cells through cyclic voltammetry, ECS Transactions 11 (2007) 403–410.

[22] H. A. Gasteiger, W. Gu, R. Makharia, M. F. Mathias, B. Sompalli, Beginning-of-life mea performance — efficiency loss contributions, Handbook of Fuel Cells – Fundamentals, Technology and Applications, John Wiley & Sons, Ltd. (2010) 1–18.

CHAPTER III

Electrocatalyst screening and characterization

3.1 Introduction

Various electrocatalysts have been evaluated for glycerol oxidation in a PEM fuel cell. Due to the operating conditions of a PEM fuel cell, there are several key requirements that electrocatalysts have to meet. First, they must be stable in contact with a Nafion® membrane, which is highly acidic when hydrated. Second, catalysts should be able to adsorb and desorb glycerol molecules easily. Third, it is advantageous to have poison-resistance to maintain activity over long-term operation. Finally, electrocatalysts should be able to target specific bonds (e.g. $C-C$ bond) to increase selectivity towards desired reactions (e.g. complete oxidation to CO_2).

In this chapter, the primary noble metal was first selected from several candidates based on the ability to react with glycerol. Then the primary noble metal and its alloy were supported on high-surface-area materials and characterized using N_2 physisorption, XRD, SEM-EDX, and ICP-OES. Electrochemical activity for glycerol oxidation was also evaluated, which is the primary result of interest. Transiton-metal-carbide-supported catalysts were synthesized and tested for stability because stability information for glycerol oxidation in PEM reactors is not readily available in the literature. Due to the simplicity of cell design and sample preparation possible with solid-state cells, a solid-state cell but no PEM reactor was used for these

electrochemical evaluations in order to save time.

3.2 Experimental

3.2.1 Synthesis of electrocatalysts

Noble metals (Pt black (Alfa Aesar), Ir black (Sigma-Aldrich), Rh black (Alfa Aesar)), and carbon-supported noble metals (20wt% Pt/C (Alfa Aesar), 20wt% Pt-10wt% Ru/C (Alfa Aesar)), were used as received. All carbide-supported Pt catalysts were synthesized from oxide precursors followed by wet impregnation of $H_2PtCl_6 \cdot 6\,H_2O$ using the standard procedure described in Section 2.2. Nb and W were chosen from among other transition metals (e.g. Mo) based on their stability in aqueous acid environments established by Pourbaix [1]. It has been observed that the stability of carbides in contact with Nafion® membranes is quite similar to that predicted by the Pourbaix diagram at pH 0.3 [2].

3.2.2 Physical characterization of electrocatalysts

The N_2 physisorption method was used to measure the physical surface area of electrocatalysts. Nitrogen gas was used with an ASAP 2010 Physisorption Analyzer (Micromeritics Instrument) to obtain the adsorption isotherms.

XRD analysis was used to determine the crystal structures of electrocatalysts. A Miniflex X-ray diffractometer (Rigaku) was used with Cu $K\alpha$ radiation (λ=1.5418 $\mathring{A}$), and a Ni filter. JADE Software (Materials Data, Inc.), which is capable of matching diffraction patterns in the ICDD-PDF database, was employed together with XRD analysis.

An ICP-OES was used to quantify the weight percent of the loaded metal on the carbide support. A 710-ES ICP-OES (Varian) was controlled with ICP Expert II software for auto sampling and data acquisition. Since W_2C cannot be completely

dissolved into aqua regia (HCl : HNO_3 = 3 : 1 by volume), the leftover metal loading solution from the incipient wetness impregnation was used to prepare analyzing solutions for the ICP-OES to calculate the concentration.

3.2.3 Electrochemical stability and activity measurement using a solid-state cell

Electrochemical stability and activity measurements were performed in a solid-state cell (Figure 3.1).
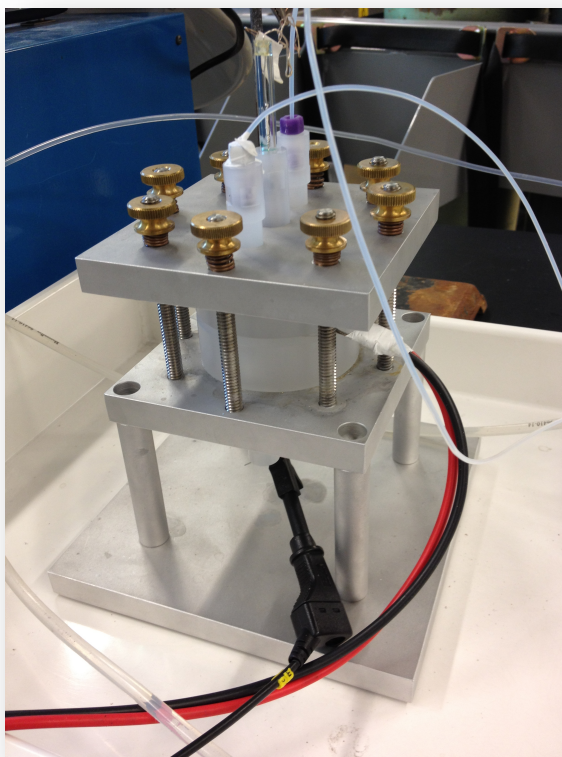
Figure 3.1: Image of a solid-state cell.
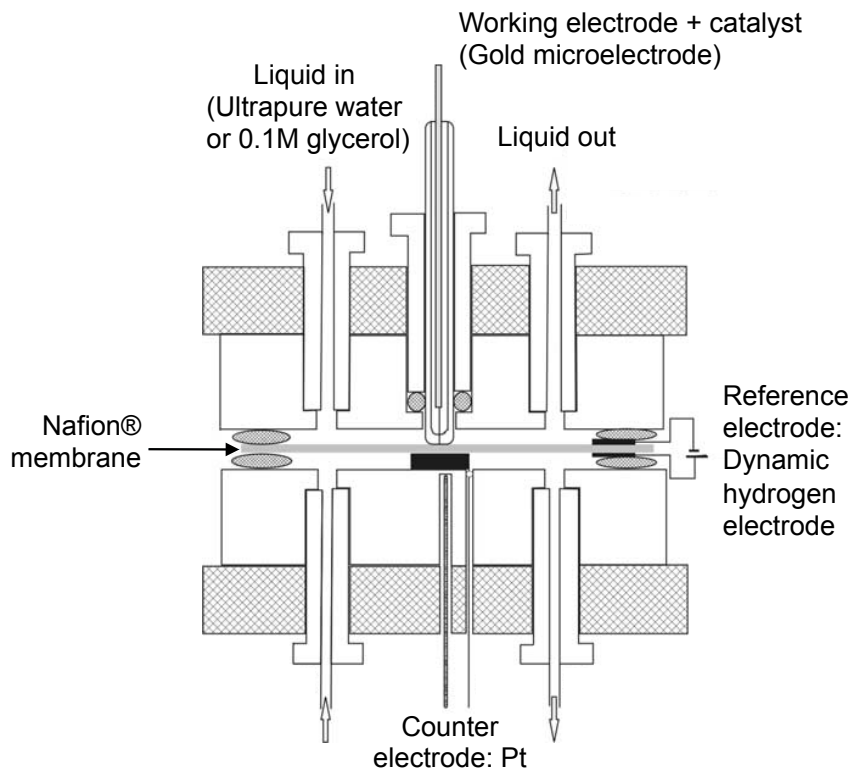
Figure 3.2: Schematic of a solid-state cell [3].

CV was implemented with an Autolab PGSTAT302N potentiostat (Metrohm AG) controlled by GPES software (Metrohm AG). A pretreated Nafion® membrane was installed and hydrated with ultrapure water for 1 hour using the liquid pump prior to the experiments. After taking blank CV scans with a gold microelectrode, a catalyst was physically rubbed on to the gold microelectrode surface to ensure good adhesion. A platinum flag with a platinum wire was used as the counter electrode. A DHE was used as the reference electrode. For stability measurement, ultrapure water was supplied from the top channels throughout the experiments. For activity measurements, either ultrapure water or 0.1 M glycerol was supplied. The flow rates for water and glycerol were 10 mL/min.

3.3 Results and discussion

3.3.1 Screening of active metal

Activity toward glycerol oxidation was evaluated for three noble metal catalysts (Pt, It, and Rh) using the solid-state cell. All these catalysts are unsupported and used as black. These three materials were chosen because they are stable in acid [1] and used as catalysts for oxidation of alcohols [4].

Figure 3.3 to 3.5 compare the CV scans for Pt, Ir and Rh in the solid-state cell and the CV scans for these catalysts in an acidic liquid electrolyte reported in the literature [5, 6]. Because of the main difference of electrolyte being solid or liquid states, some peak shapes are different, but we can find some common features in redox couples, which confirms that the Nafion® membrane was fully hydrated and the experiment with the solid-state cell was working properly.

In these CV scans, a peak is an indication of surface interaction or reaction between some species and an electrode (catalyst). For example, for Pt, oxygen is adsorbed at 1.0 V vs. RHE in the forward scan (O_{ad}), desorbed at 0.8 V vs. RHE in the reverse scan (O_{des}), and hydrogen gets adsorbed below 0.3 V vs. RHE (H_{ad}), and then desorbed in the forward scan (H_{des}). These peaks related to hydrogen and oxygen adsorption/desorption were also observed for Ir and Rh. If these peak locations for the forward and reverse scans are close to each other, the process is referred to as reversible. When these peaks are located at almost exactly same potential, typically the process is adsorption and desorption.
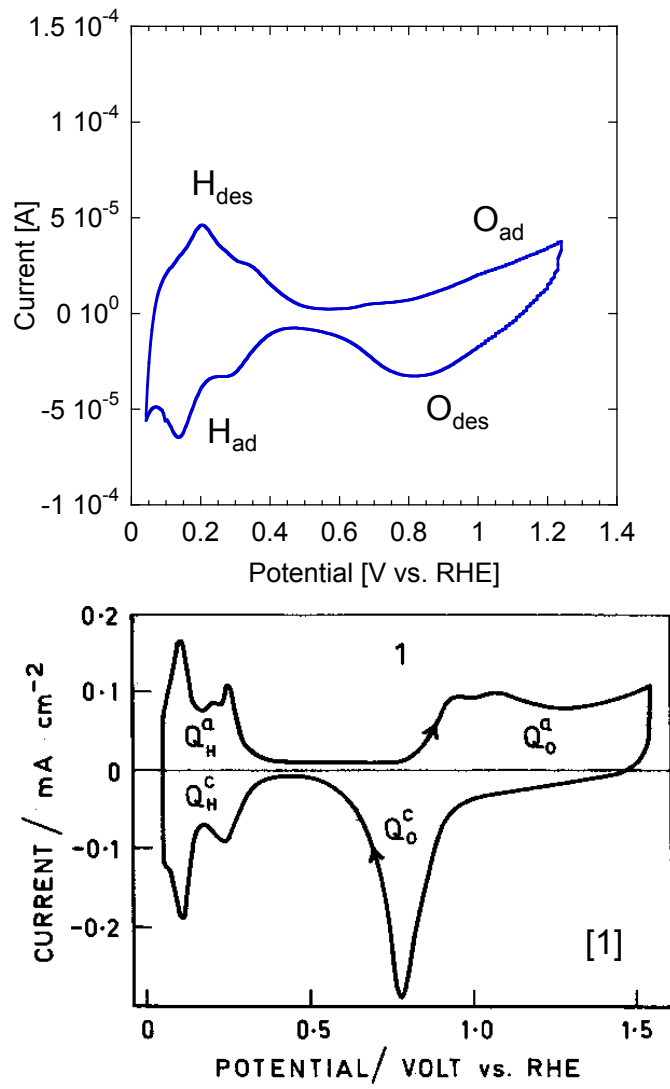
Figure 3.3: Cyclic voltammogram for Pt black in a solid-state cell and in an acidic electrolyte [5].
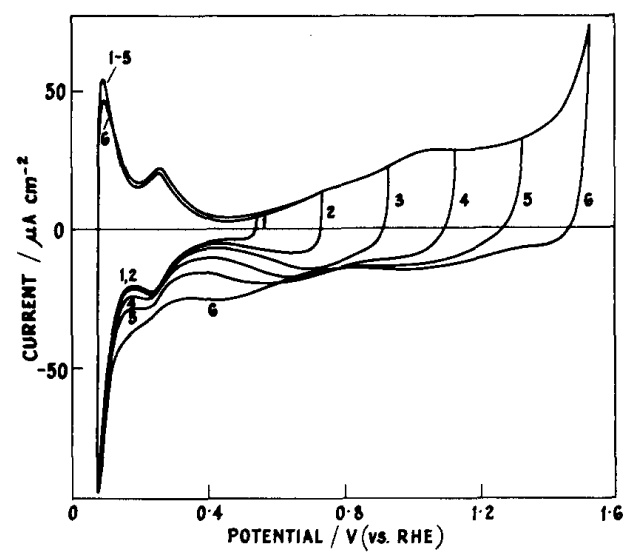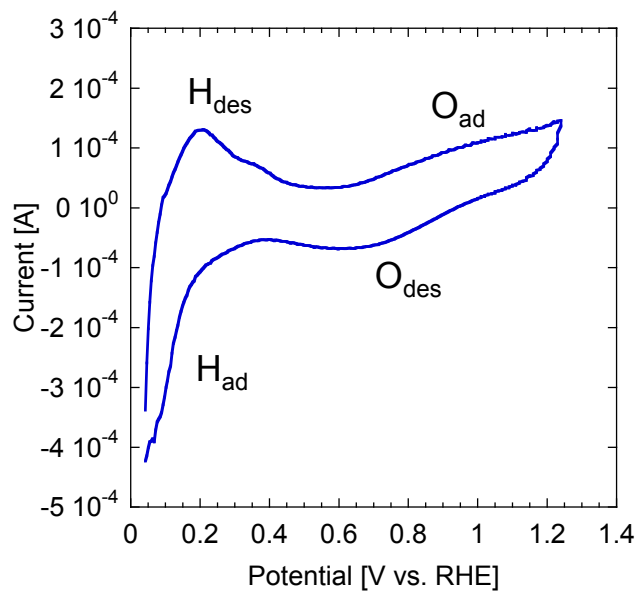
Figure 3.4: Cyclic voltammogram for Ir black in a solid-state cell and in an acidic electrolyte [6].
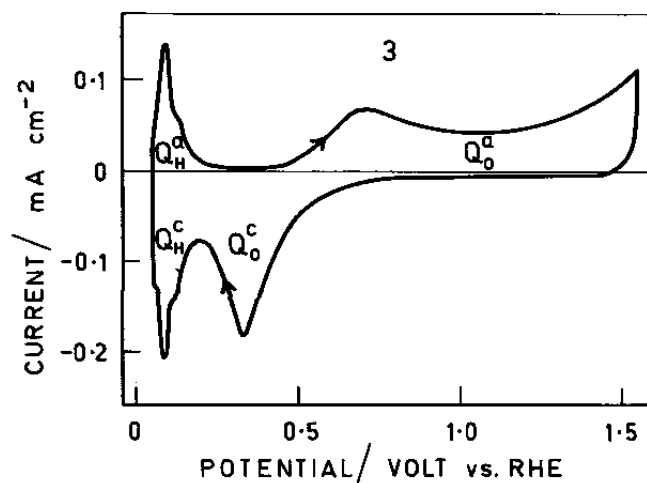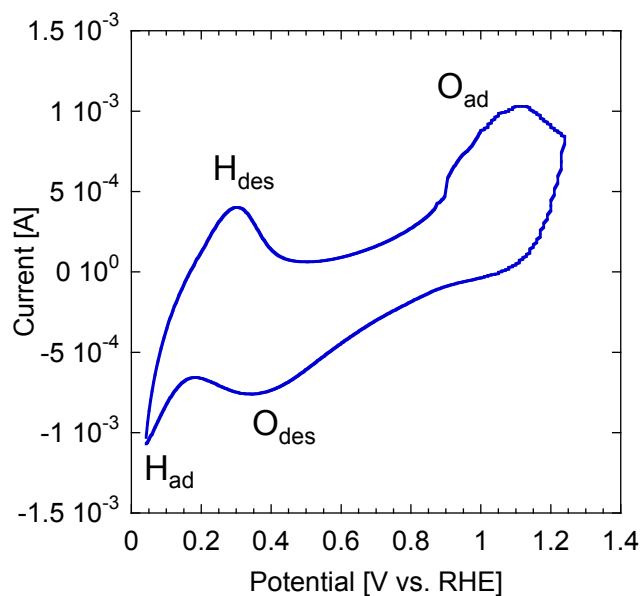
Figure 3.5: Cyclic voltammogram for Rh black in a solid-state cell and in an acidic electrolyte [5].

Figure 3.6 shows the CV scans for Pt with ultrapure water (in blue) and 0.1 M glycerol (in red). The glycerol concentration of 0.1 M was chosen to be able to compare our results with those reported in the literature. Any change in redox peaks is related to addition of glycerol. Pt showed two distinctive oxidation peaks at 0.8 V vs. RHE in the forward scan and 0.6 V vs. RHE in the reverse scan, which were not seen for the cyclic voltammograms in ultrapure water. It also exhibited suppression

of the hydrogen adsorption and desorption areas located between 0 V and 0.4 V vs. RHE.
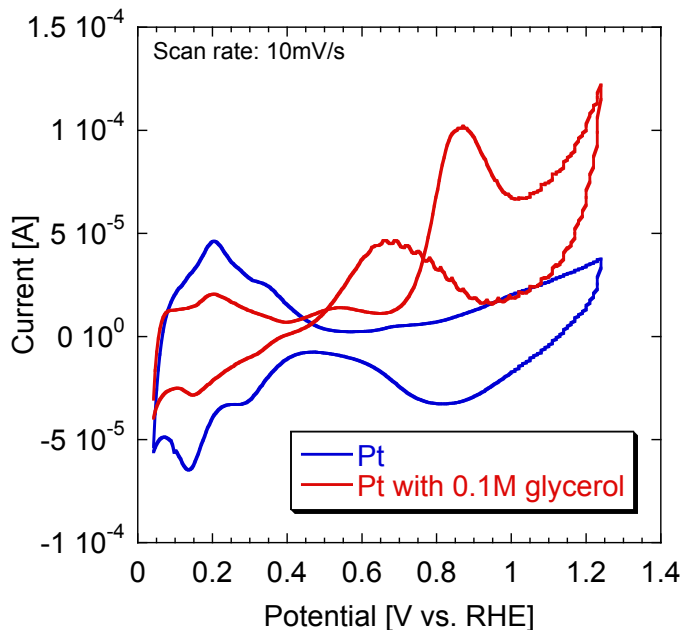
Figure 3.6: Cyclic voltammogram for Pt black with ultrapure water or 0.1 M glycerol.

These oxidation current peaks have been observed frequently in the literature for small alcohol oxidations. The peak locations reported for the forward and reverse scans were consistent with our results, indicating Pt was active for oxidizing glycerol at an interface with Nafion®. For all these results shown in Figure 3.6 to 3.8, there is oxidation of glycerol in the forward scan at around 0.8 V vs. RHE, but in the reverse scan, there is a secondary oxidation peak instead of a reduction peak. This secondary oxidation peak is associated with oxidation of incompletely oxidized carbonaceous residues as a result of oxidation of glycerol in the forward scan [7–9]. Gomes and co-workers performed an in-situ FTIR experiment in a three-electrode spectro-electrochemical cell to characterize these intermediates, and confirmed the formation of carboxylic acids, ketones and aldehydes [7]. The suppression of H_2 adsorption and desorption suggested that certain sites were occupied by strongly-adsorbed interme-

diates, reducing the number of sites available for H_2.
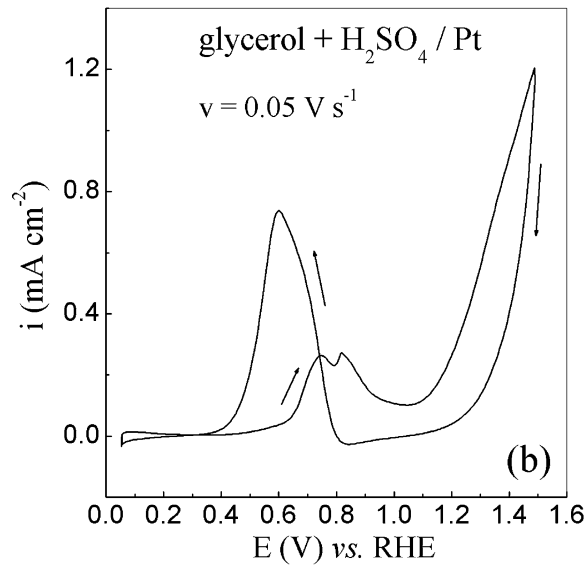
Figure 3.7: Cyclic voltammogram of a polished polycrystalline Pt electrode in 0.1 M glycerol + 0.1 M H_2SO_4, scan rate: 50 mV/s. [7]
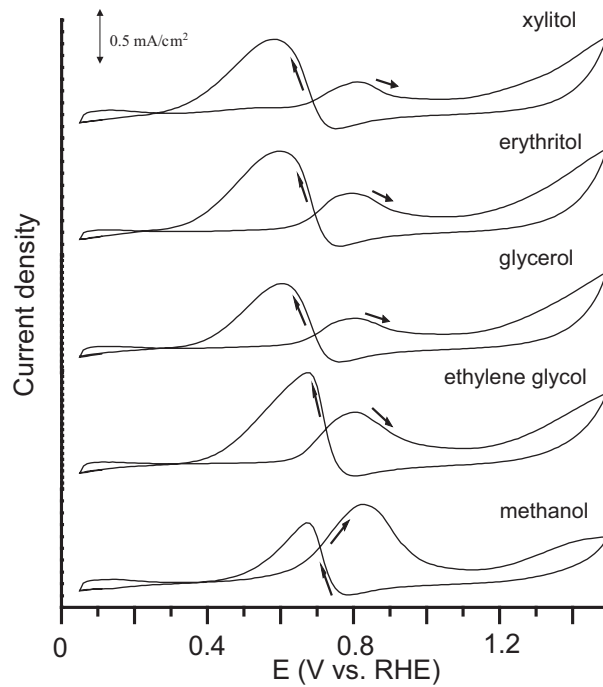
Figure 3.8: Cyclic voltammograms of a Pt electrode in 0.1 M alcohols + 1 M H_2SO_4, scan rate: 100 mV/s, temperature: 20°C. [8]

Regarding Figure 3.8, it is also worth discussing that there seem to be some similarities in the reaction mechanisms among these small alcohols, including rate-determining steps or other key steps such as adsorption or surface reaction. Figure 3.9 shows the mechanism of methanol oxidation on Pt, which is the most well-studied among alcohols. Methanol is first adsorbed on a Pt surface, and hydrogens dissociate from the C$-$H bond, followed by oxidation with surface hydroxyls to CO_2.
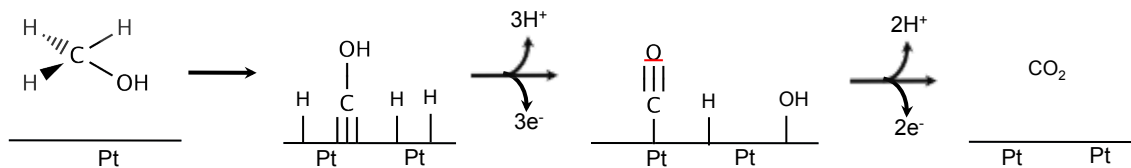
Figure 3.9: A reaction scheme describing the probable methanol electrooxidation process within a direct methanol fuel cell (DMFC) anode. [10]

Figures 3.10 and 3.11 show the CV scans for Ir and Rh with ultrapure water and 0.1 M glycerol respectively. There were slight variations for the measured current in certain potential regions but they mostly maintained a similar shape, with some enhancement in oxidation peaks. For Ir, there seem to be redox peaks at 0.8 V and 1.0 V vs. RHE, possibly due to adsorption of oxygen on the Ir surface or slow oxidation of glycerol. Rh also showed possible adsorption of oxygen on the Rh surface at 0.8 V vs. RHE. However, it is clear that neither Ir nor Rh have distinctive peaks for glycerol oxidation, indicating either that glycerol was not adsorbed, or the reaction was too slow to be detected with this scan rate (10 mV/s) on these catalysts. Even if the glycerol oxidation peak was confirmed using a slower scan rate such as 100 μV/s, the slow kinetics of Ir and Rh would not be suitable to obtain meaningful information about the reaction.
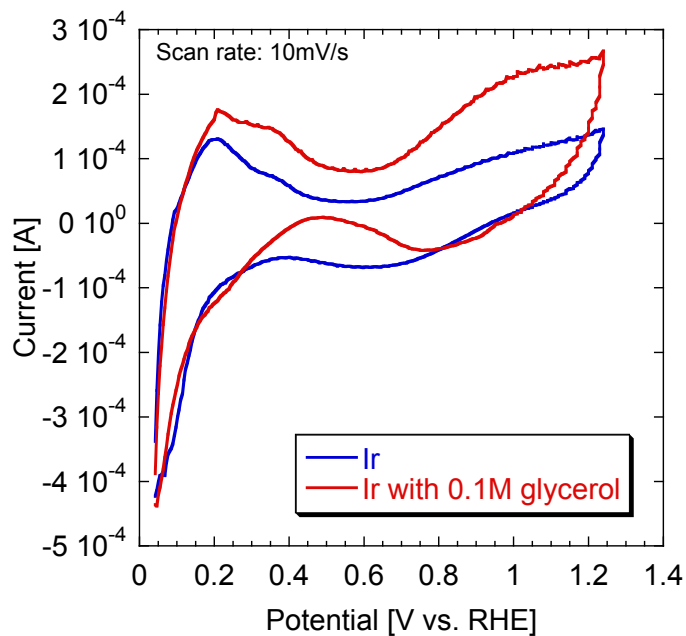
Figure 3.10: Cyclic voltammogram for Ir black with ultrapure water or 0.1 M glycerol.
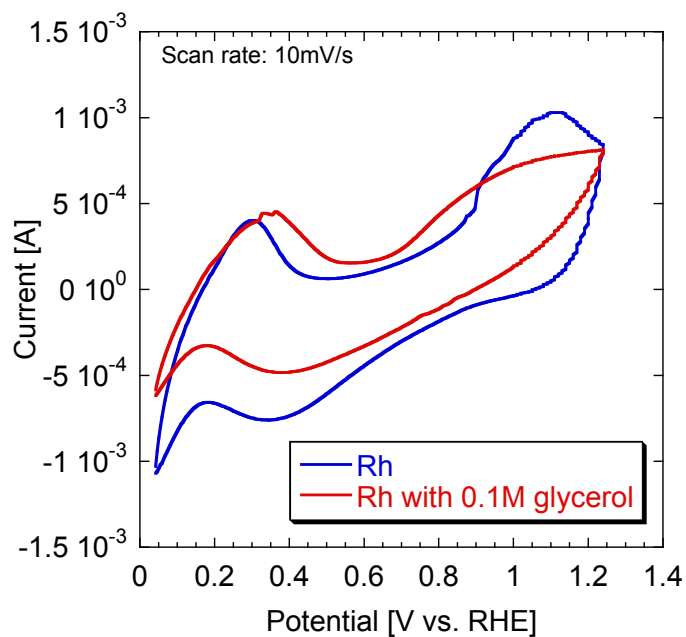
Figure 3.11: Cyclic voltammogram for Rh black with ultrapure water or 0.1 M glycerol.

Therefore, Pt was chosen as a primary metal. In addition to Pt black, we will

58

investigate Pt supported on carbon or transition-metal carbide because it is not eco-nomical when Pt is used as black, and because it is possible to expect some synergetic effect between Pt and those supports with respect to activity and selectivity, which can lead us to a reduction of Pt usage [11, 12].

3.3.2 Physical characterization of electrocatalysts

Four Pt-based catalysts were characterized before evaluation in the solid-state cell. The purpose of physical characterization was to validate the completeness of material synthesis with respect to targeted surface areas, targeted Pt loadings, crystal structure, and degree of carbonization from metal oxide precursors.

Physical surface areas and actual Pt loadings, if applicable, are listed for the evaluated electrocatalysts in Table 3.1. Surface area for the 5wt% Pt/NbC and 5wt% Pt/W_2C were an order of magnitude lower than those for the 20wt% Pt/C or 20wt% Pt-10wt% Ru/C. Both 5wt% Pt/NbC and 5wt% Pt/W_2C catalysts have closely met the nominal Pt loading based on the ICP-OES elemental analysis. Platinum loadings for the 5wt% Pt/NbC catalysts were equivalent to approximately four monolayers, and 5wt% Pt/W_2C to two monolayers, assuming a site density of 10^{19} sites/m^2. For convenience, all four catalysts will be denoted without weight percent (e.g. Pt-Ru/C for 20wt% Pt-10wt% Ru/C) for the rest of this dissertation.

Table 3.1: BET surface areas and metal loadings determined by ICP.

Material	Nominal Pt loading [wt%]	Actual Pt loading[1] [wt%]	Surface area[2] [m^2/g]
20% Pt/C	20	19.0 ± 1.7	190
20wt% Pt-10% Ru/C	20	-	140
5wt% Pt/NbC	5	4.4 ± 0.1	3.8
5wt% Pt/W_2C	5	5.0 ± 0.1	6.9

The diffraction patterns for the Pt/NbC and Pt/W$_2$C catalysts are shown in Figure 3.12, together with peak positions for polycrystalline reference materials. The results indicate that both Pt/NbC and Pt/W$_2$C were successfully carburized from oxide precursors as there were no peaks associated with their oxides. There were also no sharp Pt peaks in the diffraction patterns, suggesting that the Pt was finely dispersed on the carbide supports.
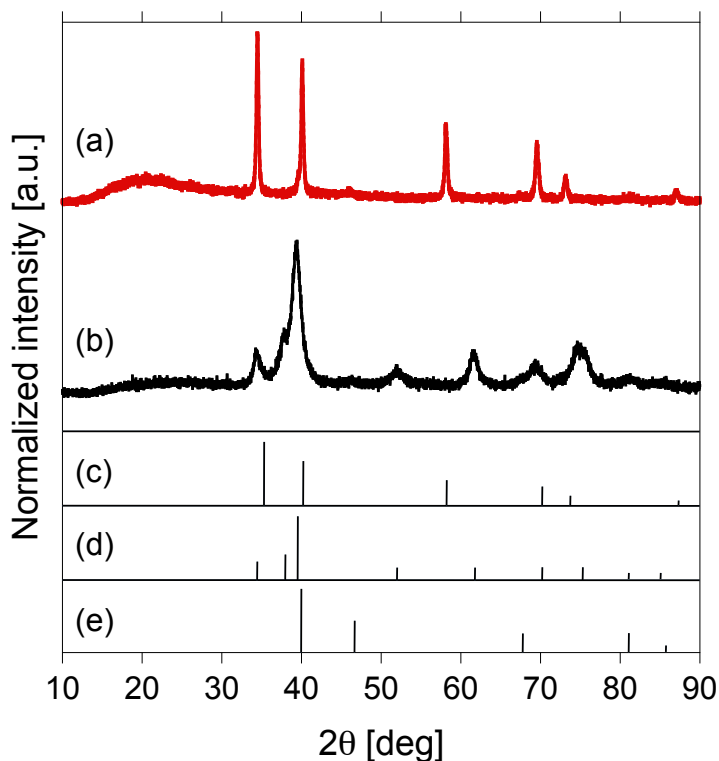
Figure 3.12: X-ray diffraction patterns for the (a) Pt/NbC and (b) Pt/W$_2$C, and peak positions for polycrystalline (c) NbC [13], (d) W$_2$C [14], and (e) Pt [15] reference materials.

3.3.3 Electrochemical stability of transition-metal-carbide-supported Pt at a Nafion® interface

The electrochemical stability window for synthesized Pt/NbC and Pt/W$_2$C was determined using a solid-state cell. First, a window expansion experiment was con-

ducted to experimentally determine the onset potential of material oxidation. After the window was chosen, the catalysts were cycled for up to 100 scans with a scan rate of 200 mV/s.

Figure 3.13 compares scan #10, #50, and #100 for (a) Pt/NbC and (b) Pt/W$_2$C. Pt/NbC seems stable up to 0.5 V vs. RHE, as there was no change in the voltammograms throughout the scans, but instability began to be seen above 0.6 V vs. RHE. However, Figure 3.6 showed that glycerol oxidation should preferably be operated at more than 0.8 V vs. RHE in order to have a reasonable rate. Therefore, Pt/NbC may not be suitable for this particular reaction.

It was reported previously that W$_2$C is only stable up to 0.4 V v.s. NHE (normal hydrogen electrode) in an acidic environment [16]. The same conclusion applies to Pt/W$_2$C, that this catalyst cannot be a choice for glycerol oxidation since it is unstable at more than 0.8 V vs. RHE where glycerol oxidation occurs on Pt. For Pt/W$_2$C, an increase in both oxidation and reduction current was observed around the hydrogen adsorption/desorption region (0$-$0.4 V vs. RHE), which could attribute to redox reaction of W$_x$O$_y$ species [16]. Weigert et al. reported a superior electrochemical stability for Pt/WC (tungsten monocarbide) in acid, which was improved to 1.0 V vs. NHE [17]. In this sense, Pt/WC could be considered as a future candidate for the electrocatalyst used for glycerol oxidation.
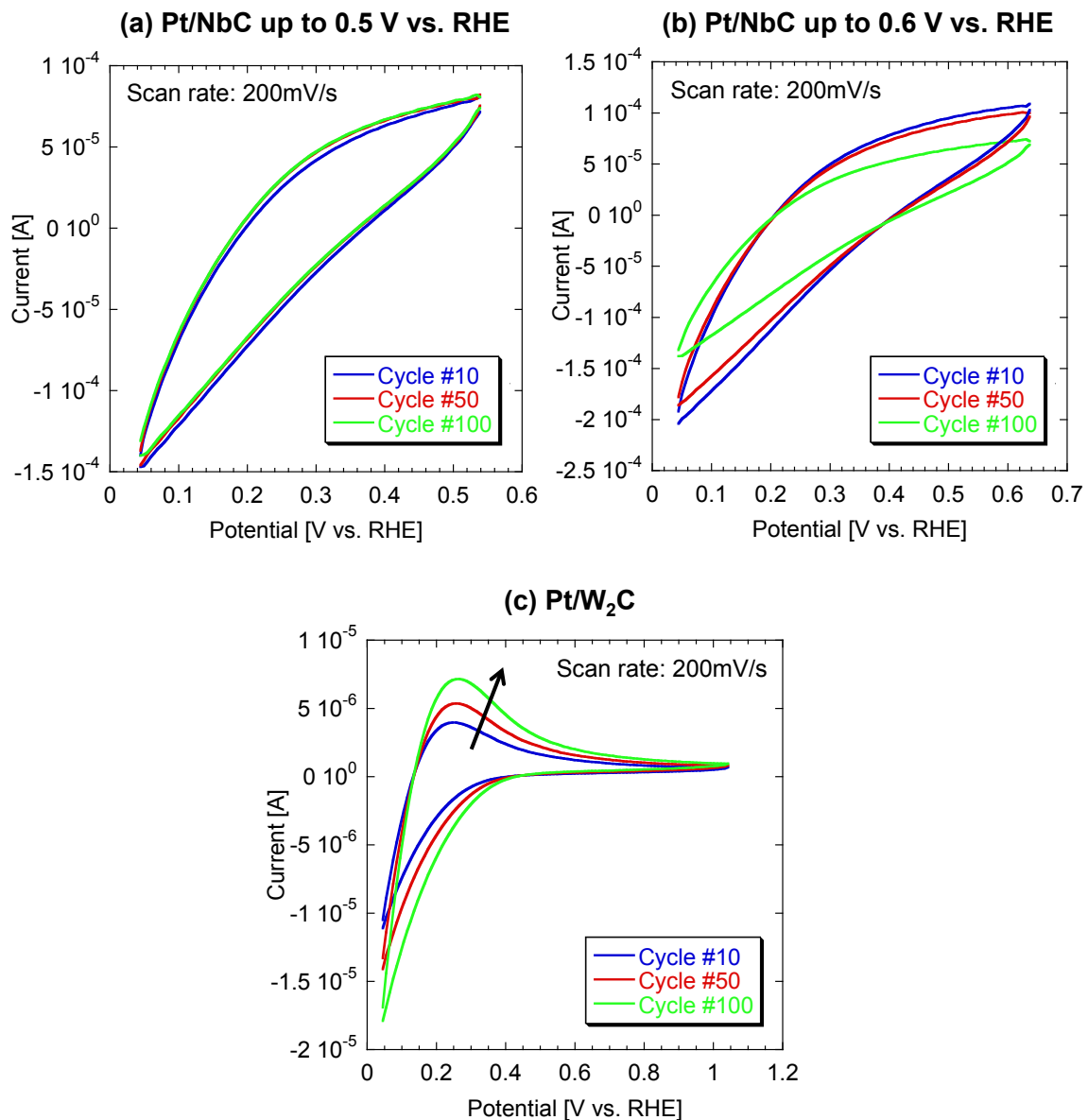
Figure 3.13: Cyclic voltammogram for (a) Pt/NbC cycled up to 0.5 V vs. RHE, (b) Pt/NbC cycled up to 0.6 V vs. RHE, and (c) Pt/W$_2$C at a Nafion$^{®}$ interface.

3.3.4 Activity of supported catalysts at a Nafion® interface

Based on catalyst screening and stability assessment of transition-metal-carbide supported catalysts, two other Pt-based catalysts were evaluated for glycerol oxidation in a solid-state cell. The first catalyst, Pt/C, is a benchmark catalyst widely used for PEM fuel cells. The second is the Pt-Ru alloy supported on carbon, which has shown to be poison resistant to CO [18], and very active for methanol electrooxidation [19].

Figure 3.14 shows the CV scans for Pt/C with ultrapure water and 0.1 M glycerol. The CV scans are similar to that for Pt black (Figure 3.6). Evidently, the Pt/C catalyst was active for glycerol oxidation, as two oxidation current peaks were confirmed in the forward and the reverse scans.
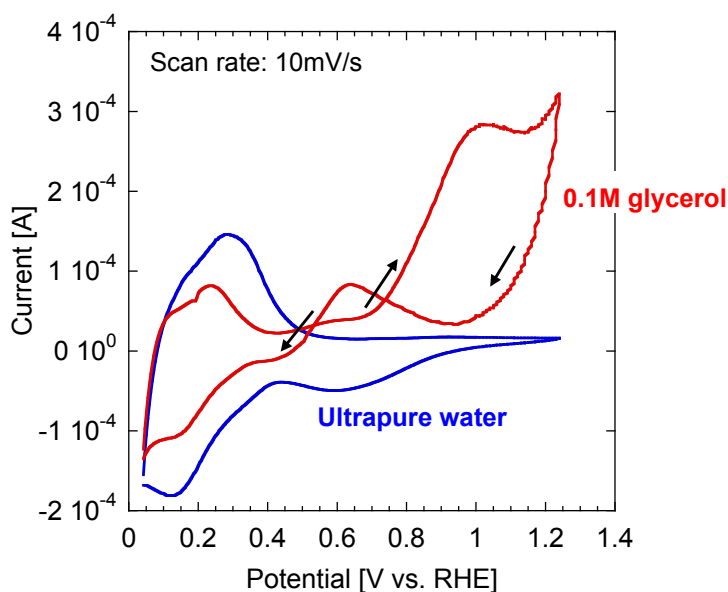
Figure 3.14: Cyclic voltammogram for 20wt%Pt/C with ultrapure water or 0.1 M glycerol.

Similar to Pt black, there was a secondary oxidation peak instead of a reduction peak in the reverse scan. The oxidized intermediates were strongly bonded on the catalyst surface for further oxidation rather than being desorbed or reduced, sug-

gesting the reduction or desorption of those intermediates are thermodynamically unfavorable on Pt as compared to the secondary oxidation.

Figure 3.15 shows the CV scans for Pt-Ru/C with ultrapure water and 0.1 M glycerol. Though anodic currents were observed at around 0.8 V vs. RHE in the forward scan, the peak shape and onset potential were quite different from those for Pt black (Figure 3.6) or Pt/C (Figure 3.14). The peak onset was located much lower, at 0.4 V vs. RHE for the forward scan, which made the peak shape much broader. Unlike Pt black or Pt/C, there was no oxidation peak observed in the reverse scan, suggesting the oxidized species in the forward scan were either reduced or desorbed in the reverse scan. The oxidation of glycerol and desorption of products on Pt-Ru/C proceed in a reversible process as opposed to the irreversible one for that on Pt black or Pt/C. These results indicate that the reaction on the Pt and Pt-Ru surface involves different intermediates and follows different reaction mechanisms, which will be explored further in the next section.
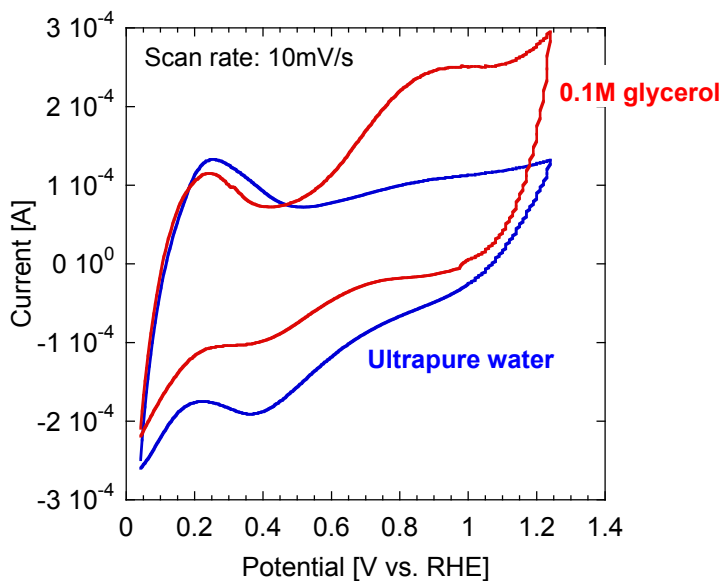
Figure 3.15: Cyclic voltammogram for 20wt%Pt-10wt%Ru/C with ultrapure water or 0.1 M glycerol.

3.4   Conclusions

The result showed that transition-metal-carbide-supported Pt catalysts were successfully synthesized by meeting the targeted physical properties. Based on the catalyst screening, Pt was chosen as a primary metal to investigate further by supporting and alloying it with other metals. Although transition-metal-carbide-supported Pt catalysts showed some stability in a solid-state cell, their stability window was much smaller, and thus their activity may be quite small to negligible for glycerol oxidation. Therefore, Pt/C and Pt-Ru/C were chosen to further investigate in a PEM reactor in the following chapters in terms of activity, selectivity, reaction mechanism and catalyst deactivation.

References

[1] M. Pourbaix, Atlas of electrochemical equilibria in aqueous solutions, 2d english ed., National Association of Corrosion Engineers (1974).

[2] A. C. Lausche, Nanostructured electrocatalysts for selective triglyceride hydrogenation, Dissertation, University of Michigan (2011) 1–119.

[3] J. Jiang, A. Kucernak, Investigations of fuel cell reactions at the composite microelectrode vertical bar solid polymer electrolyte interface. i. hydrogen oxidation at the nanostructured pt vertical bar nafion(r) membrane interface, J Electroanal Chem 567 (2004) 123–137.

[4] C. Lamy, A. Lima, V. LeRhun, F. Delime, C. Coutanceau, J. Léger, Recent advances in the development of direct alcohol fuel cells (dafc), J Power Sources 105 (2002) 283–296.

[5] D. A. J. Rand, R. Woods, A study of the dissolution of platinum, palladium, rhodium and gold electrodes in 1 m sulphuric acid by cyclic voltammetry, J Electroanal Chem 35 (1972) 209–218.

[6] D. Rand, R. Woods, Cyclic voltammetric studies on iridium electrodes in sulphuric acid solutions: Nature of oxygen layer and metal dissolution, Journal of Electroanalytical Chemistry and Interfacial Electrochemistry 55 (1974) 375–381.

[7] J. F. Gomes, G. Tremiliosi-Filho, Spectroscopic studies of the glycerol electrooxidation on polycrystalline au and pt surfaces in acidic and alkaline media, Electrocatalysis 2 (2011) 96–105.

[8] K. Matsuoka, M. Inaba, Y. Iriyama, T. Abe, Z. Ogumi, M. Matsuoka, Anodic oxidation of polyhydric alcohols on a pt electrode in alkaline solution, Fuel Cells 2 (2002) 35–39.

[9] J. H. Kim, S. M. Choi, S. H. Nam, M. H. Seo, S. H. Choi, W. B. Kim, Influence of sn content on ptsn/c catalysts for electrooxidation of c1-c3 alcohols: Synthesis, characterization, and electrocatalytic activity, Appl Catal B-Environ 82 (2008) 89–102.

[10] M. P. Hogarth, T. R. Ralph, Catalysis for low temperature fuel cells part iii: Challenges for the direct methanol fuel cell, Platin Met Rev 46 (2002) 146–164.

[11] E. Weigert, A. Stottlemyer, M. Zellner, J. Chen, Tungsten monocarbide as potential replacement of platinum for methanol electrooxidation, The Journal of Physical Chemistry C 111 (2007) 14617–14620.

[12] Y. Hara, N. Minami, H. Matsumoto, H. Itagaki, New synthesis of tungsten carbide particles and the synergistic effect with pt metal as a hydrogen oxidation catalyst for fuel cell applications, Applied Catalysis A: General 332 (2007) 289–296.

[13] E. Denbnovetskaya, Preparation of solid solutions of some complex carbides of the transition metals, Soviet Powder Metallurgy and Metal Ceramics 6 (1967) 194–197.

[14] K. Yvon, H. Nowotny, P. Benesovsky, Zur kristallstruktur von w2c, Monatshefte für Chemie 99 (1968) 726–729.

[15] C. A. Vanderborgh, Y. K. Vohra, H. Xia, A. L. Ruoff, bcc lead at 109 gpa: Diffraction studies to 208 gpa, Phys. Rev. B 41 (1990) 7338–7340.

[16] M. Zellner, J. Chen, Surface science and electrochemical studies of wc and w2c pvd films as potential electrocatalysts, Catal Today 99 (2005) 299–307.

[17] E. Weigert, D. Esposito, J. Chen, Cyclic voltammetry and x-ray photoelectron spectroscopy studies of electrochemical stability of clean and pt-modified tungsten and molybdenum carbide (wc and mo2c) electrocatalysts, J Power Sources 193 (2009) 501–506.

[18] A. Hamnett, B. Kennedy, Bimetallic carbon supported anodes for the direct methanol-air fuel cell, Electrochim Acta 33 (1988) 1613–1618.

[19] M. Watanabe, M. Uchida, S. Motoo, Preparation of highly dispersed pt+ru alloy clusters and the activity for the electrooxidation of methanol, J Electroanal Chem 229 (1987) 395–406.

CHAPTER IV

Electrocatalyst performance in a PEM reactor

4.1 Introduction

Recently, the use of a semi-batch electrochemical reactor with a solid-polymer electrolyte (SPE) has been reported for selective oxidation of glycerol due to some advantages described earlier. This chapter explores a highly-selective process for glycerol partial oxidation, and investigates the reaction mechanisms in a PEM reactor using carbon-supported Pt-based catalysts (Pt black, Pt/C, and Pt-Ru/C) previously selected in Chapter 3.

4.2 Experimental

4.2.1 Membrane electrode assembly fabrication

Noble metals (20 wt%Pt/C, 20 wt%Pt-10 wt%Ru/C (Alfa Aesar), Pt black (Alfa Aesar), and Ru-black (Sigma-Aldrich)), were used as received.

MEAs were prepared by painting the catalyst slurry onto the carbon cloth GDLs with the desired weight loadings using a paintbrush. Catalyst slurry was prepared by mixing catalyst powder with ultrapure water, isopropanol, and Nafion® perfluorinated resin solution (5 wt%, Sigma-Aldrich) for both the anode and cathode. The target concentration for the perfluorinated resin solution in the catalyst ink was 20

wt% with respect to the catalyst weight. Catalyst loadings were controlled by measuring the weight increase per unit area (e.g. 1 mg-Pt/cm^2). After loading the desired amount of catalyst on the GDLs, they were dried in an oven at 110 °C for 1 hour to remove adsorbed water and isopropanol. Each GDL has an area of 6.45 cm^2. A Nafion® membrane (N117 obtained from Ion Power, Inc.) was pretreated using the method described previously in Section 2.3.5 and stored inside the water until use. After the GDLs were dried, the Nafion® membrane was sandwiched between the anode and cathode GDLs, and these three layers were hot pressed together at 135 °C with a pressure of 56 kg/cm^2 for 5 minutes. The resulting MEAs were used to measure electrocatalytic activities and selectivities in a PEM reactor.

4.2.2   Rate and selectivity measurement in a PEM reactor

The SPE reactor was assembled according to the method described in Section 2.4.2 by placing the MEA between the Teflon® gaskets, the graphite blocks, and the copper plates. The humidified N$_2$ gas was supplied to the reactor for 24 hours to fully hydrate the MEA prior to the MEA performance evaluation to ensure good proton conduction in the Nafion®. The evaluations were carried out using the standard conditions listed in Table 2.2 unless otherwise stated.

4.2.3   Product analysis of glycerol oxidation

The resulting liquid products were analyzed using a GC equipped with FID and MS. A Varian GC-450 and MS-220 was used, along with a Varian CP-WAX column. Liquid samples were taken periodically throughout each run for up to 24 hours. The samples were characterized by diluting them with ethanol (99.5+%, ACS-grade, Acros Organics) to make 1 vol% and injected into the column with a syringe. The column was first heated at 40 °C and held at that temperature for 5 minutes and then ramped up with a heating rate of 10 °C/min and held at 220 °C for 10 minutes.

The gas products were analyzed using a GC-TCD (8610 GC, SRI Instruments). The GC was directly connected to either anode or cathode gas effluent. The gas concentration was measured every 30 minutes during the reaction. A SUPELCO 60/80 Carboxen-1000 column was used for separating gases. Argon was used as a carrier gas. The condenser was placed before entering the GC to remove the moisture in the exit stream. After injection of gas samples, the column was held at 70 °C for 5 minutes and then ramped up with a heating rate of 20 °C/min and held at 220 °C for 12.5 minutes.

4.3 Results and discussion

4.3.1 Rate of glycerol oxidation

4.3.1.1 Reaction order of glycerol oxidation

The reaction order was experimentally determined by evaluating activities for each electrocatalyst under constant potential at various applied potentials. As shown in Figure 4.1, the plot for the relative glycerol concentration vs. time produced a straight line for the evaluated potential range (0.4 V to 1.5 V vs. RHE), which indicated first-order kinetics. It is also reported in the literature that glycerol electrooxidation is of first order [1], suggesting our data is consistent with other work.
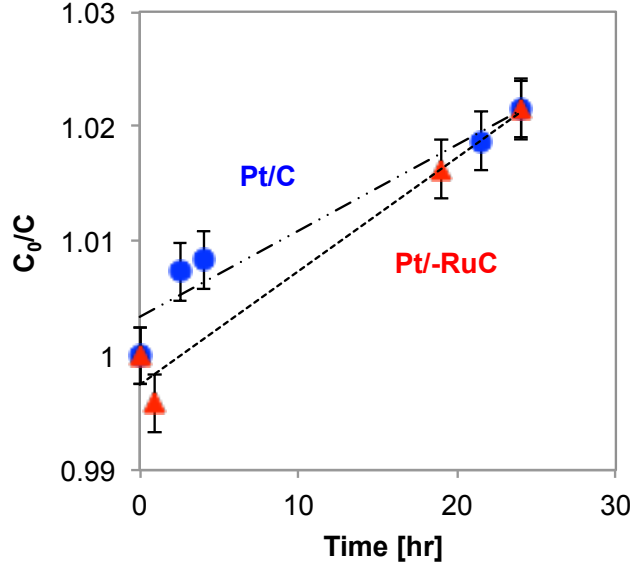
Figure 4.1: Initial glycerol concentration over glycerol concentration at time t during reaction at 1.2 V vs. RHE for Pt/C and Pt-Ru/C.

4.3.1.2 Rate constant of glycerol oxidation

To calculate the rate constants, the PEM reactor was assumed to be a single continuous stirred-tank reactor (CSTR) operated at steady-state. The glycerol solution in the PEM reactor was continuously stirred and recycled throughout the reaction. The reaction was operated under a smaller extent of conversion (less than 5%) than that which one would get from a batch system, which also justifies this assumption. Based on the first-order rate law equation determined in Section 4.3.1.1, along with a mole balance for a CSTR, a rate constant k was calculated for Pt/C and Pt-Ru/C, which was normalized by the weight of Pt for comparison.

$$r = -kC \quad \text{First order rate law} \tag{4.1}$$

$$V = \frac{(C_0 - C)\,Q}{-r} \quad \text{Mole balance of a CSTR} \tag{4.2}$$

$$k = \frac{Q}{V}\left(\frac{C_0}{C} - 1\right) \quad \text{Derived rate constant} \tag{4.3}$$

71

where Q is the volumetric flow rate [mL/s], V is the volume of glycerol solution [mL], C_0 is the initial concentration of glycerol [M], and C is the final concentration of glycerol [M].

As shown in Figure 4.2, the glycerol oxidation rates generally increased with potential for both Pt/C and Pt-Ru/C, and some regions increased exponentially, which would be consistent with the Butler-Volmer model of electrode kinetics [2].

$$i = i_0 \left[exp\left(\frac{-\alpha n F \eta}{RT} \right) - exp\left(\frac{(1-\alpha)nF\eta}{RT} \right) \right] \quad \text{Butler-Volmer equation} \quad (4.4)$$

where i_0 is the exchange current, α is the transfer coefficient, n is the stoichiometric number of electrons involved in an electrode reaction, F is the Faraday constant, η is the overpotentail defined as $\eta = E - E_{\text{eq}}$, E is the applied potential, E_{eq} is the equilibrium potential of the reaction, R is the gas constant, and T is the temperature.
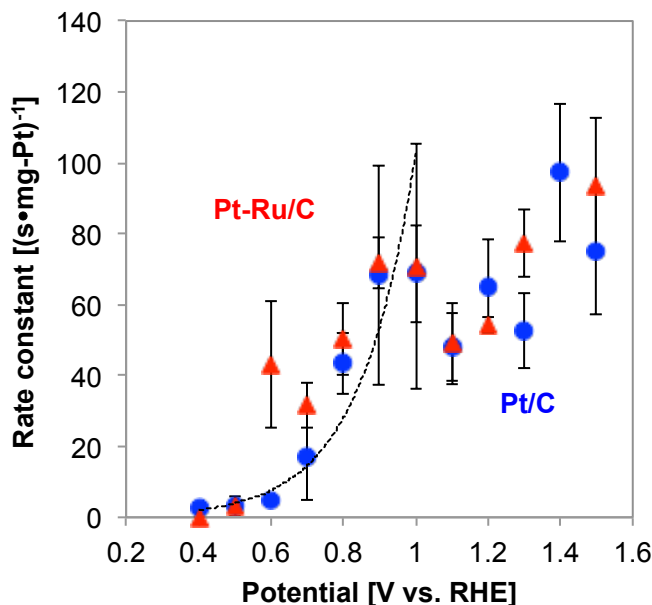

Figure 4.2: Rate constants of glycerol oxidation at various potentials for Pt/C and Pt-Ru/C.

The Butler-Volmer formulation describes how electrical current, which can be related

to the rate constant, depends on the electrode potential. This equation is valid when the electrode reaction is controlled by electrical charge transfer. Above 1.0 V vs. RHE in Figure 4.2, the rate is likely limited by mass transfer of glycerol from the bulk to the electrode surface.

The rates for Pt/C and Pt-Ru/C lay on top of each other, indicating they both had similar activities towards glycerol oxidation and addition of Ru did not affect their rates. This result confirmed that Pt alone is the active catalyst for glycerol oxidation. In other words, Ru does not directly participate in oxidizing glycerol, but rather indirectly assists the reaction as a major role.

However, these rate constants were determined by overall glycerol conversion, which included both electrochemical and non-electrochemical reactions. Though it may not be a major contribution judging from the substantial dependence of the rate vs. potential, non-electrochemical product formation does not involve electron transfer by definition, and thus rates would not be affected by potential. In order to analyze the reaction more accurately, electric current could be used as the measure of electrooxidation rate. This point will be discussed further to elucidate the reaction mechanisms in Section 4.3.4.

4.3.1.3 Rate of glyceraldehyde formation

Glyceraldehyde is one of the desired partial oxidation products obtained in a PEM reactor. Figure 4.3 compares the formation rate of glyceraldehyde at each applied potential for Pt/C and Pt-Ru/C. The reaction from glycerol to glyceraldehyde is expressed as follows.

$$C_3H_8O_3 \rightleftarrows C_3H_6O_3 + 2H^+ + 2e^- \tag{4.5}$$
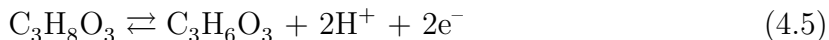
The standard potential for this reaction is approximately 0.35 V vs. NHE at

25 °C. Since thermodynamic data for glyceraldehyde were not available, calculations were made using data for lactic acid ($C_3H_6O_3$), an isomer of glyceraldehyde [3]. As shown in Figure 4.3, the rate reached a maximum at 0.8 to 1.0 V vs. RHE, and plateaued or gradually decreased despite significant applied overpotential.
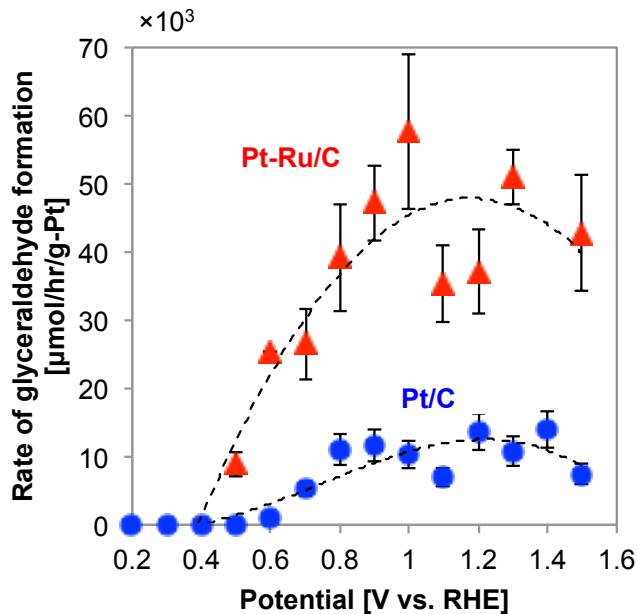
Figure 4.3: Formation rate of glyceraldehyde at various potentials for Pt/C and Pt-Ru/C.

This phenomenon could primarily be explained by mass transport limitation with respect to glycerol as the rate became limited by the diffusion of glycerol to the catalyst surface above 1.0 V. However, the rate kept falling above 1.0 V instead of leveling off to a constant, suggesting the presence of additional factors that limit the formation rate. Other factors that limit glyceraldehyde formation might be the existence of predominant competing reactions. One of the competing reactions is water oxidation at the anode, a common limitation for the aqueous system.

$$O_2 + 4H^+ + 4e^- \rightleftarrows 2H_2O \quad E^0 = 1.23 \text{ V vs. NHE} \quad (4.6)$$
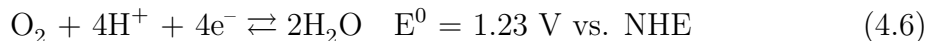
The dissociated protons transport across the Nafion® membrane, and the hydrogen evolution reaction (HER) occurs at the cathode.

$$2H^+ + 2e^- \rightleftarrows H_2 \quad E^0 = 0 \text{ V vs. NHE} \tag{4.7}$$
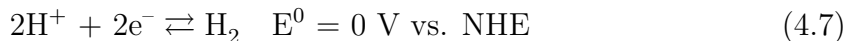
As shown in Figure 4.4, the H_2 concentration detected from the cathode started to take off after 1.0 V. This is a clear indication of HER rate increase at higher potential. Besides water oxidation and glycerol partial oxidation to produce C3 products, there are other reaction pathways to produce C1 or C2 products via C−C bond cleavage. As a matter of fact, the CO_2 concentration produced as a result of C−C bond cleavage at the anode substantially increased after 1.0 V vs. RHE as shown in Figure 4.4.
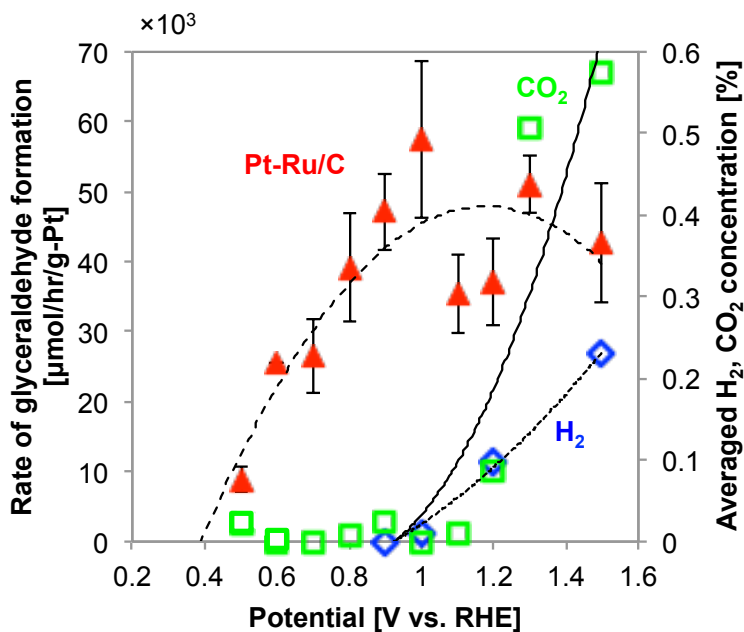
Figure 4.4: Formation rate of glyceraldehyde for Pt-Ru/C and its correlation with CO_2 via C−C bond cleavage and H_2 via water oxidation.

These competing reactions are potential dependent as indicated in Equation 4.5 and Equation 4.6. The latter equation becomes more dominant at higher potential, re-

sulting in occupation of the active sites that were originally available for glycerol oxidation.

4.3.2   Selectivity analysis of glycerol oxidation

GC analyses of the product solution indicated the presence of the five major products listed in Figure 4.5. Some are partial oxidation products, dissociative oxidation products or thermochemical dehydration products; differences can be assessed by examining the oxidation number compared to that of glycerol (indicated in the black box).
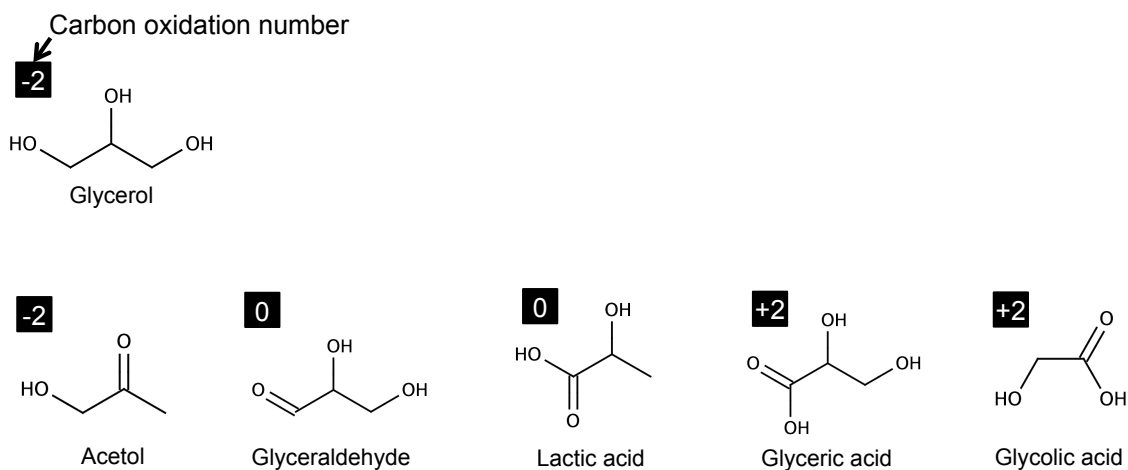
Figure 4.5: Molecular structure of glycerol and five major products with carbon oxidation numbers.

Selectivities for each electrocatalyst were evaluated at various constant potentials as shown in Figure 4.6 to Figure 4.10. There seems to have been acid-catalyzed dehydration to produce acetol. Acetol was categorized as a non-oxidation product because there was no net change in the carbon oxidation number compared to that of glycerol. This dehydration reaction did not show potential dependence based on relatively constant selectivity throughout the entire potential range. Selectivity

towards glyceraldehyde was much higher for Pt-Ru/C compared to Pt/C. Lactic acid
yield was quite small for both Pt/C and Pt-Ru/C. Lactic acid is a precursor for bio-
degradable polymers such as PLA (poly lactic acid). Glyceric acid was produced by
further oxidation of glyceraldehyde or lactic acid. Interestingly, more glyceric acid
was produced on Pt/C compared to Pt-Ru/C, which may be due to different reaction
mechanisms between these two catalysts. Finally, selectivity towards glycol acid was
relatively small but became significant for Pt/C beyond 0.8 V vs. RHE.
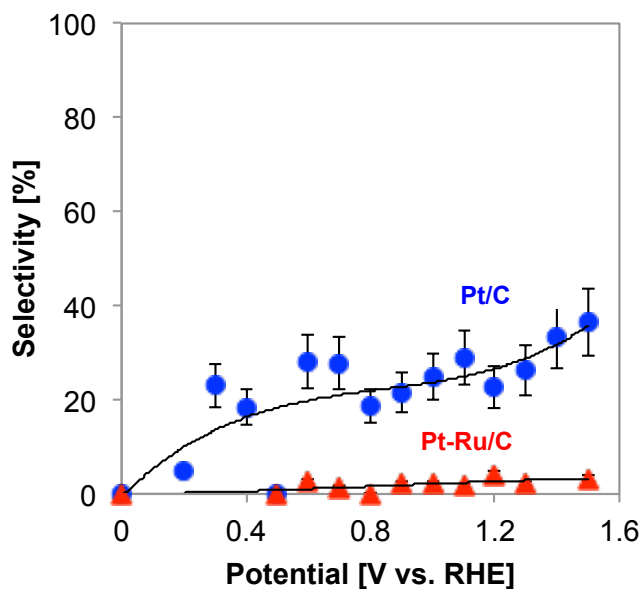
Figure 4.6: Selectivity towards acetol at various potentials for Pt/C and Pt-Ru/C.
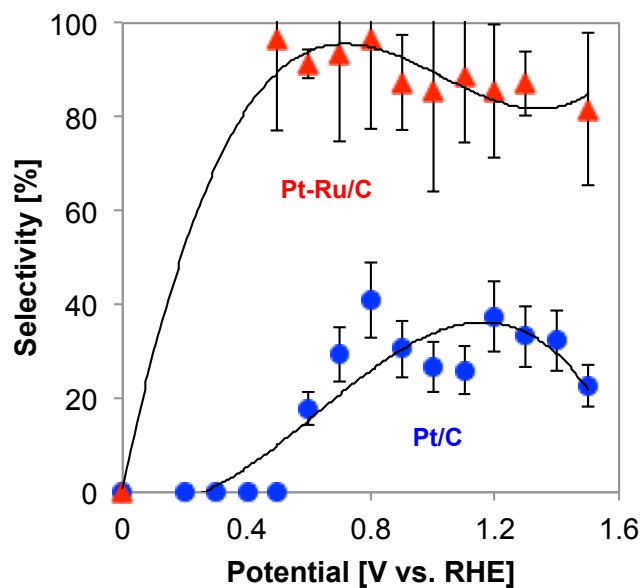
Figure 4.7: Selectivity towards glyceraldehyde at various potentials for Pt/C and Pt-Ru/C.
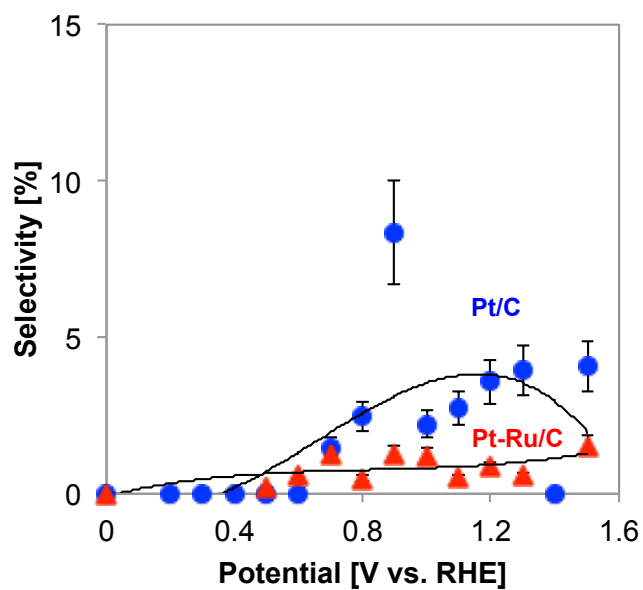
Figure 4.8: Selectivity towards lactic acid at various potentials for Pt/C and Pt-Ru/C.
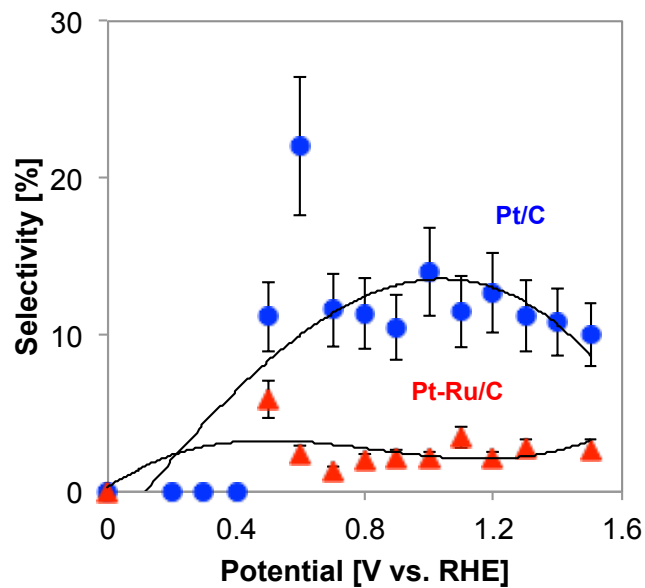
Figure 4.9: Selectivity towards glyceric acid at various potentials for Pt/C and Pt-Ru/C.
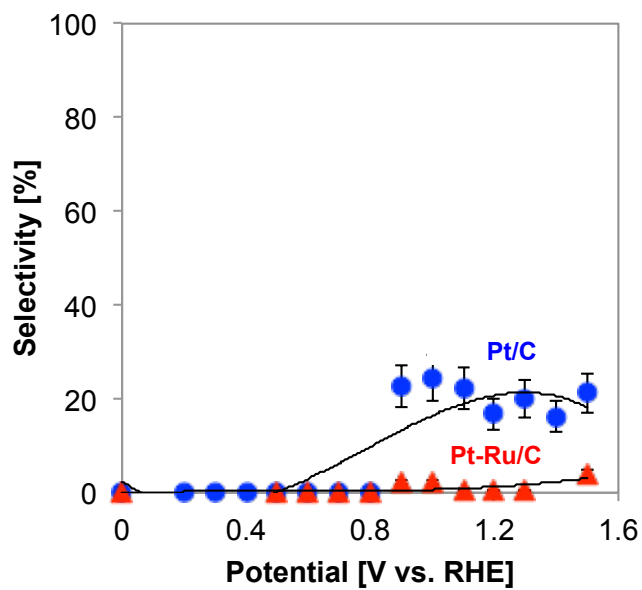
Figure 4.10: Selectivity towards glycolic acid at various potentials for Pt/C and Pt-Ru/C.

Figure 4.11 compares the selectivity evaluated at 0.9 V vs. RHE for Pt black, Pt/C and Pt-Ru/C. The Pt black or Pt/C catalyst was more selective toward dissociative oxidation products (e.g. glycolic acid) as a result of C−C bond cleavage. However, the Pt-Ru/C catalyst was significantly more selective toward partial oxidation products (e.g. glyceraldehyde).
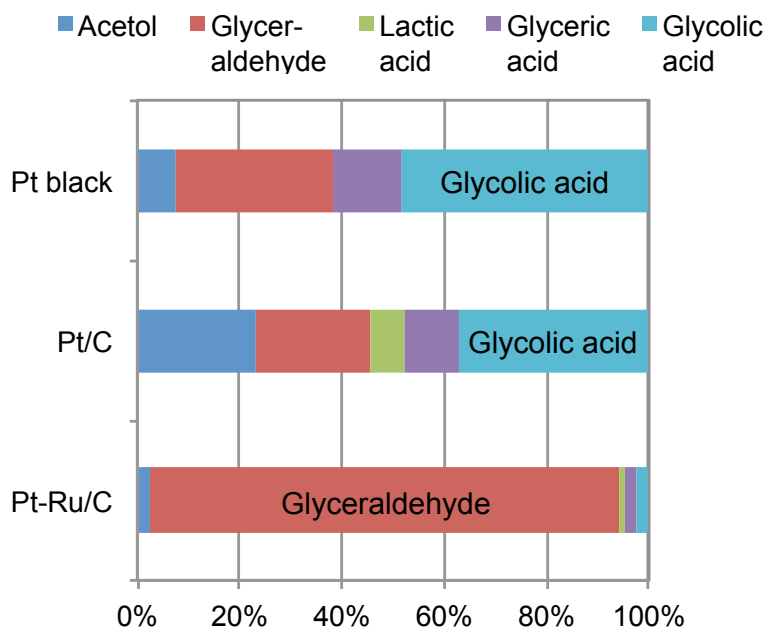
Figure 4.11: Selectivity at 0.9V for Pt-black, Pt/C and Pt-Ru/C.

Unlike the reaction rates (Section 4.3.1.2), where addition of Ru had almost no effect on improving rates, quite significant change in selectivity was observed between Pt and Pt-Ru. A similar change in selectivity has been observed for methanol oxidation, which produced more formaldehyde or formic acid than CO_2 for Pt-Ru compared to Pt by itself [4]. This provides significant support for the hypothesis that glycerol and methanol oxidation initiate similarly on these catalysts. Since the rate for the Ru black by itself was negligible based on the separate experiment, addition of Ru possibly altered the catalyst's surface chemistry, which was more favorable for partial oxidation. And most importantly, this suggests that Pt-alloy catalysts could

be developed for the selective oxidation of glycerol to value-added chemicals.

4.3.3 Current efficiency

Current efficiency (CE) was used as a measure for how efficiently the input potential (or current) was used for producing chemicals. CE for this reaction was determined by the following equation.

$$CE\ [\%] = \frac{\text{Number of H transferred from glycerol via electrooxidation}}{\text{Total number of H produced during the reaction}} \tag{4.8}$$

As shown in Figure 4.12, CE for Pt/C and Pt-Ru/C were relative low, ranging from 10 to 40%. Generally for Pt/C, higher overpotential resulted in lower CE, which was consistent with the literature [5]. For Pt-Ru/C, the CE stayed around 10 to 20% at lower potential. This is indicative of potential-dependent side reactions in addition to glycerol oxidation. One possibility is activation of water molecules on Ru to produce surface hydroxyl [6] that is necessary to oxidize poisoning species such as CO.

$$H_2O + Ru \rightarrow Ru\text{-}OH + H^+ + e^- \quad E^0 = 0.35 \text{ V vs. RHE} \tag{4.9}$$

Although the poison resistance and product selectivity can be improved by this reaction, there seems to be a sacrifice in CE for Pt-Ru/C compared to Pt/C.
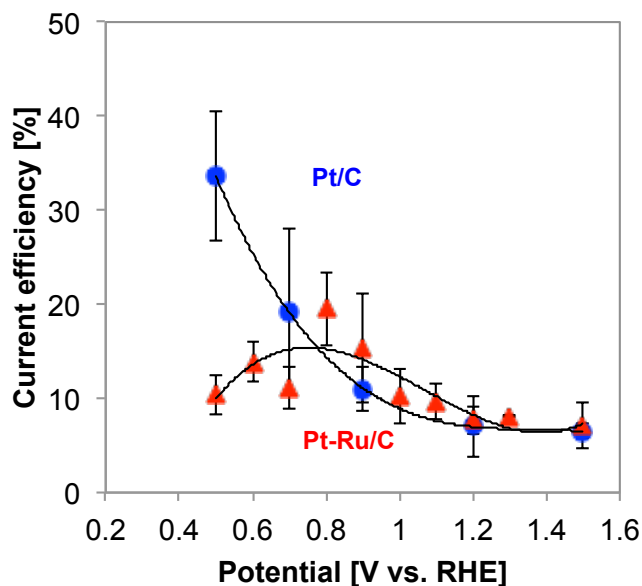
Figure 4.12: Current efficiency at various potentials for Pt/C and Pt-Ru/C.

4.3.4 Glycerol oxidation mechanisms in a PEM reactor

4.3.4.1 Glycerol oxidation pathways in a PEM reactor

Based on the types of products obtained from the evaluations in a PEM reactor, there seem to be three main reaction pathways: partial oxidation, dissociative oxidation, and dehydration. Figure 4.13 shows a summary of possible reaction pathways occurring in this system. First, glycerol is oxidized to glyceraldehyde, isomerized to lactic acid, and further oxidized to glyceric acid. Glycolic acid and CO_2 are formed by C−C bond cleavage. The third pathway is the formation of acetol, which can be produced via acid-catalyzed dehydration in contact with a Nafion® membrane. Nafion® can be the source for the protons for this reaction as it is highly acidic when hydrated.
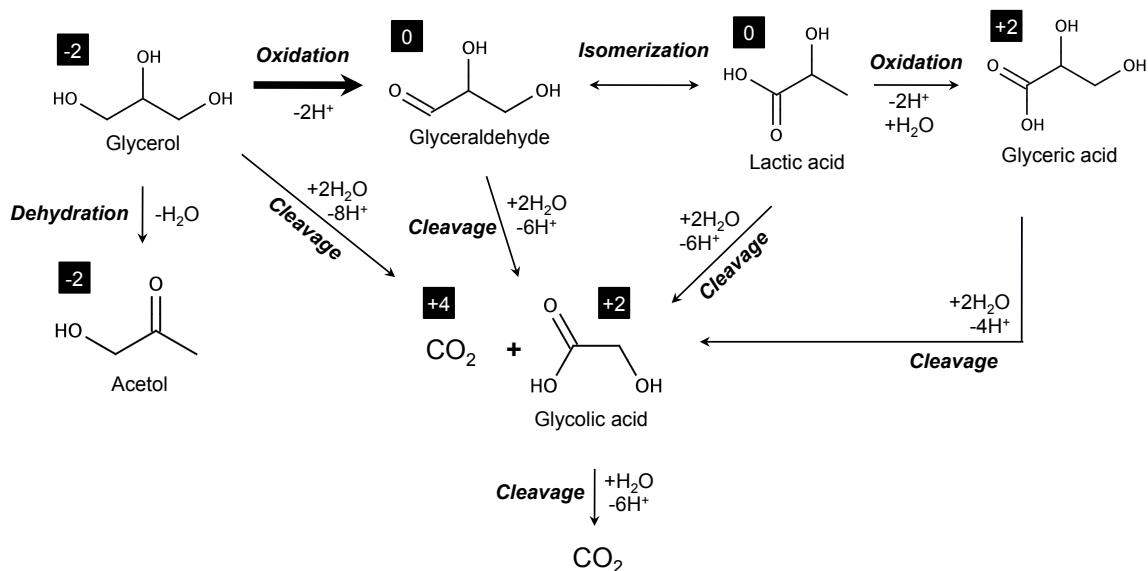
Figure 4.13: Glycerol oxidation pathways in a PEM reactor.

As shown by Lux et al., the reaction pathway and product selectivity can be greatly influenced by the acidity of the electrolyte [7]. In an acidic environment, only glyceraldehyde was produced as a primary intermediate. However, in a basic environment, a mixture of glyceraldehyde and dihydroxyacetone was observed, as shown in Figure 4.14. Our reaction pathways were similar to Lux et al.'s acidic pathways because the PEM reactor provides an acidic environment.
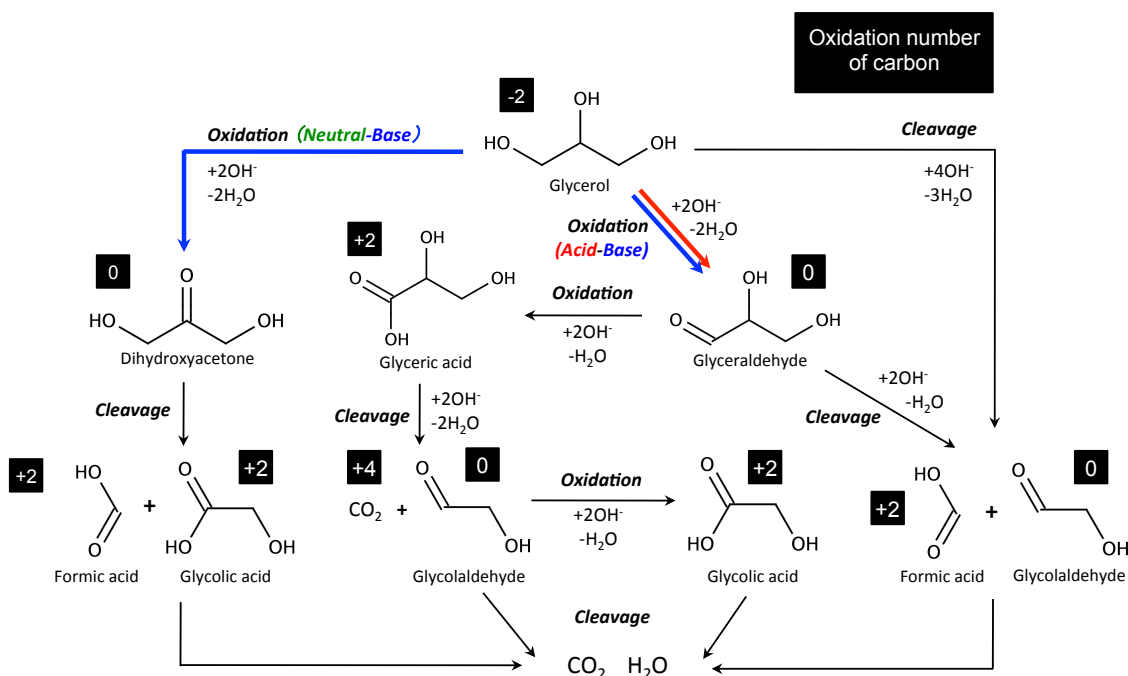
Figure 4.14: Glycerol oxidation pathways suggested by Lux et al. [7].

4.3.4.2 Investigating the selectivity shift

Pt/C and Pt-Ru/C exhibited similar glycerol conversion rates but significantly different selectivity towards partial oxidation products. As mentioned earlier, Ru by itself was not active for glycerol oxidation, indicating some change in surface chemistry by adding Ru to Pt, which could be responsible for altering selectivity. This hypothesis was further investigated by the Tafel plot analysis. This type of plot has been widely used to understand the reaction mechanisms associated with the rate-determining steps. Under the constant potential experiments in a PEM reactor, the current response typically showed a decay as indicated qualitatively in Figure 4.15. The Tafel plot was constructed by reading the current response at some fixed times (60 seconds and 24 hours) after the start of reaction. There may be a concern regarding the time required to fully develop the concentration profile for

84

glycerol at the beginning of the reaction. To minimize this time, glycerol solution was heated and circulated for 1 hour prior to the experiment. The open circuit potential was also constantly monitored and the potential was applied upon reaching a steady-state.
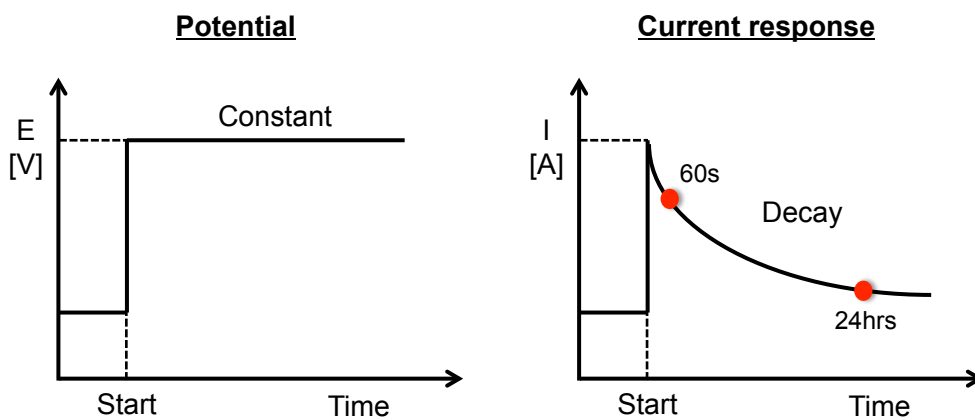
Figure 4.15: Applied constant potential and the current response.

Figure 4.16 and 4.17 show the Tafel plots for the current at 60 seconds and at 24 hours for Pt/C and Pt-Ru/C respectively. There is a clear distinction between the magnitude of current at 60 seconds and the magnitude at 24 hours, and this trend persisted for both Pt/C and Pt-Ru/C. Given that current can be correlated with the activity of electrocatalysts, this current decrease typically suggests some degree of catalyst deactivation, which will be further investigated in Chapter 5.
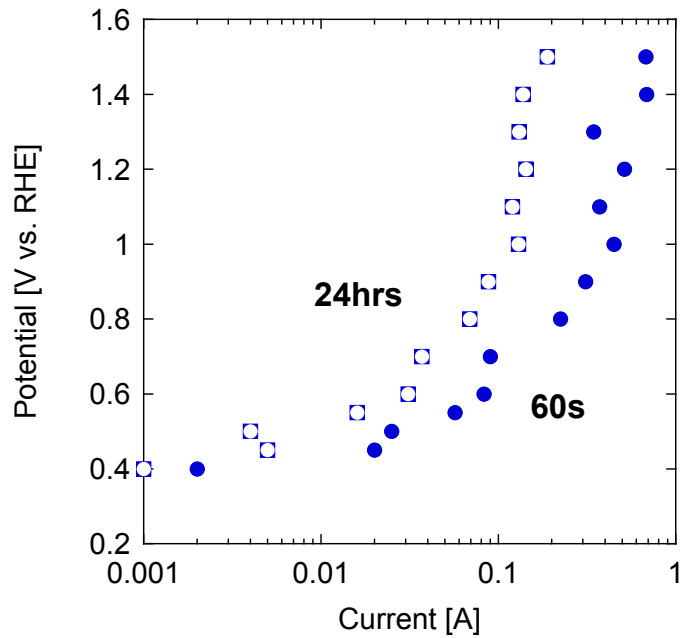
Figure 4.16: Comparison of the current for Pt/C at 60 seconds and 24 hours at each potential.
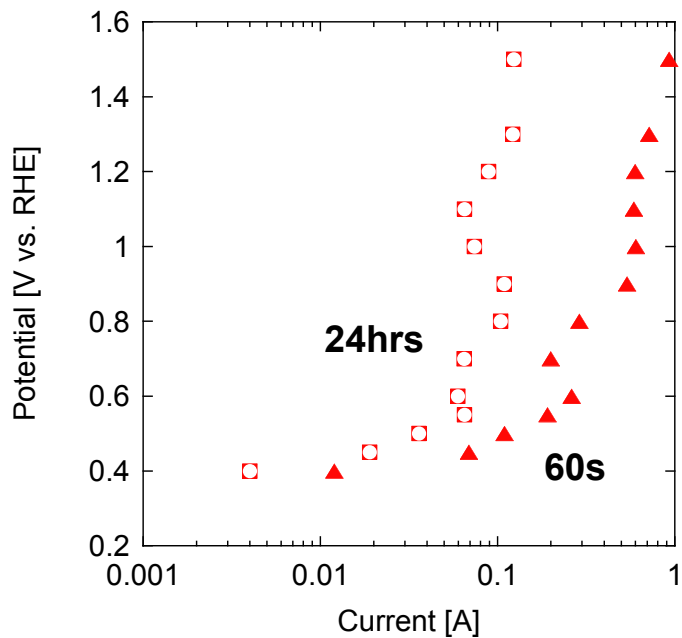
Figure 4.17: Comparison of the current for Pt/C at 60 seconds and 24 hours at each potential.

Employing the same set of data from Figure 4.16 and 4.17, the Tafel plot was next compared in terms of electrocatalyst. Figure 4.18 shows the Tafel plots for Pt/C and Pt-Ru/C, both at 60 seconds. As discussed in Section 4.3.1.2, the rate constants were very similar for Pt/C and Pt-Ru/C. However, the current for Pt/C and Pt-Ru/C was observed to be different, and in some regions, those gaps were almost an order of magnitude wide. The current for Pt-Ru/C was consistently higher than that for Pt/C.
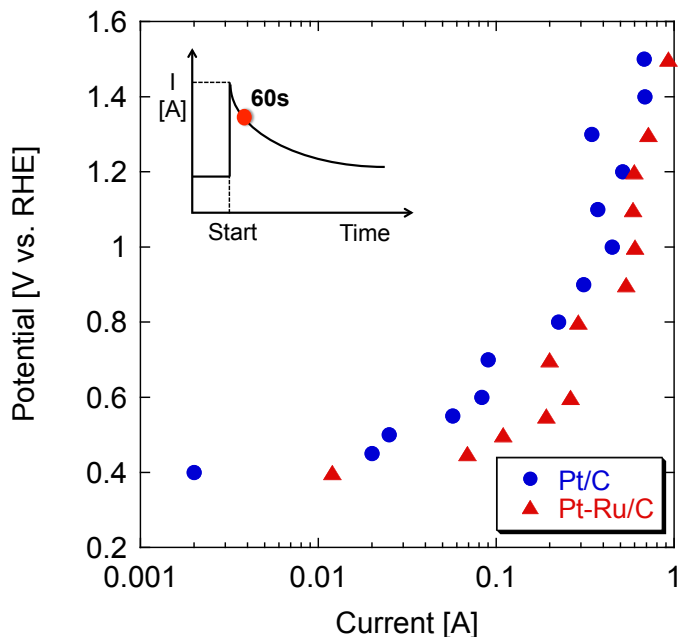
Figure 4.18: Comparison of the current for Pt/C and Pt-Ru/C at 60 seconds at each potential.

This enhancement of current for Pt-Ru/C can be explained by the ability of Ru to oxidize poisoning species at much lower potentials than those for Pt by itself [6].

$$H_2O + Pt \rightarrow Pt\text{-}OH + H^+ + e^- \quad E^0 = 0.75 \text{ V vs. RHE} \quad (4.10)$$

$$H_2O + Ru \rightarrow Ru\text{-}OH + H^+ + e^- \quad E^0 = 0.35 \text{ V vs. RHE} \quad (4.11)$$
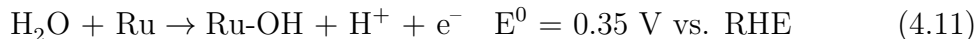
Ru supplies surface hydroxyl at as low as 0.35 V vs. RHE, which provides more active

sites, leading to a higher current.

A similar trend was confirmed in the Tafel plots for 24 hours as shown in Figure 4.19, except for the current above 1.0 V vs. RHE. For this region, both Pt and Pt-Ru gained enough overpotential to oxidize the poisoning species, and therefore the gap was smaller between catalysts. Also, these catalysts might be greatly deactivated by other factors besides poisoning, resulting in a different trend compared to that for 60 seconds.
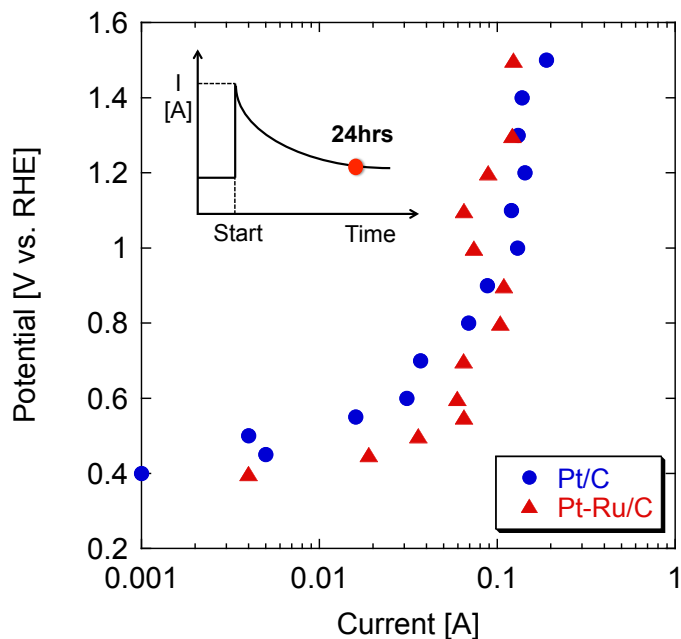
Figure 4.19: Comparison of the current for Pt/C and Pt-Ru/C at 24 hours at each potential.

The slope of the plot in the kinetically limited regime could provide some insights regarding reaction mechanisms. Different slopes suggest different rate-determining steps. Tafel plots usually exist in kinetically limited regimes at $\eta > 0.1$ V [2]. For glycerol oxidation, the beginning of the kinetically limited regime is located approximately at 0.45 V vs. RHE. As shown in in Figure 4.20, one clear distinction was observed at 0.7 V vs. RHE where the slope became much steeper. Typically in this region, the reaction is no longer limited only by kinetics but also by mass transport,

and therefore it should be excluded from obtaining mechanistic information.

The Tafel slope for Pt/C and Pt-Ru/C was determined from 0.45 V to 0.6 V vs. RHE. The slope for Pt/C was 216 ± 33 mV/dec, and the slope for Pt-Ru/C was 249 ± 19 mV/dec.
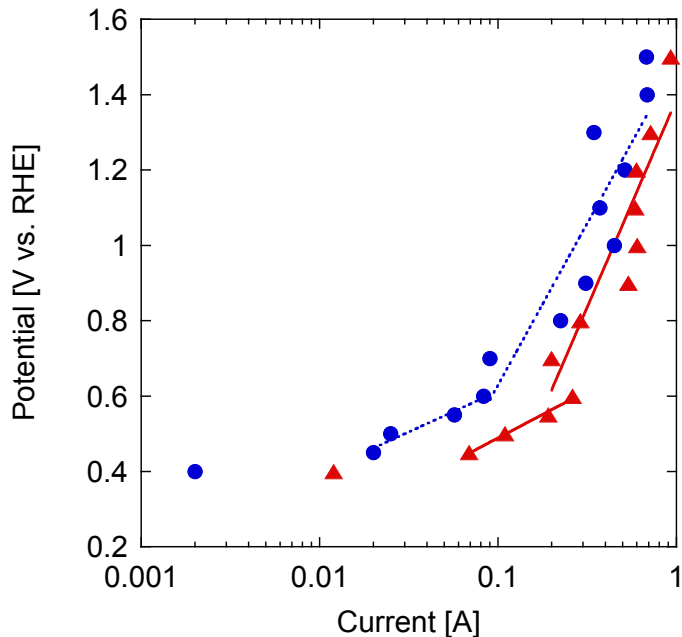
Figure 4.20: Comparison of the slopes for Pt/C and Pt-Ru/C at each potential.

While relatively little research has been reported regarding glycerol oxidation, there have been some reports of Tafel slopes for methanol oxidation. Schmidt et al. showed a Tafel slope around 80 mV/dec for Pt electrode, with the oxidative removal of CO being the rate-determining step (Faradaic rate-determining step). A relatively high Tafel slope of 195 mV/dec was reported for Pt-Ru, which was attributed to a change in the rate-limiting step to the initial methanol dehydrogenation (chemical rate-determining step) to hydroxymethyl (CH_2OH) [8].
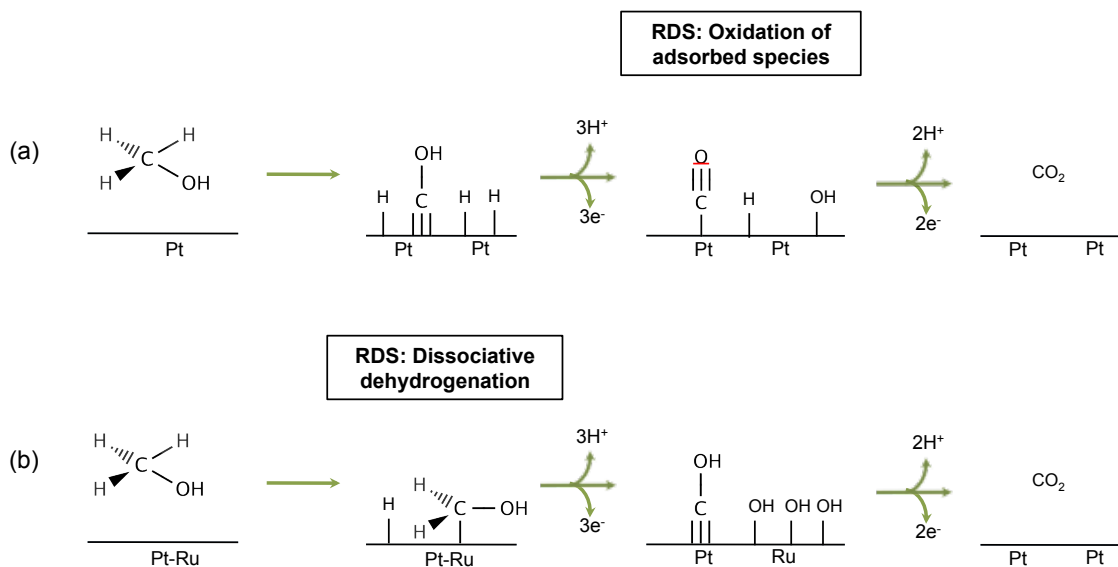
Figure 4.21: Methanol oxidation mechanisms on (a) Pt surface, and (b) Pt-Ru surface [8, 9].
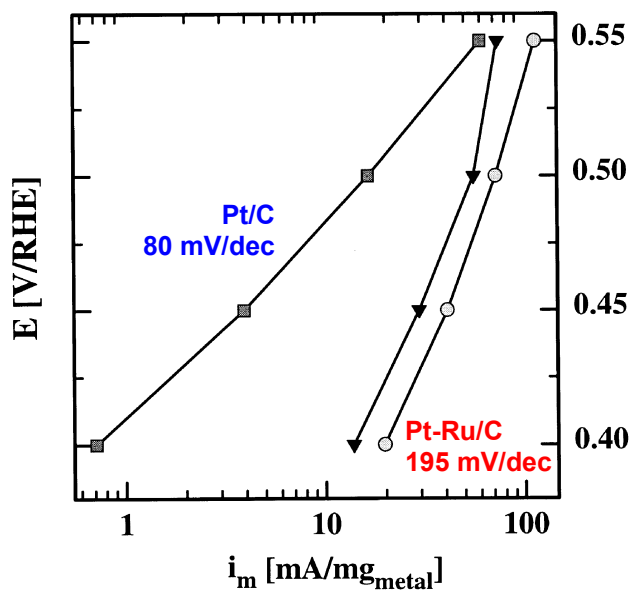
Figure 4.22: Tafel slopes for methanol oxidation over Pt/C and Pt-Ru/C (Half cell, 0.5M Methanol in 0.5M H_2SO_4) [8].

Our results for glycerol oxidation showed that the Tafel slope for Pt/C was 216 $\pm$ 33 mV/dec, and the slope for Pt-Ru/C was 249 $\pm$ 19 mV/dec. Considering the error range, there does not seem to be a significant difference in their slopes, as was observed for methanol oxidation. This indicates that the rate-determining steps for glycerol oxidation on on those catalysts could be very similar. Tafel slope alone cannot be used to explain the shift of product selectivities.

There have been some reports on electronic structure change of the Pt alloy and its influence on reaction mechanisms. Wakisaka et al. measured the magnitude of the core level (CL) shift for the Pt-Ru alloy, which was found to be 0.39 eV from Pt CL (Figure 4.23).
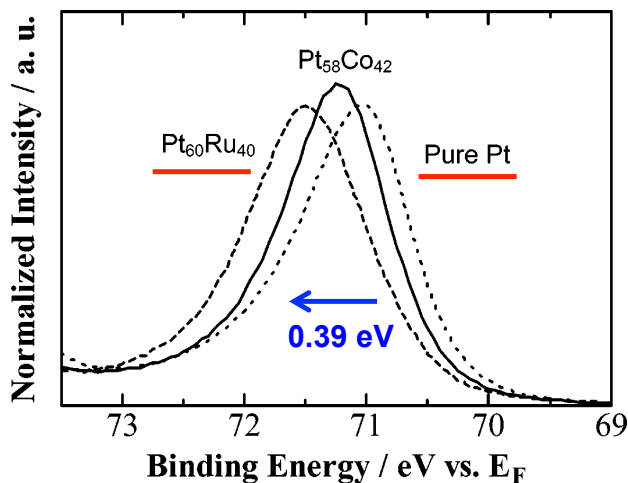
Figure 4.23: Area-normalized CL spectra of $Pt4f_{7/2}$ for pure Pt, $Pt_{58}Co_{42}$ alloy, and $Pt_{60}Ru_{40}$ alloy with respect to E_F [10].

They saw the negative shift of a Fermi level (E_F) by X-ray photoelectron spectroscopy (XPS), which resulted in a positive shift of the d-band center and the CL for the $4f_{7/2}$ electron configuration of Pt as schematically shown in Figure 4.24. The d-band center represents the electron density near the Fermi level. This shift is made by the difference in work function between pure Pt and the alloy, accompanied by rehybridization of the d-band as well as the sp-band [11].
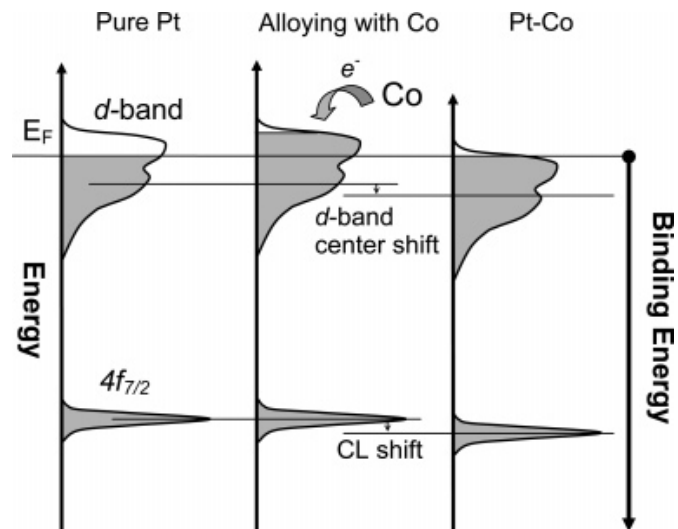
Figure 4.24: Schematic explanation of the alloying effect on the electronic structures of Pt [10].

Wakisaka et al. also found that there was a linear relationship between the shift of CL (or d-band center) and CO adsorption energy. A greater shift in CL or d-band center led to a reduction of the adsorption energy, which was an important finding to explain the enhanced CO tolerance of the Pt alloy [10].
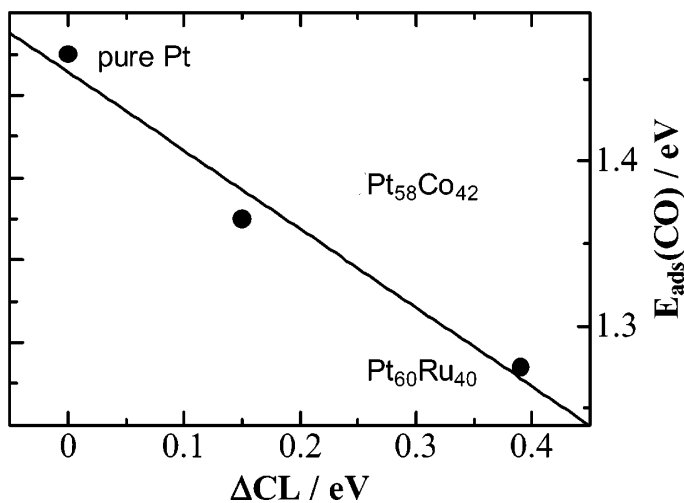
Figure 4.25: Linear relation between CL shifts and CO adsorption energies [10].

Although CO and glycerol molecules may not interact with Pt or Pt alloys similarly, it is possible that improved selectivity was due to the difference in electronic structure between Pt and Pt-Ru, which caused the adsoprtion energies of some species to change. One close measurement that could provide information about the adsorption is CV. Figure 4.26 compares the cyclic voltammogram in a Nafion® solid-state cell under the 0.1M glycerol flow. The peaks at 1.0 V for Pt/C and 0.8 V for Pt-Ru/C were related to glycerol oxidation. The onset of these peaks occurs at the potential where glycerol starts to adsorb and react on the catalyst's surface.
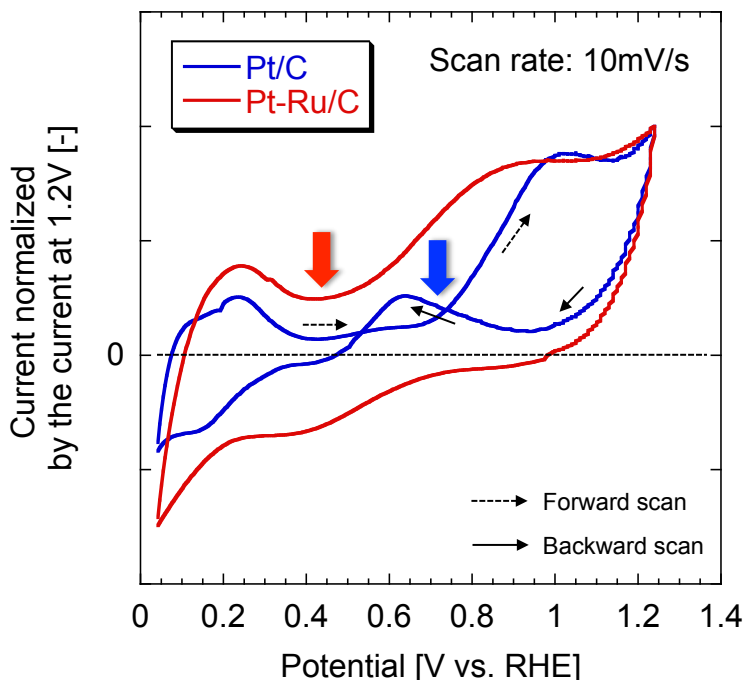
Figure 4.26: Cyclic voltammogram with 0.1M glycerol for Pt/C and Pt-Ru/C (solid-state cell, RT, 10 mL/min of 0.1M glycerol).

It is apparent that the peak onset for Pt-Ru/C was located much lower than that for Pt/C. Glycerol can be adsorbed and reacted with at as low as 0.4 V vs. RHE on a Pt-Ru surface, possibly by reducing the glycerol adsorption barrier as a result of change in electronic structure.

In Figure 4.27, the glycerol oxidation mechanism on the Pt and Pt-Ru surfaces

is elucidated. The key difference is the step indicated in the red box, at what potential glycerol adsorbs on these catalysts' surfaces, which significantly affects the subsequent reaction pathways. On the Pt surface, glycerol is adsorbed at a much higher potential ($E > 0.8$ V vs. RHE), where Pt can interact with oxygen to create Pt-O species. Surface oxygen can directly react with glycerol molecules by breaking the C−C bond. Glycerol is more strongly adsorbed since desorption or reduction of oxidized intermediates is thermodynamically unfavorable, and the residual species go through a greater extent of oxidation, resulting in the production of secondary oxidation products (e.g. glyceric acid) or dissociative oxidation products (e.g. glycolic acid).

On the other hand, for the Pt-Ru surface, glycerol adsorption occurs before the Pt surface creates Pt-O. In addition, enough OH species are provided by Ru that it is possible to oxidize surface-bonded poisoning species or destabilize the adsorbed reaction intermediates. These reaction energetics may favor the desorption of partially oxidized products (e.g glyceraldehyde) on Pt-Ru as opposed to complete oxidation to CO_2 since there was also a smaller amount of secondary oxidation product (e.g. glyceric acid) for Pt-Ru than was observed on Pt/C, according to the selectivity analysis in Section 4.3.2.
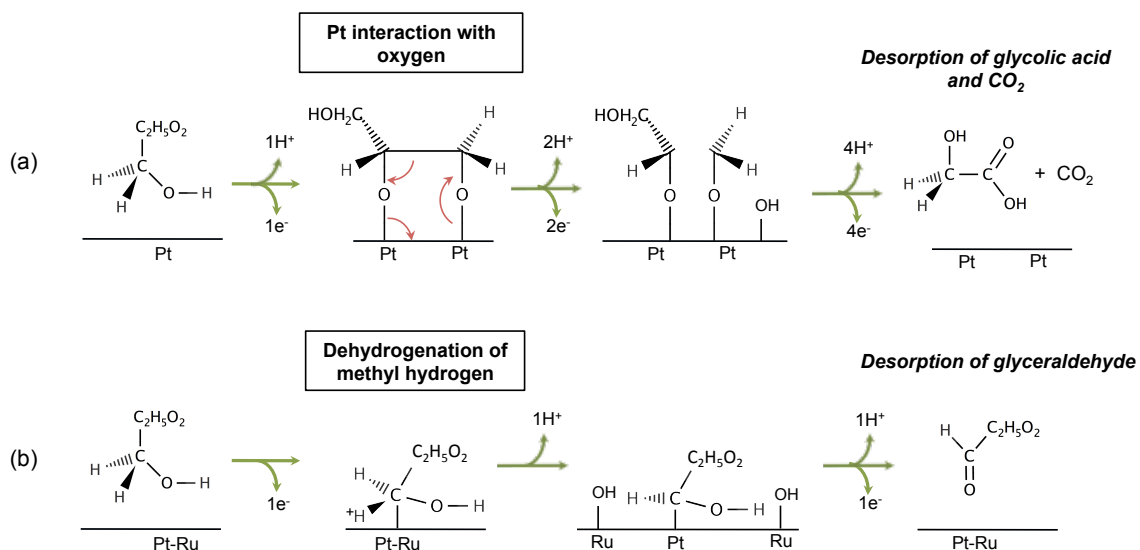
Figure 4.27: Glycerol oxidation mechanisms in a PEM reactor on (a) Pt surface, and (b) Pt-Ru surface.

4.4 Conclusions

The rate and selectivity of glycerol oxidation were evaluated on Pt/C and Pt-Ru/C in a PEM reactor. Both catalysts showed similar rate constants while exhibiting substantial differences in selectivity towards glyceraldehyde.

The glycerol oxidation mechanisms occurring on Pt and Pt-Ru surfaces were investigated. The key mechanistic differences were attributed to the nature of glycerol adsorption, which significantly affected the subsequent reaction pathways. On the Pt-Ru surface, glycerol adsorption and desorption seemed much more facile, possibly due to the difference in its electronic structure. Ru did not directly oxidize glycerol, but it prevented the severe and irreversible poisoning of Pt active sites by facilitating CO oxidation.

References

[1] L. Roquet, E. Belgsir, J. Leger, C. Lamy, Kinetics and mechanisms of the electrocatalytic oxidation of glycerol as investigated by chromatographic analysis of the reaction-products - potential and ph effects, Electrochim Acta 39 (1994) 2387–2394.

[2] A. J. Bard, L. R. Faulkner, Electrochemical methods - fundamentals and applications 2nd ed., John Wiley & Sons (2001).

[3] C. L. Yaws, Chemical properties handbook, McGraw-Hill (1999).

[4] A. Kabbabi, R. Faure, R. Durand, B. Beden, F. Hahn, J. Leger, C. Lamy, In situ ftirs study of the electrocatalytic oxidation of carbon monoxide and methanol at platinum-ruthenium bulk alloy electrodes, J Electroanal Chem 444 (1998) 41–53.

[5] P. Pintauro, M. Gil, K. Warner, G. List, W. Neff, Electrochemical hydrogenation of soybean oil with hydrogen gas, Ind Eng Chem Res 44 (2005) 6188–6195.

[6] M. Watanabe, S. Motoo, Electrocatalysis by ad-atoms .2. enhancement of oxidation of methanol on platinum by ruthenium ad-atoms, J Electroanal Chem 60 (1975) 267–273.

[7] S. Lux, P. Stehring, M. Siebenhofer, Lactic acid production as a new approach for exploitation of glycerol, Separ Sci Technol 45 (2010) 1921–1927.

[8] T. Schmidt, H. Gasteiger, R. Behm, Methanol electrooxidation on a colloidal ptru-alloy fuel-cell catalyst, Electrochemistry Communications 1 (1999) 1–4.

[9] M. P. Hogarth, T. R. Ralph, Catalysis for low temperature fuel cells part iii: Challenges for the direct methanol fuel cell, Platin Met Rev 46 (2002) 146–164.

[10] M. Wakisaka, S. Mitsui, Y. Hirose, K. Kawashima, H. Uchida, M. Watanabe, Electronic structures of pt-co and pt-ru alloys for co-tolerant anode catalysts in polymer electrolyte fuel cells studied by ec-xps, J Phys Chem B 110 (2006) 23489–23496.

[11] M. Weinert, R. Watson, Core-level shifts in bulk alloys and surface adlayers, Physical Review B 51 (1995) 17168–17180.

CHAPTER V

Deactivation mechanisms in a PEM reactor

5.1 Introduction

Chapter 4 briefly discussed the deactivation of electrocatalysts in a PEM reactor as indicated by chronoamperometry. Although some catalysts showed promising results regarding selectivities, durability of those catalysts against deactivation needs to be improved in order to assure long-term performance.

In this chapter, nonlinear regression analysis is first carried out to give us a preliminary idea about deactivation mechanisms and to suggest what type of characterization technique should be used to examine post-reaction materials. Then various characterization methods are conducted on spent catalysts to investigate the deactivation mechanisms that occurred during the operation of the PEM reactor for glycerol oxidation.

5.2 Experimental

5.2.1 Electrochemical surface area measurement in a PEM reactor

ECSA was directly measured in the PEM reactor by switching the anode and cathode gas/liquid flow as described in Section 2.6.3. An Autolab PGSTAT320N potentiostat (Metrohm AG) was used to produce cyclic voltammograms. The cath-

ode was connected to the reference and the counter electrodes, and the anode was connected to the working electrode. For all measurements, CV profiles were typically recorded between 0 and 0.8 V vs. RHE at 50 °C with a scan rate of 5 mV/s, unless otherwise stated.

5.2.2 Catalyst morphology visualization using SEM

A Philips XL 30 SEM (FEI Company) was used to visualize any change in morphology that occurred during the reaction. The fresh or spent anode catalyst was scraped from the MEAs using a spatula. The collected powder was placed on copper tape and analyzed with SEM.

5.2.3 Thermogravimetric analysis on spent catalysts

A Q50 Thermogravimetric Analyzer (TA Instruments) was used to determine the amount of extra material deposited on the spent catalyst during glycerol oxidation in a PEM reactor. Similar to the SEM analysis, the fresh or spent catalyst was scraped from the MEAs. Approximately 1 to 3 mg of material was placed on a platinum pan and heated in the furnace with exposure to 15 mL/min of dried oxygen. After equilibrating at 30 °C, the catalyst was heated to 800 °C with a heating rate of 20 °C/min.

5.2.4 Carbon support corrosion analysis

Water oxidation was conducted in a PEM reactor to measure the concentration of CO_2 associated with carbon support corrosion at the anode. The same reactor set-up and the operating conditions described in Table 2.2 were used, except for the anode flow. Here, ultrapure water was used instead of 2.7M glycerol.

5.3 Results and discussion

5.3.1 Electrochemical surface area

ECSA has been used as a measure for understanding degradation of PEM fuel cell catalysts during potential cycling [1–5]. A similar method was applied here to investigate the catalyst deactivation for glycerol oxidation in a PEM reactor by comparing ECSA of fresh and spent catalysts.

Figure 5.1 shows the cyclic voltammograms in a PEM reactor before and after glycerol oxidation.
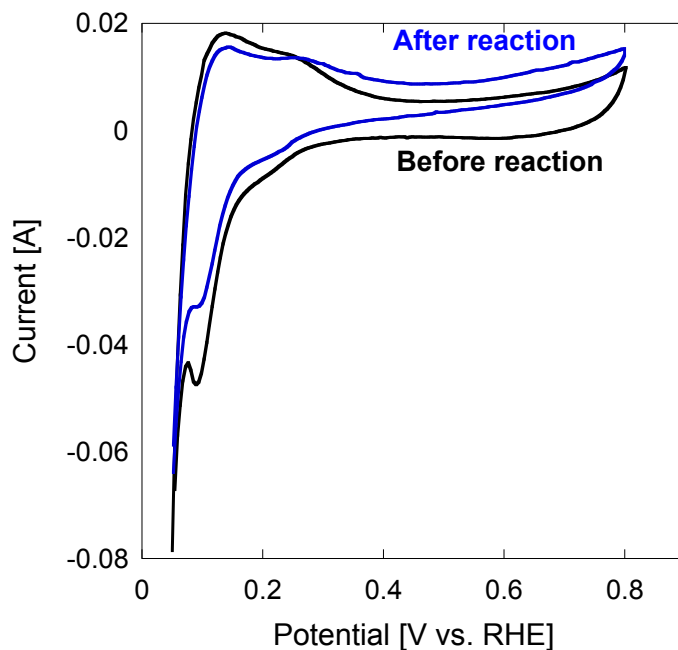
Figure 5.1: Cyclic voltammogram for the fresh and the spent MEA (Glycerol oxidation: 0.9 V vs. RHE, scan rate: 5 mV/s, anode catalyst: 20% Pt/C).

From these voltammograms, the ECSA of Pt was calculated using the mean integral charge of the hydrogen adsorption and desorption region at $0.4-0.6$ V vs. RHE, corrected for double layer current. It was assumed that one adsorbed H was observed per Pt atom, consistent with Equations 2.10 and 2.11.

Table 5.1 summarizes the ECSA loss as a function of potential. It shows a significant drop in ECSA when the reaction is operated at higher potentials. To lose about 70% of surface area, the particle's radius would be five times bigger than the initial size.

Table 5.1: ECSA loss after glycerol oxidation at various potentials for Pt/C.

ECSA $[m^2_{Pt}/g_{Pt}]$	OCV*	0.6 V	0.9 V	1.2 V	1.5 V
Before reaction	40	51	69	59	71
After reaction	39	37	24	18	23
ECSA loss	2.5%	27%	66%	70%	67%

* OCV (open circuit voltage) is the difference of electrical potential between anode and cathode when the external power supply is not connected to the PEM reactor.

The loss of ECSA has been linked to 1) catalyst particle growth, 2) Pt metal loss by dissolution into the electrolyte, and 3) carbon support corrosion associated with electrical isolation of metal nanoparticles [5]. One could also lose ECSA to site blocking by carbon deposition or poisoning.

5.3.2 Catalyst particle growth

Catalyst particle sintering has been studied as a major cause for the particle growth that causes ECSA loss. Particle sintering is the agglomeration of particles to form larger particles, which can be minimized by supporting catalysts on high surface area materials (e.g carbon) [2].

Particle growth could be confirmed by measuring the particle size using methods such as XRD. However, for these samples, XRD was not suitable due to the presence of the carbon support and Nafion® resin, which interfere with the peak identification for determining particle size.

100

5.3.3 Pt metal loss by dissolution

The Pt dissolution rate is potential dependent between 1.1 and 1.5 V in strong acid. The dissolved Pt was precipitated to form bigger Pt particles. Also significant Pt dissolution in 0.5M H_2SO_4 has been reported [3].

To study this Pt dissolution, ECSA loss was measured as a function of time. Figure 5.2 shows the surface-area loss over time when the PEM reactor was operated at 0.9 V vs. RHE. It was experimentally observed that surface area loss had reached about 70% after 50 hours.
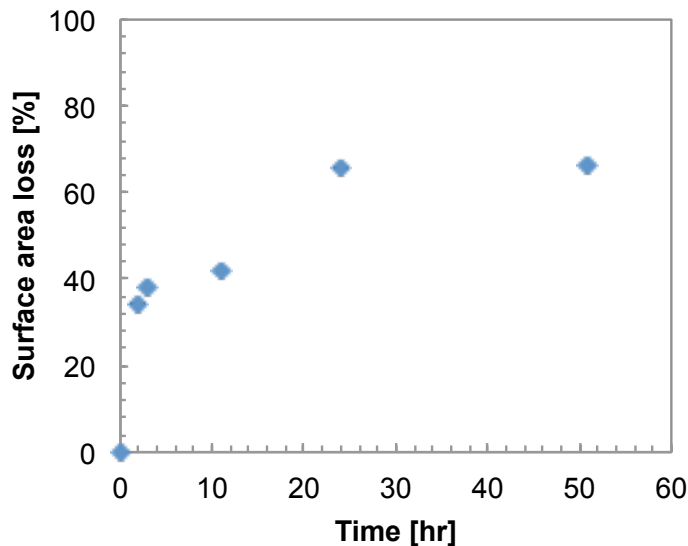
Figure 5.2: ECSA loss over time during glycerol oxidation at 0.9 V vs. RHE in a PEM reactor.

Next, the time scale to lose 70% of surface area only by Pt dissolution was theoretically determined. The maximum concentration of Pt which can be dissolved at pH = 0.3 was calculated from the following equations [6]:

$$Pt^{2+} + H_2O \rightarrow PtO + 2H^+ \tag{5.1}$$

$$\log_{10}\left[Pt^{2+}\right] = -7.06 - 2pH \tag{5.2}$$

A pH of 0.3, which represents the pH for 0.5M H_2SO_4, was considered to be close to the acidity of Nafion® and used as a good estimate. The diffusion coefficient of Pt in Nafion® was assumed to be similar to that in water, which is 1.0×10^{-9} [m^2/s] [7].

$$-J_{Pt^{2+}}(0, t) = D \left[\frac{\partial C_{Pt^{2+}}}{\partial x} \right]_{x=0} \qquad \text{Fick's law of diffusion} \qquad (5.3)$$

$$[Pt^{2+}]_{bulk} = 0 \ [\text{mol/m}^3] \quad \text{Boundary condition at bulk} \qquad (5.4)$$

$$[Pt^{2+}]_{surface} = 10^{-3} \ [\text{mol/m}^3] \quad \text{Boundary condition at surface} \qquad (5.5)$$

The diffusion equation was solved with the boundary conditions and then the time required to lose 70% of surface area was calculated by the following equation.

$$t = \frac{\text{Amount of Pt dissolved to lose 70\% of surface area}}{J \times A_{geometric}} \qquad (5.6)$$

In conclusion, it would take 10^6 hours to lose about 70% of surface area by Pt dissolution driven by the concentration gradient from surface to bulk at pH 0.3. Comparing this with the empirical result that 70% of surface area was lost in 50 hours, it is unlikely that this surface area loss was caused solely by Pt dissolution but rather than mostly by other mechanisms discussed in Section 5.3.1. Therefore, the possible effects of each of the other deactivation mechanisms were investigated by using nonlinear regression analysis of current decay and other experimental methods in order to narrow down the most relevant deactivation mechanism occurring during glycerol oxidation in a PEM reactor.

5.3.4 Nonlinear regression analysis of current decay

The current decay was observed for both Pt/C and Pt-Ru/C catalysts during the glycerol oxidation in a PEM reactor. As shown in Figures 5.3 and 5.4, approximately 80% or more compared to the initial activity has been lost for both catalysts after 24

hours of reaction.
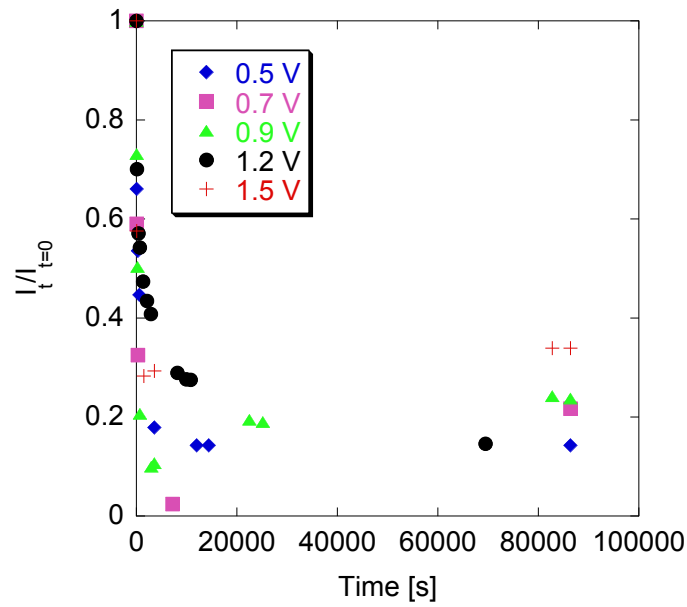
Figure 5.3: Current decay for Pt/C in a PEM reactor at constant potentials from 0.5 V to 1.5 V vs. RHE.
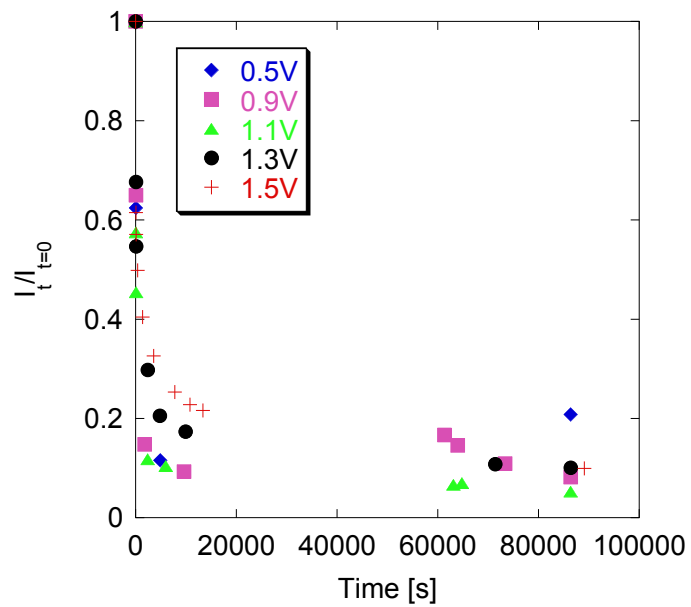
Figure 5.4: Current decay for Pt-Ru/C in a PEM reactor at constant potentials from 0.5 V to 1.5 V vs. RHE.

Nonlinear regression was used to fit the current decay to the deactivation models discussed earlier in Section 2.6.1 and in the literature [8, 9]. Mathematica® (version 8, Wolfram) was employed to calculate R^2 values. Tables 5.2 and 5.3 summarize the R^2 values for Pt/C and Pt-Ru/C at constant potentials from 0.5 V to 1.5 V vs. RHE.

Table 5.2: Deactivation model fit results for Pt/C.

Deactivation mechanism	Surface oxidation	Poisoning	Sintering	Carbon deposition
Function	Linear	Exponential	Hyperbolic	Reciprocal power
R^2				
Potential [V vs. RHE] 0.5	-0.267	0.908	0.945	0.960
0.7	-0.200	0.933	0.956	0.942
0.9	0.424	0.830	0.910	0.992
1.2	0.131	0.841	0.925	0.978
1.5	0.413	0.975	0.981	0.995
Average	**0.101**	**0.897**	**0.943**	**0.973**

Table 5.3: Deactivation model fit results for Pt-Ru/C.

Deactivation mechanism	Surface oxidation	Poisoning	Sintering	Carbon deposition
Function	Linear	Exponential	Hyperbolic	Reciprocal power
R^2				
Potential [V vs. RHE] 0.5	0.223	0.948	0.952	0.955
0.7	0.454	0.817	0.824	0.967
0.9	-0.100	0.926	0.940	0.953
1.2	0.061	0.847	0.916	0.984
1.5	0.422	0.812	0.944	0.972
Average	**0.212**	**0.870**	**0.915**	**0.966**

According to these results, all functions that were not linear (exponential, hyperbolic, and reciprocal power) showed fairly good fit in terms of R^2 value. The corresponding mechanisms are poisoning, sintering and carbon deposition respec-

tively. The results for Pt-Ru/C were similar to those for Pt/C, showing relatively high R^2 values for the three models. Reciprocal power, or carbon deposition, seemed to have the highest average R^2 value for both catalysts. However, these results did not provide enough evidence to support one deactivation mechanism over the others. It is also possible that initial catalyst deactivation is governed by one mechanism and final deactivation is governed by another. To investigate further, the experimental and theoretical results to support suggested deactivation mechanisms are discussed in the following sections.

5.3.5 Catalyst morphology

Figure 5.5 shows SEM images of fresh and spent Pt-Ru/C at various constant potentials. Surface pore structure seemed reduced for the catalyst spent at 1.5 V compared to that for the fresh catalyst. This could be due to Pt particle sintering, carbon support corrosion, or carbon deposition. All these could contribute to lowering the Pt dispersion and making the surface look more planar. However, with this SEM magnification, it is not possible to conclude upon a primary deactivation mechanism, and other experimental methods must be combined.
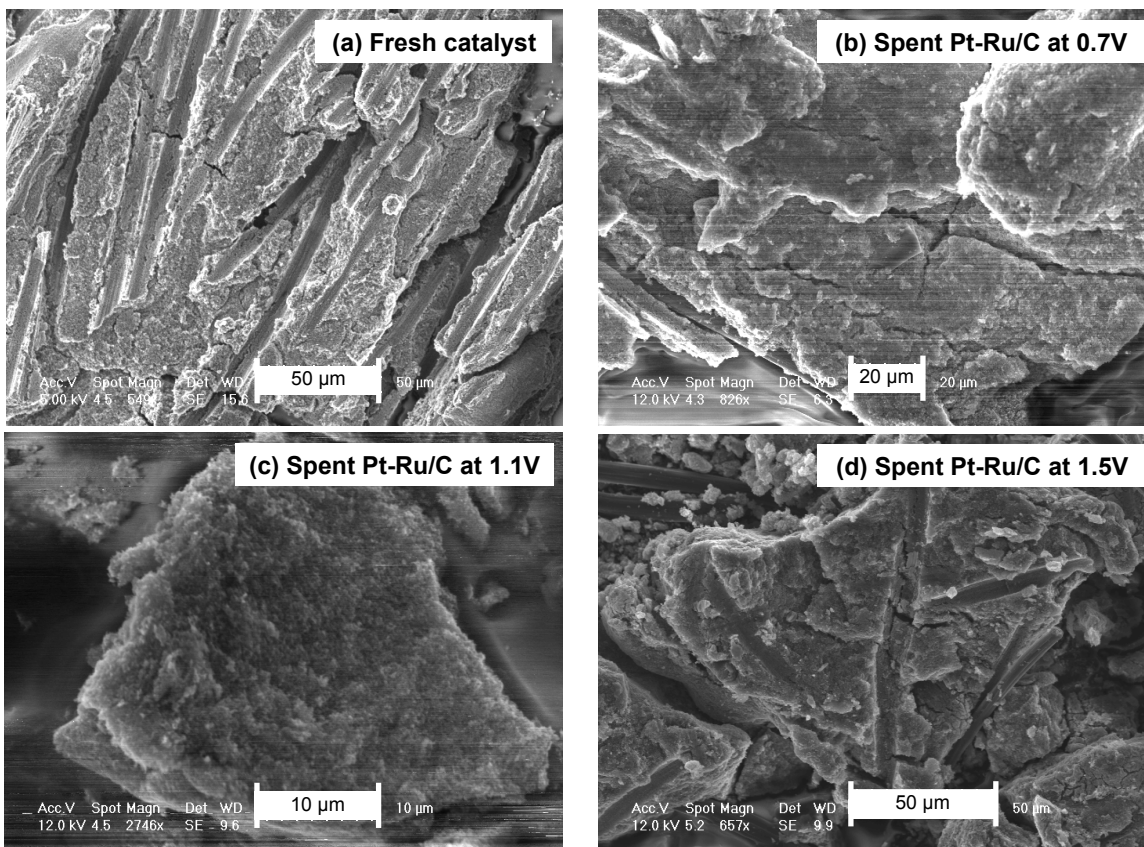
Figure 5.5: SEM images for fresh and spent catalysts scraped from MEAs (a) fresh Pt-Ru/C, (b) Pt-Ru/C spent at 0.7 V, (c) Pt-Ru/C spent at 1.1 V, (d) Pt-Ru/C spent at 1.5 V vs. RHE.

5.3.6 Thermogravimetric analysis on spent catalysts

Figure 5.6 shows the weight change measured by TGA during the temperature ramp for the Pt-Ru/C catalyst that was spent at 1.5 V vs. RHE for glycerol oxidation in a PEM reactor. Any moisture or organic species should be removed during the heating process in the furnace, and the remaining ash usually contains nonvolatile residues such as metal (e.g. Pt) or metal oxide (e.g. RuO_2).
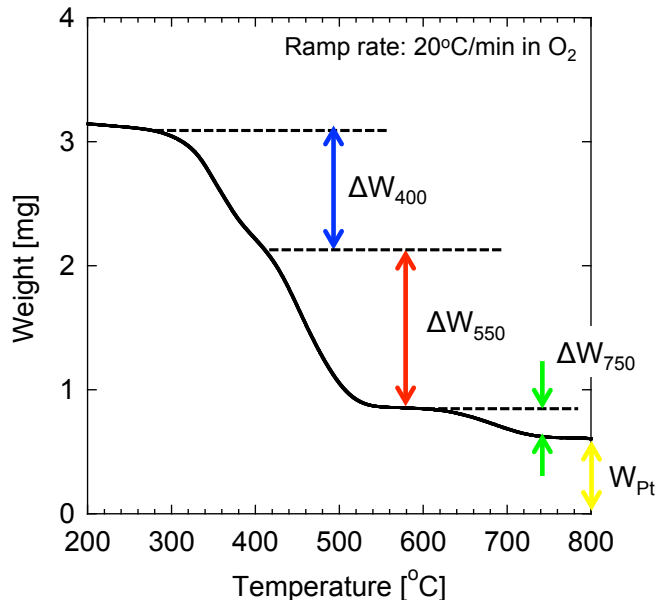
Figure 5.6: TGA results for Pt-Ru/C spent at 1.5 V vs. RHE scraped from MEAs.

There were three major losses of weight observed approximately at 400 °C, 550 °C, and 750 °C. The weight loss at a specific temperature corresponds to the decomposition of a specific carbon species. The presence of multiple weight-loss temperatures indicates that different types of carbon species were deposited [10]. For the temperatures below 200 °C, highly volatile materials such as moisture or solvent outgas, but they are of minimal importance for this study, and therefore excluded from the result. For temperatures of 200-750 °C, those degraded species are medium volatility materials, which typically include organics and polymers. Species degraded above 750 °C are referred to as combustible material, carbon black being an example [11].

The weight loss (ΔW) was used to compare the amount of extra material deposited on the surface with that of the fresh catalyst. Figure 5.7 shows the weight loss at each temperature (ΔW_T) divided by the final weight of Pt (W_{Pt}) for Pt-Ru/C spent at each constant potential. By dividing with W_{Pt}, the results were normalized by the weight of unit Pt to compare side by side when the starting weight was different. The weight of RuO_2 was excluded from W_{Pt}. The result for 0 V represents the data

for the fresh catalyst that was never exposed to the reaction. Any increase relative to the fresh catalyst indicates that additional species were deposited on the catalyst surface as a result of reaction.
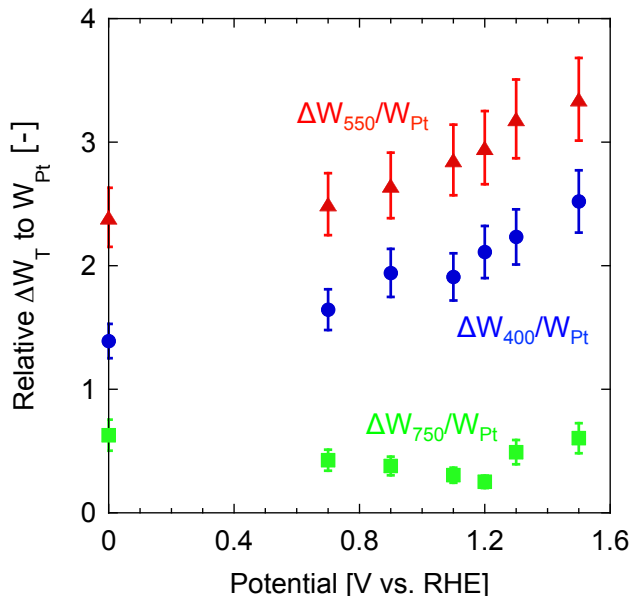
Figure 5.7: TGA results for fresh and spent Pt-Ru/C catalysts scraped from MEAs in terms of $\Delta W_T/W_{Pt}$.

For the species degraded at 400 °C and 550 °C, the excess of material ($\Delta W_{400}/W_{Pt}$ and $\Delta W_{550}/W_{Pt}$) increased linearly with potential. The value of $\Delta W_{750}/W_{Pt}$ had reduced compared to that for the fresh catalyst. This result indicated the loss of carbon black used as catalyst support.

According to the literature, CO desorption on Pt typically occurs at around 450-500 °C [12], which is close to the temperature where the ΔW_{550} is located in Figure 5.6. This leads us to the conclusion that ΔW_{400} is related to carbon deposition associated with the intermediate produced during the reaction. The sum of ΔW_{400} and ΔW_{550} is approximately equal to three molecules of carbon-based species covering the unit Pt molecule. These TGA results confirmed the presence of carbon deposition, CO poisoning, and carbon support corrosion, which could be the primary mechanisms of

catalyst deactivation occurring in the PEM reactor. Given that the weight loss at 550 °C possibly related to CO oxidation from the spent catalyst, the $\Delta W_{550}/W_{Pt}$ for Pt/C could be much higher than that for Pt-Ru/C, suggesting an interesting avenue for future study.

5.3.7   Carbon support corrosion

Carbon support corrosion has been fairly well studied in the context of PEM fuel cell catalyst durability [3–5, 13–19]. Carbon support corrosion is potential dependent, as indicated in the following equation.

$$C + 2H_2O \rightarrow 2CO_2 + 4H^+ + 4e^- \quad E^0 = 0.207 \text{ V vs. SHE} \tag{5.7}$$

This reaction particularly becomes important at more than 1.0 V vs. SHE (standard hydrogen electrode) under fuel starving conditions in acid electrolytes, and results in electrical isolation of the catalyst particles and aggregation of catalyst particles [19].

Figure 5.8 compares the concentration of CO_2 at the anode measured by the GC-TCD during water and glycerol oxidation in a PEM reactor. During water oxidation, carbon support was the only carbon source to produce CO_2 at the anode, while both glycerol and carbon support could provide carbon during glycerol oxidation. Approximately 15% of CO_2 was produced from the carbon support at 1.5 V vs. RHE, but its contribution had reduced to 0% when operated at 0.9 V vs. RHE. In other words, carbon support corrosion can be minimized by choosing a lower operating potential. The use of graphitized carbons could be another solution; graphitized carbon has been shown to be highly corrosion resistant in a high-temperature acid environment [20].
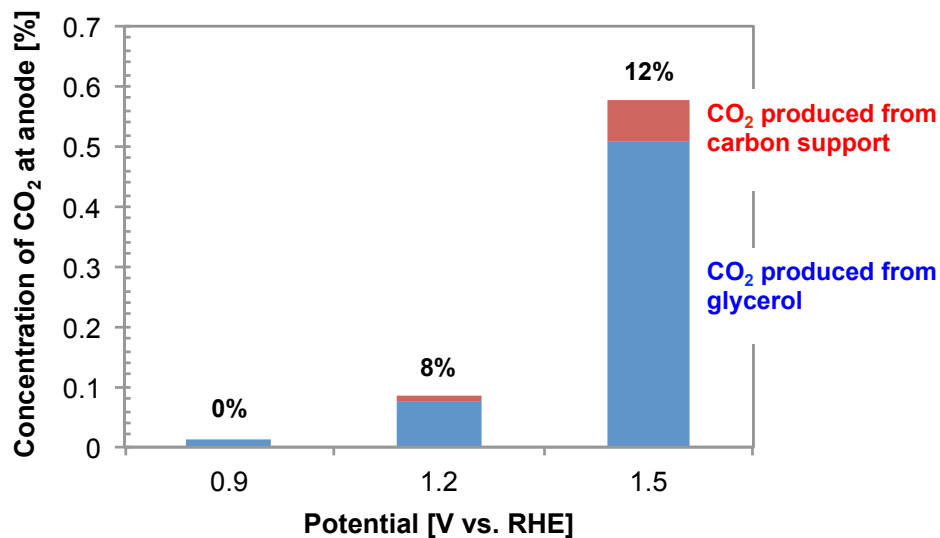
Figure 5.8: Concentration of CO_2 at anode for water oxidation and glycerol oxidation in a PEM reactor.

5.4 Conclusions

A series of experimental and theoretical studies suggested the existence of combined deactivation mechanisms occurring during glycerol oxidation in a PEM reactor. The main deactivation mechanisms could be carbon deposition, CO poisoning, and carbon support corrosion. Most of these effects can be minimized by lowering the operating potential, suggesting a trade-off between activity and durability.

References

[1] A. C. C. Tseung, S. C. Dhara, Loss of surface area by platinum and supported platinum black electrocatalyst, Electrochim Acta 20 (1975) 681–683.

[2] M. S. Wilson, F. H. Garzon, K. E. Sickafus, S. Gottesfeld, Surface area loss of supported platinum in polymer electrolyte fuel cells, J Electrochem Soc 140 (1993) 2872–2877.

[3] P. J. Ferreira, G. J. laO', Y. Shao-Horn, D. Morgan, R. Makharia, S. Kocha, H. A. Gasteiger, Instability of pt c electrocatalysts in proton exchange membrane fuel cells, J Electrochem Soc 152 (2005) A2256–A2271. Ti.

[4] M. Cai, M. S. Ruthkosky, B. Merzougui, S. Swathirajan, M. P. Balogh, S. H. Oh, Investigation of thermal and electrochemical degradation of fuel cell catalysts, J Power Sources 160 (2006) 977–986.

[5] F. Hasche, M. Oezaslan, P. Strasser, Activity, stability and degradation of multi walled carbon nanotube (mwcnt) supported pt fuel cell electrocatalysts, Phys. Chem. Chem. Phys. 12 (2010) 15251–15258.

[6] M. Pourbaix, Atlas of electrochemical equilibria in aqueous solutions, 2d english ed., National Association of Corrosion Engineers (1974).

[7] J. Newman, K. E. Thomas-Alyea, Electrochemical systems 3rd ed., Wiley-Interscience (2004).

[8] A. Voorhies, Carbon formation in catalytic cracking, Industrial & Engineering Chemistry 37 (1945) 318–322.

[9] A. C. Lausche, J. A. Schaidle, L. T. Thompson, Understanding the effects of sulfur on mo2c and pt/mo2c catalysts: Methanol steam reforming, Applied Catalysis A: General 401 (2011) 29–36.

[10] X. Chen, A. R. Tadd, J. W. Schwank, Carbon deposited on ni/ce-zr-o isooctane autothermal reforming catalysts, Journal of Catalysis 251 (2007) 374–387.

[11] D. E. Larkin, Compositional analysis by thermogravimetry: the development of a standard method, ASTM STP (1988) 28–37.

[12] G. Somorjai, Y. Li, Major successes of theory-and-experiment-combined studies in surface chemistry and heterogeneous catalysis, Topics in Catalysis 53 (2010) 311–325.

[13] L. Roen, C. Paik, T. Jarvi, Electrocatalytic corrosion of carbon support in pemfc cathodes, Electrochemical and Solid-State Letters 7 (2004) A19.

[14] C. Reiser, L. Bregoli, T. Patterson, J. Yi, J. Yang, M. Perry, T. Jarvi, A reverse-current decay mechanism for fuel cells, Electrochem Solid St 8 (2005) A273–A276.

[15] T. Patterson, R. Darling, Damage to the cathode catalyst of a pem fuel cell caused by localized fuel starvation, Electrochem Solid St 9 (2006) A183–A185.

[16] K. Matsutani, K. Hayakawa, T. Tada, Effect of particle size of platinum and platinum-cobalt catalysts on stability against load cycling, Platinum Metals Review 54 (2010) 223–232.

[17] F. T. Wagner, S. G. Yan, P. T. Yu, Catalyst and catalyst-support durability, Handbook of Fuel Cells – Fundamentals, Technology and Applications (2010) 1–14.

[18] M.-X. Wang, Q. Liu, H.-F. Sun, N. Ogbeifun, F. Xu, E. A. Stach, J. Xie, Investigation of carbon corrosion in polymer electrolyte fuel cells using steam etching, Mater Chem Phys 123 (2010) 761–766.

[19] K. G. Gallagher, R. M. Darling, T. F. Fuller, Carbon-support corrosion mechanisms and models, Handbook of Fuel Cells – Fundamentals, Technology and Applications (2010) 1–10.

[20] R. Borup, J. Meyers, B. Pivovar, Y. S. Kim, R. Mukundan, N. Garland, D. Myers, M. Wilson, F. Garzon, D. Wood, P. Zelenay, K. More, K. Stroh, T. Zawodzinski, J. Boncella, J. E. McGrath, M. Inaba, K. Miyatake, M. Hori, K. Ota, Z. Ogumi, S. Miyata, A. Nishikata, Z. Siroma, Y. Uchimoto, K. Yasuda, K.-I. Kimijima, N. Iwashita, Scientific aspects of polymer electrolyte fuel cell durability and degradation, Chem Rev 107 (2007) 3904–3951.

CHAPTER VI

Conclusion and future work

6.1   General conclusions

This thesis has focused on glycerol oxidation in the context of a PEM reactor. Various physical and electrochemical characterization methods were applied to understand the reaction.

Some noble metals (Pt, Ir, and Rh) were first tested in a solid-state cell to screen the active catalyst for glycerol oxidation at a Nafion® interface. Pt showed the best performance in terms of the ability to adsorb glycerol and activity towards glycerol oxidation. Therefore, Pt-based catalysts (Pt black, Pt/C, and Pt-Ru/C) were chosen for further evaluation in a PEM reactor.

The effects of electrocatalyst and applied potential on activity and selectivity were studied by evaluating the order of reactions and intermediates. Glycerol oxidation rates in the reactor occurred with first-order kinetics, an observation consistent with the literature [1]. While the rates for Pt/C and Pt-Ru/C were similar, a significant change in selectivity towards partial oxidation products (e.g. glyceraldehyde) was observed when adding Ru to Pt. Ru by itself exhibited negligible rates of glycerol oxidation, indicating a change in surface chemistry between Pt, Pt-Ru, and Ru.

The glycerol oxidation pathways and the rate-determining step were also identified for each catalyst. Tafel slope analysis suggested that the rate determining steps for

Pt and Pt-Ru may be similar. The selectivity shift between Pt/C and Pt-Ru/C was possibly caused by some surface chemistry change correlated with the electronic structure. The electronic structure greatly influences the adsorption energy of specific molecules to the catalyst surface that favors certain reaction pathways. One example was discussed in Chapter 4 regarding the improvement of CO tolerance from pure Pt to Pt-Ru alloy by reducing the CO adsorption energy measured by XPS [2].

We also observed a reduction of the glycerol adsorption barrier on the Pt-Ru surface relative to Pt. For Pt/C, glycerol starts to adsorb at a rather high potential where the Pt surface forms Pt-O. This active oxygen interacts with glycerol molecules and breaks C−C bonds (dissociative oxidation) in addition to facilitating partial oxidation. On the other hand, for the Pt-Ru surface, glycerol starts to adsorb at a much lower potential, where the Pt surface is not yet oxidized, resulting in more partial oxidation than dissociative oxidation. Ru can also activate water at much lower potentials to create the surface hydroxyl that is necessary to oxidize surface-bonded species, which facilitates the desorption of partially oxidized species.

Catalyst deactivation mechanisms occurring in a PEM reactor during glycerol oxidation were also investigated. Based on nonlinear regression analysis and experimental observations, we conclude that several deactivation mechanisms exist simultaneously. Particle sintering may be occurring, but the crystal size of the Pt is too small to be detected by the XRD, and thus the effect of sintering is still unknown. The ECSA loss over time suggests that Pt dissolution is unlikely due to the mismatch in time scales between empirical values and predictions based on diffusion theory. TGA suggested that carbon deposition, CO poisoning, and carbon support corrosion were the major contributors for deactivation, which can be minimized by selecting a lower operating potential.

In summary, Pt-alloy could be developed as a selective catalyst for glycerol oxidation in a PEM reactor to produce commodity chemicals. However, simultaneous

management of catalyst deactivation is required to ensure the long-term and stable operation of the reactor.

6.2 Future directions of this research

Throughout this research, one of the most interesting findings was the effect of electrocatalyst on product selectivity. In the case of glycerol oxidation, the selectivity towards the partial oxidation product was greatly improved by alloying Pt with Ru. Therefore, it is worthwhile to screen other Pt alloy catalysts for performance. The type of solid-polymer electrolyte also has an impact on both activity and selectivity, which should be investigated further. This reaction can also be evaluated in a non-aqueous environment that would eliminate the competing reaction associated with water oxidation to achieve higher efficiency.

While this thesis focused on understanding the difference in selectivity between Pt and Pt-Ru, the parameters that would increase the reaction rate should also be explored. For example, the gravimetric rate could be improved by highly dispersing Pt on carbon black. Next-generation support such as carbon nanotubes may have a positive effect on both rate and selectivity.

To deepen our understanding of the selectivity shift occurring on Pt and Pt-Ru surfaces, additional experiments can be performed, including XPS to measure adsorption energy on probe molecules, in-situ Raman spectroscopy in a three-electrode cell to characterize reaction intermediates, or electrochemical impedance spectroscopy to obtain differential capacity with respect to each reaction intermediate related to adsorption strength, which would help to develop a more comprehensive glycerol oxidation mechanism.

Finally, improved resistance to catalyst deactivation is an important area for future research, especially in the context of carbon deposition, CO poisoning, and carbon support corrosion when used in a PEM reactor environment. Findings in this direction

will also be a great base on which to develop more reliable fuel cell technology.

References

[1] L. Roquet, E. Belgsir, J. Leger, C. Lamy, Kinetics and mechanisms of the electrocatalytic oxidation of glycerol as investigated by chromatographic analysis of the reaction-products - potential and ph effects, Electrochim Acta 39 (1994) 2387–2394.

[2] M. Wakisaka, S. Mitsui, Y. Hirose, K. Kawashima, H. Uchida, M. Watanabe, Electronic structures of pt-co and pt-ru alloys for co-tolerant anode catalysts in polymer electrolyte fuel cells studied by ec-xps, J Phys Chem B 110 (2006) 23489–23496.